January 2016

Interfacial Mechanical Strength Characterization in Multilayered Materials via Nanoscale Impact and Nano Mechanical Raman Spectroscopy Experiments

Devendra Verma
Purdue University

Recommended Citation

Verma, Devendra, "Interfacial Mechanical Strength Characterization in Multilayered Materials via Nanoscale Impact and Nano Mechanical Raman Spectroscopy Experiments" (2016). *Open Access Dissertations*. 1232.
https://docs.lib.purdue.edu/open_access_dissertations/1232

INTERFACIAL MECHANICAL STRENGTH CHARACTERIZATION IN MULTILAYERED MATERIALS VIA NANOSCALE IMPACT AND NANO MECHANICAL RAMAN SPECTROSCOPY EXPERIMENTS

by

Devendra Verma

A Dissertation

Submitted to the Faculty of Purdue University

In Partial Fulfillment of the Requirements for the degree of

Doctor of Philosophy

Department of Aeronautics and Astronautics
West Lafayette, Indiana
December 2016

THE PURDUE UNIVERSITY GRADUATE SCHOOL
STATEMENT OF DISSERTATION APPROVAL

Dr. Vikas Tomar, Chair
    School of Aeronautics and Astronautics
Dr. R. Byron Pipes
    School of Aeronautics and Astronautics
    School of Materials Engineering
    School of Chemical Engineering
Dr. Amit H. Varma
    Lyles School of Civil Engineering
Dr. Weinong Chen
    School of Aeronautics and Astronautics
    School of Materials Engineering

Approved by:
Dr. Weinong Chen
Head of the Departmental Graduate Program

Dedicated to
my parents
Shakuntala and Ramesh,
and my siblings
Manju, Pushpa, and Ankit
for my childhood memories.

ACKNOWLEDGMENTS

I would like to start by thanking my advisor Dr. Vikas Tomar for supporting me during my stay at Purdue. He was instrumental to my growth as a researcher and as a person that I have grown into during last five years. He gave me opportunities to work on diverse set of problems apart from my thesis. I would also like to thank my committee members Dr. Pipes, Dr. Chen and Dr. Varma for their support and guidance throughout the process.

I cannot possibly mention numerous other friends I made at Purdue who kept me motivated to keep going on my journey but I am deeply thankful to have met all of them. I got the opportunity to meet all these wonderful people during my time in Purdue Graduate Student Government, Boiler Out and various AAE activities.

In the end, I would also like to mention my lab-mates who are like a family to me here.

TABLE OF CONTENTS

LIST OF TABLES

LIST OF FIGURES

ABSTRACT

Author: Verma, Devendra. Ph.D.
Institution: Purdue University
Degree Received: December 2016
Title: Interfacial Mechanical Strength Characterization in Multilayered Materials via Nanoscale Impact and Nano Mechanical Raman Spectroscopy Experiments
Major Professor: Vikas Tomar.

A composite materials strength can significantly depend on the constitutive description of interfaces. A computational model of composite deformation should, therefore, incorporate interface constitutive behavior. These interfaces poses several challenges in studying them due their length scales of micrometer to nanometer as well the coupling of other factors such as confinement during the loading. Thus, separating main phase constitutive behavior from interface constitutive behavior in mechanical property measurement experiments is an arduous task. In this work, an epoxy interface between glass plates is analyzed under quasistatic and dynamic loading conditions to obtain a description of interfacial constitutive response at strain rates from 10^{-2} to 10^{3} s^{-1}. The experiments were conducted with indenters of radius 1, 10 and 100 μm on the interfaces thicknesses of 1, 10 and 100 μms within the spatial error tolerance of less than 3 μms. The interface thickness was verified with the Scanning Electron Microscopy (SEM) and Energy Dispersive X-ray (EDX) analysis. The approach relies on describing interfaces as a confined material phase between two unconfined phases. Dynamic microscale impact tests are used to obtain stress-strain response as a function of strain rate for the analyzed interfaces. The data was then subjected to statistical analysis to remove experimental errors. An analytical model was developed to find the confinement effect and the solution was verified by capturing stress maps with Nanomechanical Raman Spectroscopy (NRS) experiments pre and post experiments to analyze the change in the stress distribution around interfaces. Based on the analyses of confinement effects, a constitutive model is proposed to predict the interface deformation behavior with a dependence on both strain rate and confinement effect. This model is further used in the finite element simulations to predict and quantify the role of interfaces in multilayered materials.

CHAPTER 1. INTRODUCTION

1.1 Objectives and Significance

The development of advance materials have led researchers to look for inspirations from various material systems such as naturally occurring shells in shrimps, crabs etc [1, 2]. These materials are providing important insights into the hierarchical design needed to improve the properties such as strength and toughness of the materials. One of the key factors contributing to the exceptional properties of these materials is their multilayered structure. The presence of multilayers provides them higher tensile strength in metals, better brittle properties in ceramics etc. These multilayers also lead to higher strength to weight ratio, less friction and wear, higher temperature operation, higher corrosion resistance, higher fracture toughness etc. They key to translate these properties in developing better materials lies in understanding the interface behavior between the layers of multilayered materials.

The development of new composites as well as metallic multilayered alloys needs a better understanding of the behavior of these interfaces as a function of rate of deformation and their composition. The understanding of constitutive behavior of these interfaces will also lead to development of finite element models to be able to predict the deformations under different loading scenarios. Thus, a combination of the understanding of the constitutive behavior of the interface and their role in the bulk properties of the multilayered materials is an essential piece needed for the development of better multilayered materials. The current work investigates the role of these interfaces.

1.2 Research Challenge

The multilayered materials are made up of thousands of individual layers which makes it difficult to identify and extract its constitutive behavior. The length scale of these interfaces poses another challenge that needs special experimental tools to perform the experiments which are otherwise not possible in regular uniaxial tests. These interface range from few nanometers in metals to few micrometers in ceramics and other composite materials. These interfaces also vary in their thickness across same material system with a gradient effect. Therefore, a new method needs to be developed to study the behavior of these individual interfaces.

It is in addition to identifying the zone around the interfaces where they play a role during the application of different loads as well the effect of its structure. Thus, the experiments needs to be designed such that these deformations in the interfaces could be visually monitored too. It is also not clear how different factors such as strain rates of loading, presence of other interfaces in nearby region, temperature changes during the experiment and the effect of interface composition are coupled with each other. A thorough investigation is needed to decouple these effects and to develop constitutive laws defining their roles.

The main research challenge to decouple the behavior of the interfaces from the main phases of the material is addressed in the case of epoxy interfaces between glass plates. The confinement effect on these interfaces is also addressed and accounted for in the constitutive law along with the effect of coupling. It is then further implemented in finite element software to quantify the role of individual interfaces.

1.3 Chapter Outline

Chapter 2 gives an overview of the role of interfaces in different materials studied by the authors as well as other researchers. The differences between biomaterials and metallic materials are highlighted. An account of different tools such as molecular dynamic simulations, theoretical frameworks is given with the advantages and disadvantages of each method. In the end, a description of the current technique is provided.

Chapter 3 describes the experimental tools used to study the interfaces in this research. The first part discusses the nanoindentation principles and the advantages of this technique. The second part describes the use of nanoscale impacts to study the high strain rate behavior of these materials. The third part gives a detailed account of the nanomechanical Raman spectroscopy technique and its unique advantage in measuring the stresses in a non-contact way.

Chapter 4 includes the nanoindentation and nanoscale impact experiments performed on the samples. It starts with the sample preparation methods used to make the samples. It is followed by the description of data collection methods as well as their statistical analysis. The rate dependence on the data is discussed which is further used to find the stress-strain relations of the interfaces.

Chapter 5 further discusses the stress-strain relations of interfaces and the observed differences in the material in the interface and its native state. The difference is found to stem from the confinement effect which is further investigated and an analytical model is developed to account for it. The analytical model is validated using nanomechanical Raman spectroscopy measurements.

Chapter 6 includes the step by step explanation of the development of the new constitutive law which couples the confinement effect and the strain rate effect in the deformation of interfaces. It is further developed for difference sizes of interfaces in the materials.

Chapter 7 utilizes the new confinement model and shows its application in quantifying the role of interfaces in different material systems using finite element software ABAQUS. The simulations are compared with the experimental results to validate the model. The contribution of each individual interface is shown from the energy absorbed by each interface.

Chapter 8 summarizes the thesis with the conclusions and provides recommendations for the future work. The possible applications of the proposed model are described along with mentioning its limitations.

1.4 Contributions

There are three main contributions of this thesis, which gives a new direction in understanding the multilayered material behavior:

1. An interface constitutive law is developed that couples the strain rate dependence and the confinement effect in the deformation of interfaces. The law is developed based on the experimental investigation of epoxy interfaces between glass plates. The law is further implemented in finite element software to quantify and predict the role of interfaces in the deformation of multilayered materials.

2. An analytical solution is developed to calculate the multiaxial stresses in the interfaces in materials. The analytical solution also provides the stress distribution across the depth of the interfaces. The analytical solution is further verified using

nanomechanical Raman spectroscopy experiments which is developed in our lab to measure the stress distributions in a non-contact way.

3. The scope of the nanoindentation method is further stretched to be able to predict the strain rate dependence on materials from nanometer to micrometer length scale which is otherwise not possible using the conventional uniaxial tests.

CHAPTER 2. INTERFACES IN MATERIALS

2.1 Interfaces in Biomaterials

Naturally occurring materials have been of keen interest in the materials community with the aim of understanding and reproducing the exceptional strength and toughening mechanisms present in these materials, e.g. exoskeletons of shrimps [2, 3], lobsters [4, 5], crabs [6, 7], nacre [8, 9] etc. All such materials share some common traits such as a strong hierarchical structure, layered structure, composition of material with both minerals and fibers, gradient in the thickness of layers, etc. These naturally occurring materials have been able to manipulate the characteristics mentioned above to customize the design of their exoskeletons for survival in different habitats, cuticles to attack the predators to mention a few applications. The one important parameter along with the material composition in such designs is the role of the interfaces in the multilayered structure. In our earlier articles, we highlighted the difference between the mechanical properties of two similar species of shrimp Pandalus Platyceros and Rimicaris Exoculata, that are found at sea level and at 2300 m depth in the sea as a function of habitat with focus on wet vs dry conditions [3], temperature effect [2], and mineral composition [10, 11].

The individual layers in the Bouligand exoskeleton consist of chitin based fibrils coated in proteins at nanometer level. Such fibrils bind together to form fibers. These fibers are then woven together to form chitin-protein layers. These layers are stacked in a twisted plywood structure known as the Bouligand pattern. The spacing between such woven layers is filled with proteins and biominerals [1-3, 10, 11]. Raabe et al. [5, 12] studied the structure and mechanical properties of lobster exoskeleton reporting the hardness and the reduced stiffness with depth of exoskeleton of lobster. Boßelmann et al. [4] showed the direct correlation between increase in mineral content and hardness of lobster claw. Chen et al. [7] compared the mechanical properties of the crab shell in dry and wet conditions revealing the effect of wet conditions. Sylvain et al.[13] showed the effect of the packing of the calcite layers in the protein at nm scale on the high strength and toughness of nacre. Feng et al. [9] found that the crack deflection, fiber pull-out and organic matrix bridging are the three main toughening mechanisms acting on nacre along with the organic matrix which also plays a major role in the toughening. Chen et al. [14] investigated the structure of natural ceramic mollusk shell for fracture strength and fracture toughness while identifying different shapes and arrangements of laminated aragonites and organic layers. Schneider et al. [15] developed models that are capable of predicting strength values for real biomaterials up to five hierarchical levels. This discussion is a small summary of work done in the natural materials area with focus on Bouligand structure.

A more involved list of the experimental work done at the interfaces in various materials is presented in Table 2-1. The table lists the material type, key aspects of measurements, and authors by year. This list, even though, does not list each and every possible article in the literature (and only lists work going back 15 years), gives the reader a comprehensive review of the experimental techniques and measurements focusing on interfaces.

Table 2-1 List of experimental research at the interfaces in materials.

Year	Materials	Key aspects	Authors
2015	Shrimp exoskeleton	Layered structure with thickness gradient. Interface helps in crack containment	Verma et al. [1, 10, 11]
2015	Polypropylene/glass fiber composite	Interlaminar interface strength contribution in impact resistance	Sorrentino et al.[16]
2015	TiAl64/Steel	Interface properties fluctuation in dynamic conditions	Verma and Tomar [17]
2014	PP/glass fiber	Interface strength in low velocity impact	Simeoli et al. [18]
2014	Nacre	Organic interlamellar layers contribution to strength	Lopez et al. [19]
2014	Calcia and Silica	Ceramic bioinspired composite from nacre	Bouville et al. [13]
2013	Ti-43Al-9V/Ti-6Al-4V	Thermal behavior of interface joints	Wang et al. [20]
2013	Suture Tendon	Stitching at suture-tendon interface	Savage et al. [21]
2013	Biomaterials	Mechanical characterization	Roeder [22]
2013	Ti/Ni, Ti64/Steel	Interfacial strength properties	Kundu et al. [23, 24]

Table 2-1 Continued

2013	Ti64/Bone	Implant/bone interface	Grandfield et al. [25]
2013	Alloy 718	Welded interface properties	Damodaran et al. [26]
2013	Glass/epoxy	Impact fatigue	Azouaoui et al. [27, 28]
2012	Polymide and nano clay	Bioinspired honeycomb structure	Xu et al. [29]
2012	Odontodactylus scyllarus	Multiphase bio composite	Weaver et a. [30]
2012	Fiber-metal laminate	Impact resistance	Sadighi et al. [31]
2012	Ti/Ni/Steel	Diffusion bonded layers	Sam et al. [32]
2012	Ti/Ni/Steel	Diffusion bonded joint	Peng et al. [33]
2012	Cu/Nb multilayers	Effect of He ion implants	Li et al. [34]
2012	Ti/Steel	Interface microstructure	Kundu et al. [35]
2012	Glass/epoxy	Interface strength by pull-out tests	Koyanagi et al. [36, 37]
2012	Beetle forewings	Bioinspired honeycomb structure	Chen et al. [38]
2012	Copper	Role of grain boundary in fracture of material	Cerreta et al. [39]
2011	Biomaterials	Design principles	Wu et al. [40]
2011	Barnacle exoskeleton	Nanomechanical properties of the cuticle	Raman et al. [41]

Table 2-1 Continued

2011	CNF/Polymer composite	Tensile stress measurements	Mohan et al. [42]
2011	GFRP laminates	Impact strength of the laminates under impact	Menna et al. [43]
2011	Bone	Structure and hierarchical organization	McNamara [44]
2011	Natural materials	Energy dissipation by organic layers	Mayer [6]
2011	Soft tissues	Contact stresses dissipation	Korhonen et al. [45]
2011	Pt-Ir coatings	Adhesive interlayer strength	Klocke et al. [46]
2011	TiN coatings	Effect of interface on cyclic damage	Chen et al. [47]
2011	Magnesium alloy	Bone –implant interface	Castellani et al. [48]
2010	Ti64 coating	Wear properties of coatings	Wheeler et al. [49]
2010	Lobster cuticle	Hierarchical organization of layered structure	Svetoslav et al. [50]
2010	Concrete/epoxy	Fracture characterization	Lau et al. [51]
2010	Carbon/epoxy	Time and temperature dependence of interface strength	Koyanagi et al. [52]

Table 2-1 Continued

2010	Nacre	Interconnectedness of chitin interfaces	Bezares et al. [53]
2010	Biological material	Hierarchical structure	Bechtle et al. [15]
2009	Fish	Anisotropic design	Lifeng et al. [54]
2009	Nacre	Biomimetic design	Luz et al. [55]
2009	AlTiN and TiAlCrN	Coating strength	Fox-Rabinovich et al. [56]
2009	Graphene	Nanoindentation property measurements	Das et al. [57]
2009	Mollusk shells	Cross laminar interface links	Barthelat et al. [58]
2008	Dentin	Residual tensile stress effect	Hernandez et al. [59]
2008	Particulate-polymer nanocomposite	Particle/matrix interface adhesion	Fu et al. [60]
2008	Ag/Ni	Interface stress measurements	Birringer et al. [61]
2008	Crab exoskeleton	Structure and mechanical properties	Chen et al. [7]
2007	Ag/Ni	Bilayer thickness effect on the properties	Kang et al. [62]
2006	Glass/ carbon fiber	Temperature effect at interfaces	Ray [63]

Table 2-1 Continued

2006	Lobster exoskeleton	Chitin protein microstructure	Raabe et al. [5, 12]
2006	Biological materials	Design principles	Mayer [64]
2005	Natural Fiber-Polyolefin	Interfacial strength between fiber and matrix	Sain et al. [65]
2004	Bivalva shell	Ceramic polymer interface fracture strength	Chen et al. [14]
2001	Cement/cement	Interface strength based on time of cure	Park et al. [66]
2000	Nacre	Alumina/Kevlar composite cased on nacre	Feng et al. [9]
1999	Glass/epoxy	Glass epoxy cross linked interface	Swadener et al. [67]
1999	Ag/Ni	XRD interface stress measurements	Josell et al. [68]
1998	biomaterials	Interfaces in biomaterials	Bonfield et al [69]
1996	Stone crab	Hardness measurements across the thickness	Melnick et al [70]
1995	Ag/Cu	Interface stress measurements	Berger et al. [71]
1994	Glass/epoxy	Interface degradation	Chateauminois et al. [72]

Table 2-1 Continued

1993	Metal/ceramic	Interface strength measurement by laser	Gupta et al. [73, 74]

2.2 Interfaces from Molecular Dynamic Simulations Perspective

The interfaces in several materials are also studied using molecular dynamic tools to be able to predict the mechanisms of deformation in interfaces at molecular level. One unique feature that determines the properties of natural biomaterials is the interfacial interactions between organic and inorganic phases in the form of protein (e.g. chitin (CHI) or tropocollagen (TC))-mineral (e.g. calcite (CAL) or hydroxyapatite (HAP)) interfaces, [75-78]. The size of protein-mineral interfaces can be enormous. Such interfaces control biological reactions, and provide unique organic microenvironments that can enhance specific affinities, as well as self-assembly in the interface plane that can be used to orient and space molecules with precision. Interfaces also play a significant role in determining structural integrity and mechanical creep and strength properties of biomaterials. In the structural studies of such biological materials, it is observed that at the mesoscale (~100 nm to few µm), the mineral crystals are preferentially aligned along the length of the organic phase polypeptide molecules in a hierarchical (e.g. staggered or Bouligand pattern) arrangement [79-83]. The length scale and complexity of microstructure of hybrid interfaces in biological materials make it difficult to study them and to understand the underlying mechanical principles, which are responsible for their extraordinary mechanical performance. One of the most important aspects of understanding the influence of interfaces on natural material properties, is the knowledge of how stress transfer occurs across the organic-inorganic interfaces. Molecular modeling provides a way to study such phenomenon at the length scale of the individual molecular components and a brief review of some of these studies is given below.

The effect of different kinds of interfaces was modeled in our research in the case of chitin-calcite interactions, Qu et al [84, 85]. These studies focused on the role of interface related mechanisms in determining overall mechanical deformation properties while also addressing the real aspect of stresses at interfaces. A brief literature survey list of the simulation work done at the interfaces in materials is presented in Table 2-2. The table lists the material type, key aspects of measurements, and authors by year. Even though the list does not contain each and every possible article in the literature, it gives the reader a general overview of the modeling techniques and measurements available in the literature on biomaterials, metals, composites and ceramics.

Table 2-2 List of modeling research at the interfaces in materials.

Year	Materials	Key aspects	Authors
2015	Chitin-calcite	Effect of interface composition	Qu et al. [84, 85]
2014	Collagen	Interface thermomechanics	Qu et al. [86]
2014	Stainless Steel	Dislocations at grain boundaries	McMurtrey et al.[87]
2014	Nacre like aluminium composite	Impact behavior of wavy interfaces	Flores-Johnson et a. [8]

Table 2-2 Continued

2013	Collagen	Viscoelastic properties	Gautieri et al. [88]
2012	Laminate composite	Low velocity impact strength	Shi et al. [89]
2012	Graphene	Fracture at interface of the graphene joints	Fang et al. [90]
2011	Fcc/bcc interface	Dislocation mechanisms	Zhang et al. [91]
2011	Cu/Nb interface	Interface dominated deformation mechanisms	Wang et al. [92]
2011	Fcc/bcc/ multilayers	Interface shear strength	Wang et al. [93]
2011	GFRP laminates	Impact strength	Menna et al. [43]
2011	Pt-Ir coatings	Adhesive interlayer strength	Klocke et al. [46]
2010	Steel/steel	Stress distribution on joint line of the material	You et al. [94]
2010	composites	Failure of interface	Wisnom [95]
2010	Nacre	Interconnectedness of chitin interfaces	Bezares et al. [53]
2009	fish	Anisotropic design of the fish exoskeleton	Lifeng et al. [54]
2009	Cu/Nb	Crystal elastic/plastic model for nanoscale metallic multilayers	Wang et al. [96]

Table 2-2 Continued

2008	Ag/Ni	Interface stress measurements	Birringer et al. [61]
2002	Bentonite clay	Diffusivity of chemical species	Ichikawa et al. [97]
2001	Carbon-epoxy	Stress transfer	Paipetis et al. [98]
1999	Agglomerates	Impact strength based on surface energy	Subero et al. [99]

2.3 Interface from Theoretical Formulations

The concepts of dividing surface, interfacial excess energy and interfacial stress were initially introduced by Gibbs [100]. According to the Gibbs formulation, the amount of reversible work dw performed to create new area dA of a fluid or solid surface can be expressed as

$$dw = \gamma dA. \tag{2.1}$$

Here, γ is the surface tension. Interface excess energy is directly correlated to interface mismatch stress with both having origin in orientation mismatch at the interfaces. The surface contributions to the thermodynamic quantities are defined as the excesses over the values that would be obtained if the bulk phases retained their properties constant up to a two-dimensional imaginary dividing surface embedded in a three- dimensional continuum. In other words, the interface (not interphase) is a mathematical surface of zero thickness over which the thermodynamic properties change discontinuously from one bulk phase to the other. The excess amount is associated only with the dividing surface. These formulations were developed for continuum mechanics by Shuttleworth [101] relating the interfacial excess energy to surface stress [101]. The formulations were further developed by Gurtin and coworkers to find relations between the surface and body stresses[102].

$$\begin{aligned} &div\Sigma = Tn + \rho_0 \ddot{u}, \\ &\Sigma = \sigma I + 2\left(\mu_0 - \sigma\right) IE + \left(\lambda_0 + \sigma\right)\left(trE\right) I + \sigma\Delta u, \\ &E = 1/2\left(Du + Du^T\right). \end{aligned} \tag{2.2}$$

Here, T , u and E denote, respectively, the stress, displacement and the strain field. The constants ρ, λ and μ are the mass density and Lame moduli for body while with $\rho_o, \sigma, \lambda_o$ and for the surface. $\sum$ denotes the surface stress. Such relations have been widely used and modified in the recent years by Sharma et al.[103], Yang et al.[104], Cammarata et al.[105] etc. Dingreville and Qu[106, 107] related surface stress at interface with interface in-plane strain and in-plane stress based on a modification of Shuttleworth and Herring[43] model, applicable to coherent interfaces and recently extended to include some degree of incoherency. The interfacial excess energy equation for the case of a flat interface between two elastic solids as shown in Fig. 2-1 were given by Dingreville and Qu[106-108]. The stress and strain far away from the interface are defined as

$$\lim_{x_3 \to \pm\infty} \boldsymbol{\sigma} = \boldsymbol{\sigma}_{\pm}, \quad \lim_{x_3 \to \pm\infty} \boldsymbol{\varepsilon} = \boldsymbol{\varepsilon}_{\pm}. \tag{2.3}$$

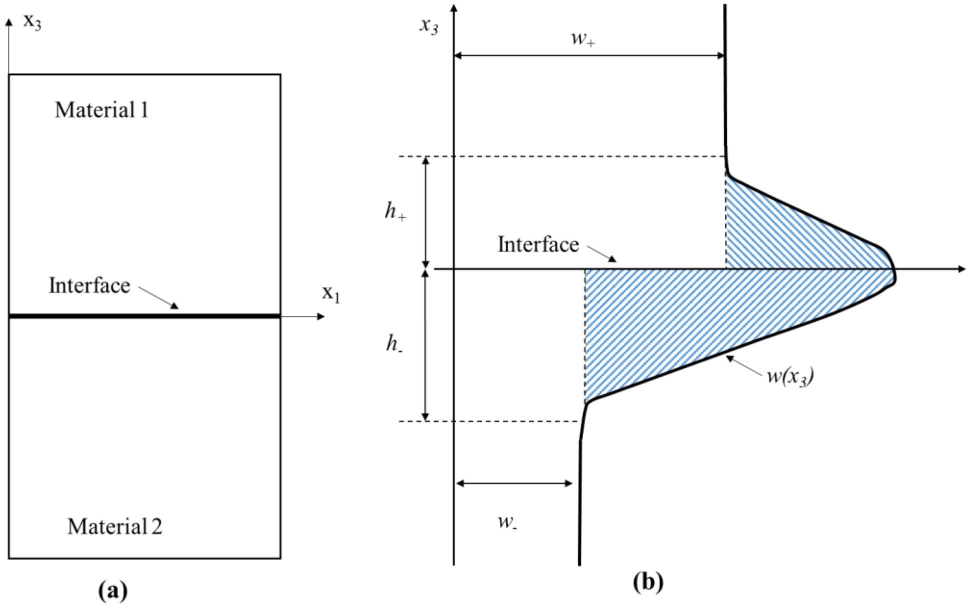

Fig. 2-1. (a) Schematic of flat interface (b) Distribution of strain energy near interface. Figure adapted from Dingreville and Qu [107]

Here, regions with $x_3 > 0$ are denoted by positive sign and regions with $x_3 < 0$ are denoted by negative sign. In the given scenario, the standard Gibbs definition of the interfacial excess energy per unit undeformed area is given by

$$\Gamma = \int_{0}^{\infty} \left[w(\mathrm{x}_3) - w_+ \right] dx_3 + \int_{-\infty}^{0} \left[w(\mathrm{x}_3) - w_- \right] dx_3 \,, \tag{2.4}$$

where,

$$w\left(x_3\right) = \hat{c}_0 + \hat{\boldsymbol{\tau}}^s : \boldsymbol{\varepsilon}^s + \frac{1}{2} \boldsymbol{\varepsilon}^s : \mathbf{C}^s : \boldsymbol{\varepsilon}^s + \frac{1}{2} \boldsymbol{\sigma}^t : \mathbf{M} : \boldsymbol{\sigma}^t \,, \tag{2.5}$$

$$w_\pm = \frac{1}{2} \boldsymbol{\varepsilon}^s_\pm : \mathbf{C}^s_\pm : \boldsymbol{\varepsilon}^s_\pm + \frac{1}{2} \boldsymbol{\sigma}^t_\pm : \mathbf{M}_\pm : \boldsymbol{\sigma}^t \,, \tag{2.6}$$

are the elastic strain energy densities(in the undeformed configuration) corresponding to the total and remote fields, respectively. Specifically, $\boldsymbol{\varepsilon}^s$ and $\boldsymbol{\sigma}^t$ are, respectively, the in-plane and transverse stress tensors. The integrals needs to be carried out only over the thickness of the interfacial region, $h_+ + h_-$ as given in Fig. 2-1(b). In the flat part, the transverse part of the stress tensor is uniform throughout the biomaterial, $\sigma^t = \sigma^t_+ = \sigma^t_-$. Furthermore, continuity of displacement along the interface leads to $\varepsilon^t = \varepsilon^t_+ = \varepsilon^t_-$. Solving it further the interfacial excess energy can be written as

$$\Gamma = \Gamma_0 + \mathbf{\Gamma}^{(1)} : \boldsymbol{\varepsilon}^s + \frac{1}{2}\boldsymbol{\varepsilon}^s : \mathbf{\Gamma}^{(2)} : \boldsymbol{\varepsilon}^s + \frac{1}{2}\boldsymbol{\sigma}^t : \Lambda^{(2)} : \boldsymbol{\sigma}^t , \tag{2.7}$$

where,

$$\Gamma_0 = \int_{-\infty}^{\infty} \hat{w}_0(x_3)dx_3, \quad \mathbf{\Gamma}^{(1)} = \int_{-\infty}^{\infty} \hat{\boldsymbol{\tau}}^s(x_3)dx_3, \tag{2.8}$$

$$\mathbf{\Gamma}^{(2)} = \int_0^{\infty}\left[\mathbf{C}^s(\mathrm{x}_3) - \mathbf{C}^s_+\right]dx_3 + \int_{-\infty}^{0}\left[\mathbf{C}^s(\mathrm{x}_3) - \mathbf{C}^s_-\right]dx_3 , \tag{2.9}$$

$$\mathbf{\Lambda}^{(2)} = \int_0^{\infty}\left[\mathbf{M}(\mathrm{x}_3) - \mathbf{M}_+\right]dx_3 + \int_{-\infty}^{0}\left[\mathbf{M}(\mathrm{x}_3) - \mathbf{M}_-\right]dx_3 . \tag{2.10}$$

Equation (2.7) gives the interfacial excess energy as an explicit function of the in-plane strain and transverse stress tensors. The interfacial excess stress is given by

$$\mathbf{\Sigma}^s = \int_0^{\infty}\left[\boldsymbol{\sigma}^s(\mathrm{x}_3) - \boldsymbol{\sigma}^s_+\right]dx_3 + \int_{-\infty}^{0}\left[\boldsymbol{\sigma}^s(\mathrm{x}_3) - \boldsymbol{\sigma}^s_-\right]dx_3 . \tag{2.11}$$

Which is further modified as

$$\mathbf{\Sigma}^s = \mathbf{\Gamma}^{(1)} + \mathbf{\Gamma}^{(2)} : \boldsymbol{\varepsilon}^s + \boldsymbol{\sigma}^t \cdot \mathbf{H}, \tag{2.12}$$

with

$$\mathbf{H} = \int_0^{\infty}\left[\gamma(\mathrm{x}_3) - \gamma_+\right]dx_3 + \int_{-\infty}^{0}\left[\gamma(\mathrm{x}_3) - \gamma_-\right]dx_3 . \tag{2.13}$$

In the case of isotropic bimaterials with Lamé constants $\lambda_{\pm}$ and $\mu_{\pm}$, the inplane biaxial stress is given by $\Sigma^{s}_{\alpha\alpha}/2$, where

$$\Sigma^{s}_{\alpha\alpha} = \Gamma^{(1)}_{\alpha\alpha} + 2K_S \varepsilon^{s}_{\kappa\kappa} + \frac{4K_S \nu_S}{E_T} \sigma^{t}_{3} \tag{2.14}$$

Clearly, K_S is the plane stress bi-axial bulk modulus of the interface. The individual components of the interfacial excess stress tensor are

$$\Sigma^{s}_{11} = \Gamma^{(1)}_{11} + (K_S - \mu_S)\varepsilon^{s}_{\kappa\kappa} + 2\mu_S \varepsilon^{s}_{11} + \frac{2K_S \nu_S}{E_T} \sigma^{t}_{3}, \tag{2.15}$$

$$\Sigma^{s}_{22} = \Gamma^{(1)}_{11} + (K_S - \mu_S)\varepsilon^{s}_{\kappa\kappa} + 2\mu_S \varepsilon^{s}_{22} + \frac{2K_S \nu_S}{E_T} \sigma^{t}_{3}, \tag{2.16}$$

$$\Sigma^{s}_{12} = \Gamma^{(1)}_{12} + 2\mu_S \varepsilon^{s}_{12}. \tag{2.17}$$

The given equations can be simplified for a 1-D case. The indentations are assumed to cause a 1-D deformation in the elastic limits at low loads. For the case of isotropic solid, the interfacial isotropic elasticity formulation gives the final form of interfacial mismatch stress components as

$$\Sigma^{S} = \Gamma^{(1)} - \lambda^{*,S} \varepsilon^{m,S} - 2\mu^{*,S} \varepsilon^{m,S} + \lambda^{S} \varepsilon^{S} + 2\mu^{S} \varepsilon^{S} + \frac{2K^{S} \nu^{S}}{E^{\perp}} \sigma^{\perp}. \tag{2.18}$$

Here, Σ^{S} is the in-plane interfacial mismatch stress in the direction of indentation. $\Gamma^{(1)}$ is the elastic stress component. λ and μ are lame's constant with '*' denoting the interfacial components. $E^{\perp}$ and $\sigma^{\perp}$ are the transversal components modulus and stress. K^{S} is the in-plane bi-axial modulus. ν is the poisson's ratio, ε^{S} is the in-plane strain and $\varepsilon^{m,S}$ is the interfacial mismatch strain. In the present case we are only looking at the normal component of the interfacial mismatch stresses (component in the direction of indentation). The derivation for this equation can be found in the given references. Considering the case when the in-plane mismatch strains are ignored, the equation can be simplified as

$$\Sigma^{S} = \Gamma^{(1)} + \lambda^{S}\varepsilon^{S} + 2\mu^{S}\varepsilon^{S} + \frac{2K^{S}\nu^{S}}{E^{\perp}}\sigma^{\perp}. \tag{2.19}$$

The $\Gamma^{(1)}$ is the applied stress during the dynamic indentation. ε^{S} is the strain calculated from the dynamic indentation data. The material properties for the interface and bulk materials are obtained from the tensile tests. $\sigma^{\perp}$ is calculated by dividing the applied load with the surface area of the cube corner indenter and the taking its component in the transverse direction. This method provides the way to account for the transverse stresses in the interfaces along with the in-plane strain contribution.

In an another study, a method to calculate the stresses of interfaces with vanishing thickness was presented by *Ustinov et al.* [109] .The authors describe surfaces and interfaces as transversally isotropic to the interface normal. The variation of density of every volumetric surface value (such as energy and stress) is understood as the integral of the excess of the corresponding value over the interface (or surface) area over the normal direction to the interface (surface). The conditions of compatibility and equilibrium for an interface between the bulk phases A and B are introduced as:

$$\delta\epsilon_{ij}^{||} = \delta\epsilon_{ij}^{||A} = \delta\epsilon_{ij}^{||B} \tag{2.20}$$

$$\sigma_{ij}^{\perp} = \sigma_{ij}^{\perp A} = \sigma_{ij}^{\perp B} \tag{2.21}$$

The first condition means, that the strains in the interface plane (x, y)

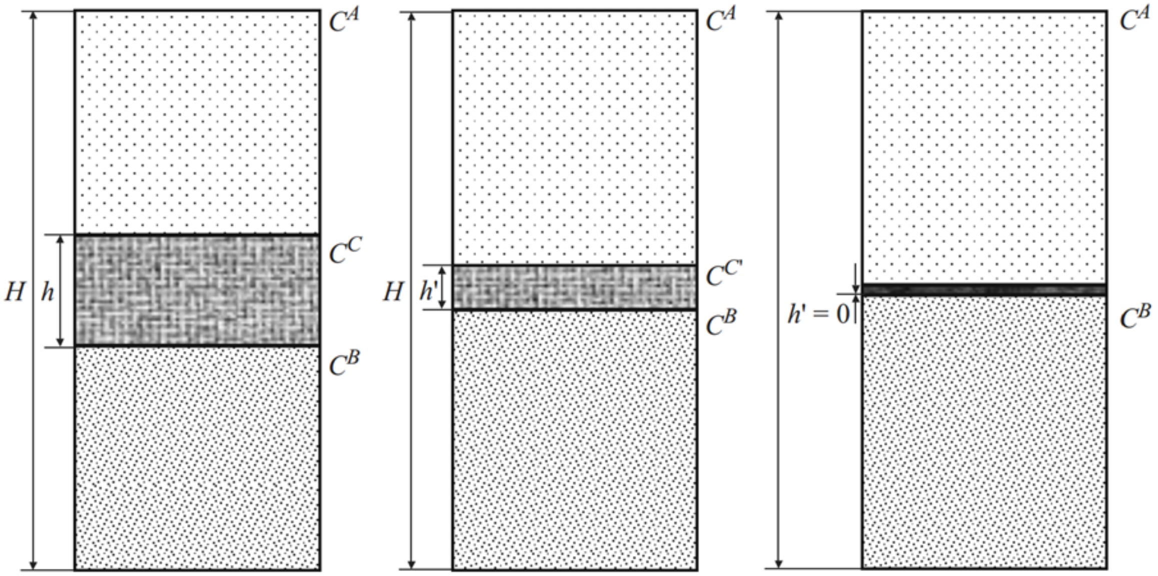

Fig. 2-2. Schematic of the interfaces used for elastic constant determination. Three layered material of the initial step (left) and modified intermediate layer C' (middle) with vanishing thickness h’

Using the two index notation as in the previous sections, a three layered elastic, transverse isotropic material is described by a set of constants $C_{11}^i, C_{12}^i, C_{13}^i, C_{33}^i, C_{44}^i, C_{66}^i = \left(C_{11}^i - C_{22}^i\right)/2$. The alphabetic character i refers to the respective layers. For the intermediate layer with the thickness h, we designate $i = C$. Analogously, we designate $i = A$ for the upper and $i = B$ for the lower layer. The $z-$ axis is assumed to be normal to the interfacial area, x and y are in-plane to the interface. In the following, a homogeneous loading of the considered structure is assumed. The elastic energy of the system is described as

$$U = U_0 + \frac{h}{2}\begin{bmatrix} C_{11}^C\left(\epsilon_{xx}^{C\,2}+\epsilon_{yy}^{C\,2}\right)+2C_{12}^C\epsilon_{xx}^C\epsilon_{yy}^C+2C_{13}^C\epsilon_{zz}^C\left(\epsilon_{xx}^C+\epsilon_{yy}^C\right)+C_{33}^C\epsilon_{zz}^{C\,2} \\ +C_{66}^C\epsilon_{66}^{C\,2}+C_{44}^C\left(\epsilon_{yz}^{C\,2}+\epsilon_{xz}^{C\,2}\right) \end{bmatrix}.$$

(2.22)

In this equation, U_0 is the elastic energy of the upper and lower layers. Authors replaced the intermediate layer C in a next step by three new layers, where the thickness of the new intermediate layer with the elastic constants $C_{ij}^{'}$ is $h' < h$ (Fig. 2-2). The new upper and lower layers of the initial intermediate layer have the elastic constants of the initial upper and lower layers. The constants $C_{ij}^{'}$ of the modified intermediate layer are chosen so, that the overall elastic energy of the system remains the same. Now, the thickness h' is reduced stepwise towards zero and the elastic constants of the layer are adjusted simultaneously. A new two layered system with additional interface elastic constants is obtained. Its elastic energy is

$$\begin{aligned}
U_{\text{eff}} = U_0 + \frac{h-h'}{4}[& C_{11}^{A}\left(\epsilon_{xx}^{A\,2} + \epsilon_{yy}^{A\,2}\right) + 2C_{12}^{A}\epsilon_{xx}^{A}\epsilon_{yy}^{A} + 2C_{xz}^{A}\epsilon_{zz}^{A}\left(\epsilon_{xx}^{A} + \epsilon_{yy}^{A}\right) \\
& + C_{33}^{A}\epsilon_{zz}^{A\,2} + C_{66}^{A}\epsilon_{xy}^{A\,2} + C_{44}^{A}\left(\epsilon_{yz}^{A\,2} + \epsilon_{xz}^{A\,2}\right) + C_{11}^{B}\left(\epsilon_{xx}^{B\,2} + \epsilon_{yy}^{B\,2}\right) \\
& + 2C_{12}^{B}\epsilon_{xx}^{B}\epsilon_{yy}^{B} + 2C_{13}^{B}\epsilon_{zz}^{B}\left(\epsilon_{xx}^{B} + \epsilon_{yy}^{B}\right) + C_{33}^{B}\epsilon_{zz}^{B\,2} + C_{66}^{B}\epsilon_{66}^{B\,2} \\
& + C_{44}^{B}\left(\epsilon_{yz}^{B\,2} + \epsilon_{xz}^{B\,2}\right) + \frac{h'}{2}[C_{11}^{C'}\left(\epsilon_{xx}^{C'2} + \epsilon_{yy}^{C'2}\right) + 2C_{12}^{C'}\epsilon_{xx}^{C'}\epsilon_{yy}^{C'} \\
& + C_{13}^{C'}\epsilon_{zz}^{C'}\left(\epsilon_{xx}^{C'} + \epsilon_{yy}^{C'}\right) + C_{33}^{C'}\epsilon_{zz}^{C'2} + C_{66}^{C'}\epsilon_{xy}^{C'2} \\
& + C_{44}^{C'}\left(\epsilon_{yz}^{C'2} + \epsilon_{xz}^{C'2}\right)]
\end{aligned} \quad . \tag{2.23}$$

While the longitudinal strains $\epsilon_{xx}^{C'}, \epsilon_{yy}^{C'}$ and $\epsilon_{xy}^{C'}$ stay the same as for the initial system

$$\begin{aligned}
\epsilon_{xx}^{A} = \epsilon_{xx}^{B} = \epsilon_{xx}^{C} = \epsilon_{xx}^{C'} = \epsilon_{xx}, \\
\epsilon_{yy}^{A} = \epsilon_{yy}^{B} = \epsilon_{yy}^{C} = \epsilon_{yy}^{C'} = \epsilon_{yy}, \ . \\
\epsilon_{xy}^{A} = \epsilon_{xy}^{B} = \epsilon_{xy}^{C} = \epsilon_{xy}^{C'} = \epsilon_{xy}
\end{aligned} \tag{2.24}$$

The following relations for the transverse strains are presented, by claiming that the surface displacements should coincide with the initial system

$$\frac{h-h'}{2}\epsilon_{xz}^{A}+\frac{h-h'}{2}\epsilon_{xz}^{B}+h'\epsilon_{xz}^{C'}=h\epsilon_{xz}^{C} \tag{2.25}$$

$$\frac{h-h'}{2}\epsilon_{yz}^{A}+\frac{h-h'}{2}\epsilon_{yz}^{B}+h'\epsilon_{yz}^{C'}=h\epsilon_{yz}^{C}\ . \tag{2.26}$$

$$\frac{h-h'}{2}\epsilon_{zz}^{A}+\frac{h-h'}{2}\epsilon_{zz}^{B}+h'\epsilon_{zz}^{C'}=h\epsilon_{zz}^{C} \tag{2.27}$$

By substituting equation (2.25)-(2.27) in (2.23) the elastic energy of the modified system is expressed in terms of the strains of the initial system. Solving the equation system which results by equating U to U_{eff} after performing the limit transition $h' \rightarrow 0$ the elastic properties A_{ij} of the interface with vanishing thickness can be expressed as:

$$A_{11}=A_{22}=A_{12}+2A_{66}\ , \tag{2.28}$$

$$A_{12}=A_{21}=\frac{h}{4C_{33}^{A}C_{33}^{B}-2C_{33}^{C}\left(C_{33}^{A}+C_{33}^{B}\right)}\left[\begin{array}{l} C_{13}^{B\,2}\left(2C_{33}^{A}-C_{33}^{C}\right)+C_{13}^{A\,2}\left(2C_{33}^{B}-C_{33}^{C}\right) \\ +2C_{13}^{C\,2}\left(C_{33}^{A}+C_{33}^{B}\right) \\ -4C_{13}^{B}C_{13}^{C}C_{33}^{A}-4C_{13}^{A}C_{13}^{C}C_{33}^{B}+2C_{13}^{A}C_{13}^{B}C_{33}^{C} \\ -\left(2C_{12}^{C}-C_{12}^{A}-C_{12}^{B}\right)\left(C_{33}^{C}\left(C_{33}^{A}+C_{33}^{B}\right)-2C_{33}^{A}C_{33}^{B}\right) \end{array}\right]$$

(2.29)

,

$$A_{13}=A_{23}=A_{33}=A_{32}=\frac{\left(C_{13}^{B}C_{33}^{A}+C_{13}^{A}C_{33}^{B}\right)C_{33}^{C}-2C_{13}^{C}C_{33}^{A}C_{33}^{B}}{C_{33}^{C}\left(C_{33}^{A}+C_{33}^{B}\right)-2C_{33}^{A}C_{33}^{B}}\ , \tag{2.30}$$

$$A_{33} = \frac{1}{h}\left(\frac{1}{C_{33}^{C}} - \frac{1}{2C_{33}^{A}} - \frac{1}{2C_{33}^{B}}\right)^{-1}, \tag{2.31}$$

$$A_{44} = A_{55} = \frac{1}{h}\left(\frac{1}{C_{44}^{C}} - \frac{1}{2C_{44}^{A}} - \frac{1}{2C_{44}^{B}}\right)^{-1}, \text{ and} \tag{2.32}$$

$$A_{66} = h\left(C_{66}^{C} - \frac{C_{66}^{A} + C_{66}^{B}}{2}\right). \tag{2.33}$$

It is evident, that these elastic constants are dependent only on the thickness of the initial layer h and not on the (vanishing) thickness h'. In the case of thickness tending to zero, these constants are defined as,

$$\begin{aligned} &A_{11} = h'C_{11}^{C'}, A_{12} = h'C_{12}^{C'}, A_{13} = C_{13}^{C'}, \\ &A_{33} = C_{33}^{C'} / h', A_{44} = C_{44}^{C'} / h', A_{66} = h'C_{13}^{C'}. \end{aligned} \tag{2.34}$$

A list of the theoretical work at the interfaces in materials is presented in Table 2-3. The table lists the key aspects, and authors by year. Even though the list does not contain each and every possible article in the literature, it gives the reader a general overview of the theoretical background on the interface mechanics formulations available in the literature on biomaterials, metals, composites and ceramics.

Table 2-3 List of theoretical research at the interfaces in materials**.**

Year	Key aspects	Authors
2014	Transverse Interfacial stresses	Dingreville et al . [106]
2013	Interface elastic constants for finite thickness	Ustinov et al. [109]
2010	Surface/interface stress effect	Zhang et al. [110]

Table 2-3 continued

2009	Interface elastic constants by a semi analytical approach	Dingreville et al.[111]
2008	Interfacial Excess Energy	Dingreville et al. [107]
2005	Size dependent elastic constants	Duan et al. [112]
2005	Surface free energy in elasticity	Dingreville et al.[108]
2004	Surface/interface bulk elasticity	Sharma and Ghanti. [103]
1998	Interface stress at atomic level	Nix and Gao [113]
1997	Interfacial nanostructured materials	Cammarata et al. [105]
1970	Diffusion at grain boundary	Cahn [114]
1975	Surface stress continuum formulation	Gurtin and Murdoch [102]
1953	Surface energy and surface stress	Herring [115]
1950	Surface stress continuum formulation	Shuttleworth [101]
1928	Surface Energy	Gibbs [100]

2.4 Current Techniques/literature Review

It is well established that a material exhibits changes in its constitutive response as a function of changes in temperature, length scale of analyses, and strain rates, [1, 2, 116, 117]. The material damage under different impact scenarios such as due to sand particles, various projectiles etc. occur via different deformation mechanisms. An understanding of such mechanisms is required to develop new constitutive laws. A number of constitutive deformation laws for polycrystalline materials are available in literature for dynamic loading [118]. Recently, the focus has shifted on developing these models for the dynamic loading failure in interfaces to determining the material failure [118]. The current work aims at investigating interface failure under micro scale dynamic impacts. There are several material constitutive models available to understand the strain rate effect on material's dynamic strength and failure [119-122]. The impact damage propagates inside a material via stress or shock waves causing large inelastic deformation. Development of material models for such deformation cases requires precise experiments because of smaller temporal and spatial resolution required. One such example is the split Hopkinson bar experiment for intermediate strain rate experiments in tensile, torsion, and compression modes [123]. The experimental procedure involves impacting bulk material samples and measuring average stress-strain response for the whole sample. The development of nanoindentation techniques in the last few decades has enabled measurement of nanoscale to microscale material site-specific behavior such as an interface sandwiched between two materials [124]. The present work focuses on using a small-scale impact test based on nanoindentation at high strain rates to measure strain rate dependent interface constitutive behavior.

The interface deformation description has been of interest since Gibbs work on the surface energy [100]. The interfacial failure is significantly dependent on the surface and interface stress. The plastic deformation of interfaces should also take into account stress mismatch because of the material property differences on either side of interfaces. In the case of nanomaterials, surface and interface stresses become significantly important owing to the significantly high surface to volume ratio. As described by Zhang et. al. [110], the interface stress consists of two parts, both arising from the distorted atomic structure near the interface: the first part, independent of the deformation of solids, is the interface residual stress, and the second part which contributes to the stress field related to the deformation is related to the interface elasticity. Interface plastic deformation, particularly the initial yield point is sensitive to the local strain (or local stress) of a heterogeneous material, which includes both the local surface or interface residual stress and local stress–strain relationship. The concepts of dividing surface, interfacial excess energy, and interfacial stress were initially introduced by Gibbs [100]. Interface excess energy is directly related to interface mismatch stress with both having origin in orientation mismatch at interface. For example, if an interface is considered as a sharp zero thickness entity then the interface excesses thermodynamic quantitates would be the difference between the bulk phase and interface properties in a three- dimensional continuum. The excess amount is associated only with the dividing surface. Based on such postulate, surface stress formulations were developed for continuum mechanics by Shuttleworth [101] relating the interfacial excess energy to surface stress [101]. The formulation were further modified by Gurtin and coworkers to find relations between the surface and body stresses [102]. Such relations have been widely used and modified in the recent years by Sharma et al. [103], Yang et al. [104], Cammarata et al. [105] etc. Dingerville and Qu [107] relating surface stress at interface with interface in-plane strain and in-plane stresses based on the modification of Shuttleworth and Herring model, applicable to coherent interfaces and recently extended to include some degree of incoherency. In the present case the analyzed interface is of finite thickness made up of a different material compared to the adjacent phases. The response of interfaces under dynamic and quasistatic loading is modeled in this work by developing a dynamic response constitutive model. A quick look at the literature gives different dynamic strength models applicable to various strain rate ranges. The most popular models that cover the whole range of strain rates in dynamic loading experiments were developed by Steinberg-Guinan (SG) [119], Johnson-Cook(JC) [120], Steinberg and Lund (SL) [122], Zerilli and Armstrong (ZA) [121], and Fallansbee and Kocks [125] etc. The SG model is applicable for 1D plate experiments with limitations such as not being able to capture the evolving history. The ZA model and mechanical threshold stress (MTS) model of Fallansbee and Kocks [125] have their own advantages such as applicability at higher strain rates and describing the viscoplastic response up to strain rates of 10^4 s^{-1}. The JC model is an empirical relation to describe the flow stress dependency on the strain rate, plastic strain, and temperature change with applicability up to strain rates of 10^4 s^{-1}.

To account for the confinement effects, the residual confinement stresses in the interfaces are measured using the Nanomechanical Raman spectroscopy experiments. There are other techniques, for example, destructive techniques with higher precision (nano scale) are transmission electron microscopy (TEM), methods such as electron diffraction contrast imaging (XTEM) and convergent beam electron diffraction (CBED). These techniques are expensive and require destructive elaborated specimen preparation [126]. The latter causes an extensive modelling for the interpretation of the XTEM images [127]. Raman spectroscopy, which was originally used to obtain information about the chemical composition and crystallinity of the examined sample, was later found to be sensitive to applied stresses too. A relationship between the Raman peak and the applied loads was first found by E. Anastassakis, A. Pinczuk *et al*. [128] who applied uniaxial stresses along the]

$[0|0|1]$ and $[1|1|1]$ planes of silicon. The external load cause splitting and shift of the Raman peaks from which correlation coefficients were obtained. Raman spectroscopy has become a popular non-destructive stress measuring technique due to the presence of correlation between mechanical stresses and the Raman peak. This technique has been used in the literature to measure stresses in the crystalline materials such as Silicon [129] and polymers such as epoxy [130]. The JC model is therefore updated in the current article to account for both confinement effect and strain rate effect. In order to understand the underlying mechanisms of deformation and to measure constitutive response of interfaces, characterization techniques with sufficient resolution are needed. The interface properties of an epoxy interfaces between glass plates are investigated by nano and micro scale impact experiments.

CHAPTER 3. METHODS

3.1 Nanoindentation

Nanoindentation is one of the preferred method to measure the mechanical properties of small volume materials at nano-micro scale. The interfaces investigated in this study are very thin which requires techniques better than the traditional uniaxial mechanical loading tests. Nanoindentation experiments have the ability to measure properties at desired sites such as grains and grain boundaries without any significant sample preparation. This makes nanoindentation an excellent tool to perform elastic-plastic property measurements at nano and micro-scales in the current experiments. The experiments are performed by indenting the interfaces at predefined peak load ($P_{\max}$) by stepwise increase in the load or peak depth ($h_{\max}$) by increasing the depth in small steps. A spherical indenter was used for performing the indentations and the unloading portion of the curve was used for calculating the mechanical properties from contact mechanics framework [131, 132]. The maximum indentation load $P_{\max}$ and the corresponding are of indentation A was measured during experiments. The hardness, H is given as

$$H = \frac{P_{\max}}{A}. \tag{3.1}$$

Here, A for a spherical indenter is related to the contact depth radius a_c given as

$$A = 3.14 a_c^2. \tag{3.2}$$

The reduced modulus, E_r is derived from the slope of the upper portion of the unloading curve as

$$S = \frac{dP}{dh} = 1.17 E_r \sqrt{A}. \tag{3.3}$$

Here, S is the stiffness measured from the slope of unloading portion of the curve. E_r is then used to find the material modulus given by the relation,

$$\frac{1}{E_r} = \frac{(1-\nu^2)}{E} + \frac{(1-\nu_i^2)}{E_i}. \tag{3.4}$$

Here, E and ν are the Young's modulus and the Poisson's ratio of the specimen under examination. E_i and ν_i are respectively the Young's modulus and the Poisson's ratio of the indenter. More details on these procedures can be found in the author's earlier articles [2, 3].

The load-displacement data was further analyzed to find the stress-strain behavior of the material. The contact depth was calculated from the indentation depth using equation(3.5),

$$h_c = h - 0.5\left[\frac{3P}{4E^*}\right]^{2/3}\left[\frac{1}{R}\right]^{1/3}. \tag{3.5}$$

Here, P is the applied load, h is the indentation depth, E^* is the modulus of material from the experiments, and R is the radius of the indenter.

The contact radius a_c was measured by equation (3.6) given as

$$a_c = \sqrt{2h_c R - h_c^2}. \tag{3.6}$$

The indentation stress and strain were then defined by equation (3.7) as

$$\sigma_{ind} = \frac{P}{\pi a_c^2}, \quad \epsilon_{ind} = \frac{4h_e}{3\pi a_c}. \tag{3.7}$$

Here, $h_e = h - h_c$ is the elastic depth of indentation. These stresses and strains were also corrected for the zero load and zero displacement. Reader can find more details on the procedures in the articles by S. R. Kalidindi [133]. The experimental set up is a multi-module mechanical testing instrument from NanoTest, Micro Materials Ltd., platform 2, shown in Fig. 3-1. The experimental set up consist of a 3D stage that allows it to move in x, y and z directions with nanometer precision. The instrument has a vertical pendulum with an indenter. The pendulum hangs on frictionless springs which indents during experiments in the horizontal direction. The force on the pendulum is applied through the electro-magnets located on the top of the pendulum. The depth of the indents is measured by the capacitance plates located behind the indenter. Authors have used the same experimental setup in their earlier studies for various materials characterization. More details on the equipment can be found in earlier articles by the authors in the following references [10, 11].

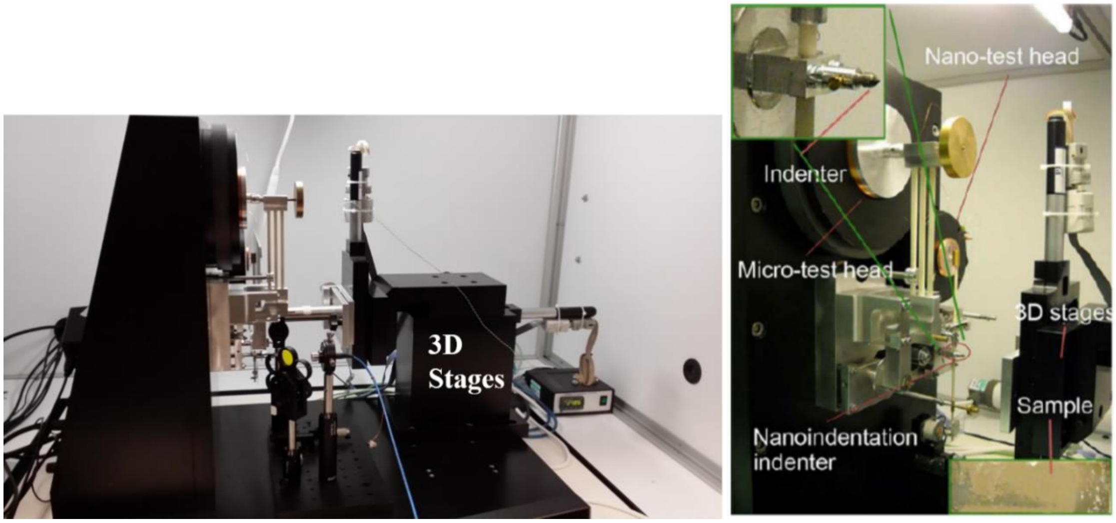

Fig. 3-1. Instrument set up, NanoTest, Micro Materials Ltd.

The samples were glued firmly to the substrate to avoid any displacements. The sample surface was observed under a microscope for any defects before mounting it on the stage. The experiments were performed at $25\,^{o}C$. One of the most challenging task is to design experiments that are reliable and repeatable. It was ensured that the same experimental conditions were present while performing experiments for long time intervals. 20 indentations were performed to get each data point. A 10 µm tip radius spherical indenter was used to perform experiments.

3.2 Nanoscale Impact

The impacts were also performed using the same set up described in the earlier section but with the high strain rate module [1]. The impacts were performed with the spherical indenter of 10 µm tip radius. The force on the pendulum was applied through a solenoid at the bottom and an electromagnet at the top from both ends of the pendulum as shown in Fig. 3-2. The instrument was resting on a vibration isolation table throughout the experiment and the temperature was kept stable. During the impacts, the pendulum was pulled from both ends by applying forces from both the electromagnet and the solenoid. For impact, the solenoid was switched off to release the pendulum to impact the predefined site. The data acquisition is similar to the nanoindentation. The position of the indenter is monitored and stored during the impacts. The displacement from the points of initial contact to the maximum penetration is considered as the maximum depth and is used in the strain rate calculations. The final depth after the impact is considered as the residual depth after the impact. The time is also recorded during the experiments corresponding to the displacement as shown in Fig. 3-3. It is used to calculate the velocity of the impacts by taking a first order derivative.

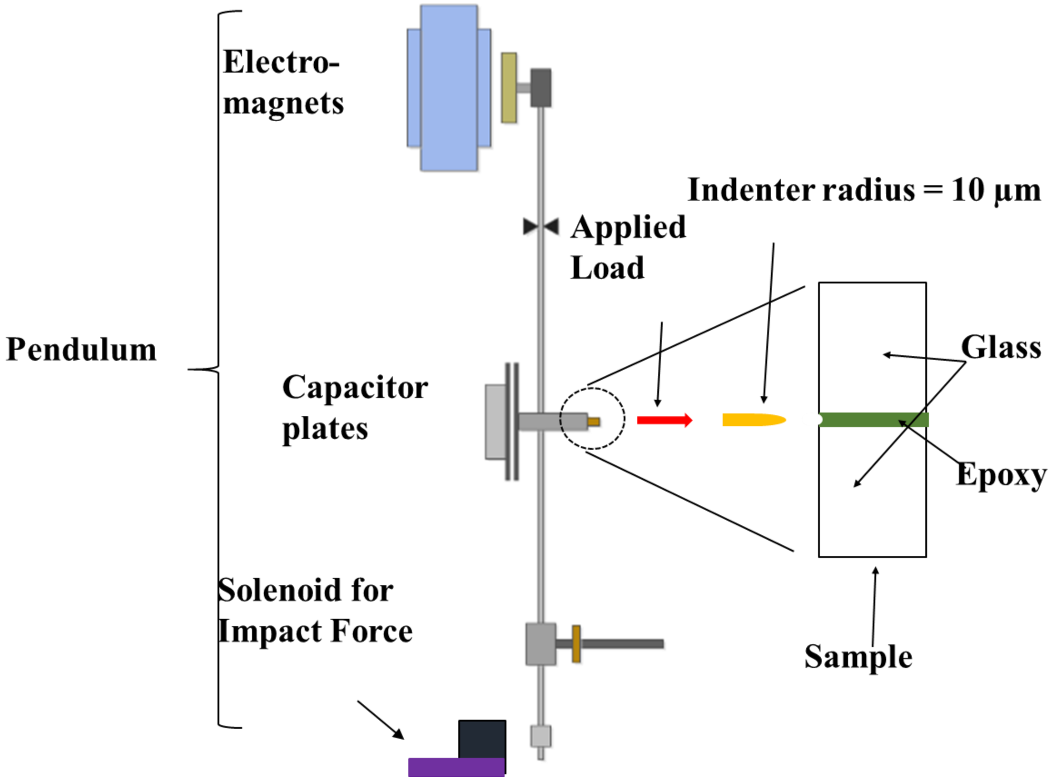

Fig. 3-2. Schematic of instrument set up for dynamic indentation tests.

The average strain rate during an impact event was approximated by equation (3.8) given as

$$\dot{\varepsilon} \approx \frac{V_{in}}{h_{\max}}. \tag{3.8}$$

Here, $h_{\max}$ is the highest depth and V_{in} is the contact velocity.

The energy absorbed in the sample deformation is calculated by equation (3.9) as [134, 135]

$$\frac{m\left(V_{in}^2 - V_{out}^2\right)}{2} = \int_0^{h_{res}} Pdh\ . \tag{3.9}$$

Here, P is the load, m is the mass of pendulum, V_{out} is the outgoing velocity and h_{res} is the residual depth. The area under the impact is given by equation(3.2). The effective dynamic hardness, H_d is given by equation (3.10) as derived by H. Somekawa and C.A. Schuh [135],

$$H_d = \frac{3m\left(V_{in}^2 - V_{out}^2\right)}{2ch_{res}^3}. \tag{3.10}$$

The strain rates during the experiments were in the range of 10 s^{-1} to 2000 s^{-1}. The strain rate in the current experiments depended on the maximum load applied at the impacts.

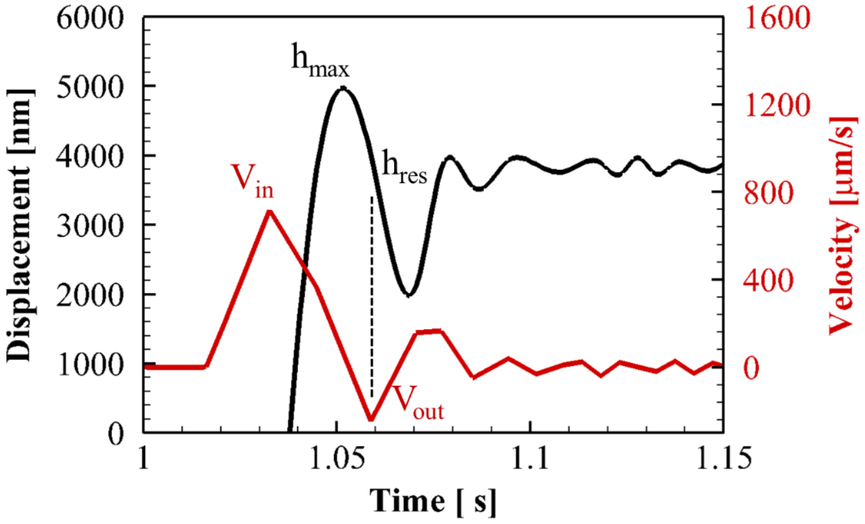

Fig. 3-3. Representative curve for impact experiment, showing h_{max}, h_{res}, V_{in}, and V_{out}.

The stress and strain were then defined by equation (3.11) as

$$\sigma_{ind} = \frac{P}{\pi h_{\max}^2}, \quad \epsilon_{ind} = \frac{h_{\max} - h_{res}}{h_{\max}}. \tag{3.11}$$

3.3 Nanomechanical Raman Spectroscopy Experiments

The Nanomechanical Raman Spectroscopy (NRS) experimental set up was used to measure the residual confinement stresses in the interface. The experimental setup for Raman spectroscopy consisted of two key instruments, a high performance laser and a high resolution CCD image sensor. The Raman laser used in this research is 514.5 nm Ar+ laser (Modu-Laser Inc, UT). The laser was redirected to the sample surface for measurement using a single mode fiber (SMF). The back-scattered laser signal was collected by the same objective and sent to the spectrometer (Acton SP2500, Princeton Instruments Inc., NJ). The Mechanical load was applied using the nanoindentation platform manufactured by Micro Materials Inc., UK with load range from 0.1 mN to 500 mN, with the accuracy of better than 0.1 mN. The experimental setup to measure the Raman signal is shown in *Fig. 3-4*.

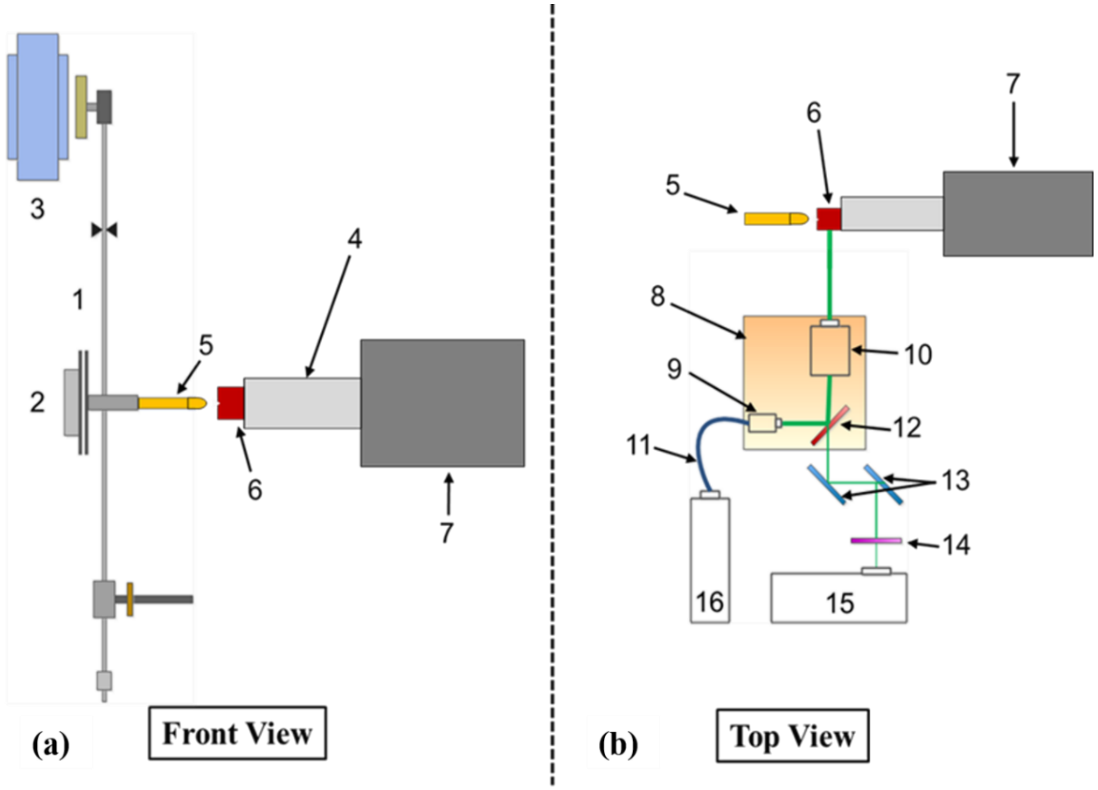

Fig. 3-4. Setup of the Nanomechanical Raman spectroscopy experiments, (a) Nano indentation in front view. (b) Raman spectroscopy setup in top view.

The spherical indenter (5) was attached to the pendulum (1). The force was applied and measured with electro magnets (3). The displacement of the indenter was measured with the capacitor plates (2). One plate was connected to the pendulum and the other one was fixed. The displacement of the pendulum changes the gap between the two plates and therefore its electrical capacity. The displacement was therefore a function of this capacitance. The sample (6) was fixed with a sample holder (4) on a stage which was moveable in three directions (7).

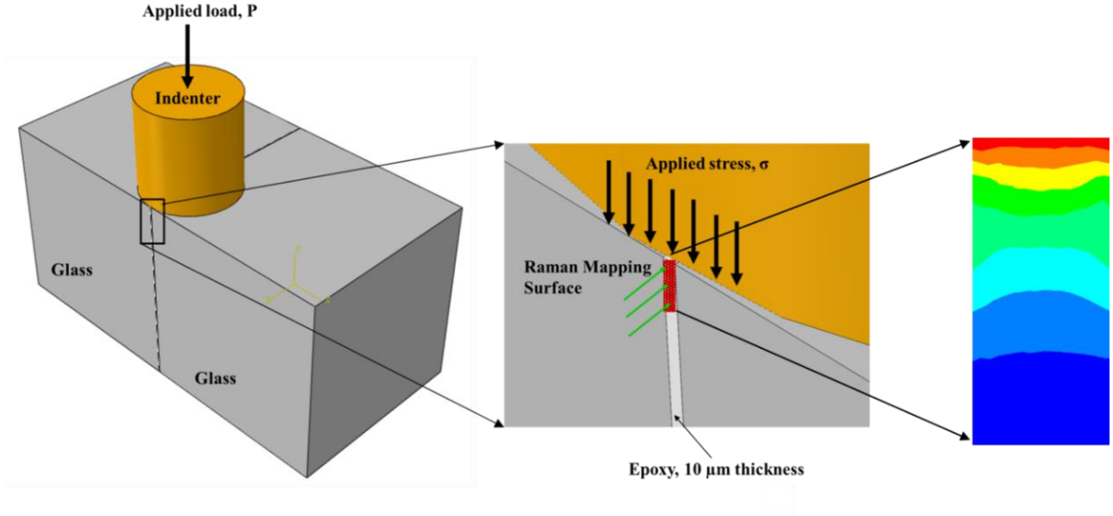

Fig. 3-5. Nanomechanical Raman spectroscopy experimental schematic describing the collection of Raman signal over the interface.

The top view in *Fig. 3-4* shows the setup of the Raman Spectroscopy. An Argon Ion Laser (16) was used as the monochromatic light source. The laser light had a wavelength of 514.5 nm. The laser light was directed to a dichroic mirror (12) which reflected the laser light directed by the optical fiber cable (11) and narrowed by a collimator(9). An objective (10) focused the light on a 2 µm area on the sample. The emitted light from the sample with a different wavelength reflected back through the dichroic mirror. The reflecting mirrors (13) were used to redirect it to a notch filter (14). This filter rejected the laser light wavelength portion of the spectrum, and transmitted all other wavelengths. An optical spectrometer (15) was placed behind the notch filter to analyze the Raman signal from the sample. The optical spectrometer resolved the signal corresponding to Raman peaks from the sample. The procedure to collect signal is as given in Fig. 3-5.

During the process, the examined material is penetrated by the monochromatic laser light. The incoming photons generate a dipole moment in the molecules of the material. The amount of the resulting moment, called polarizability, is dependent on the molecule geometry and structure and therefore on the material. The Raman tensor describes the relation between the scattering intensity and the polarizability. The induced moment causes vibrations of the molecules and the energetic level of the molecule increases to a virtual level as shown in Fig. 3-6. Oscillating dipole moments generate electrical magnetic waves. The material emits a big part of this light elastically, which means the emitted light has the same wavelength, frequency and energy as the laser light. This (elastically) reflected light is called the Rayleigh scatter. The big arrows in the figure illustrates that this elastic reflection is the most probabilistic process. Additionally, a small amount of light with other wavelengths is emitted by the material. The photons of this light collide inelastically with molecules. This causes a variation of the emitted photon energy by ΔQ. Since the energy of photons Q is correlated to its frequency f by $Q = gf$, where g is the Planck constant, the emitted light has different wavelength from the laser light. This inelastically scattered light is called the Raman Scatter and is the basis of the Raman Spectroscopy. During the collision of the photon and the molecule, the photon can add energy to the material or, in a constructive collision, the energy of the photon increases. The former case is called Stokes Scatter and the latter is called Anti-Stokes Scatter. Since the intensity of the Anti-Stokes Scatter is normally significantly smaller, a common way is to measure only the Stokes Scatter.

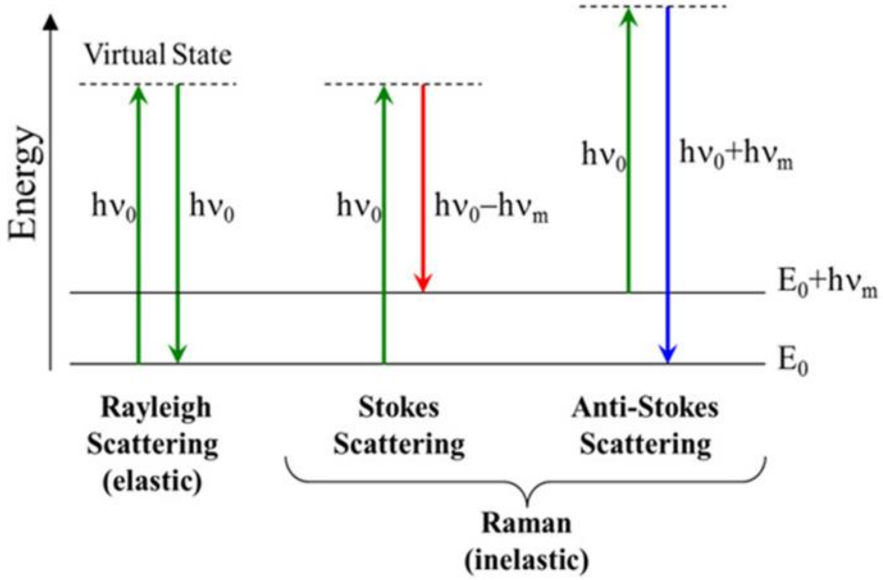

Fig. 3-6. Inelastic collisions of photons and molecules increase the energy level of the electrons to a virtual unstable state from which the energy is reduced back to a basic state by light emission

3.4 Scanning Electron Microscopy (SEM) and Energy Dispersive X-ray (EDX)

Scanning Electron Microscope (SEM) images were captured by the FEI Nova nanoSEM (FEI Company, Hillsboro, OR) located at Purdue University. The normal focus point for the Nova SEM is 5 mm. The accelerating voltage was set to 10.00 kV in a high vacuum chamber. Energy Dispersive X-ray (EDX) analysis was completed using the FEI Quanta 3D FEG Dual-beam SEM. The normal focus point for Quanta SEM is 10 mm. The accelerating voltage was 20.00 kV.

CHAPTER 4. RATE DEPENDENCE ON STRESS-STRAIN

4.1 Sample Preparation

Single interface samples of glass and epoxy were prepared with an epoxy interface sandwiched between two glass phases. The samples were prepared using two part industrial epoxy procured from Composite Polymer Design (South St. Paul, MN, USA). The resin, CPD4505A, and hardener, CPD 4507B, were thoroughly mixed in recommended proportions of 100A : 28B by weight. The epoxy layer thickness was controlled by putting tabs of appropriate thickness in between the glass slides. The interface thickness was kept at 10 µm achieved by placing the epoxy between glass slides with 10 µm tabs on the sides. The samples were cured at a prescribed temperature of 250 ^{o}F for one day. The thickness of the interface in samples was measured with a microscope to make sure that it was in the error margin of 10±0.5 µm. The sample surfaces as shown in Fig. 4-1 were polished to remove scratches that could interfere with the data measurement during experiments.

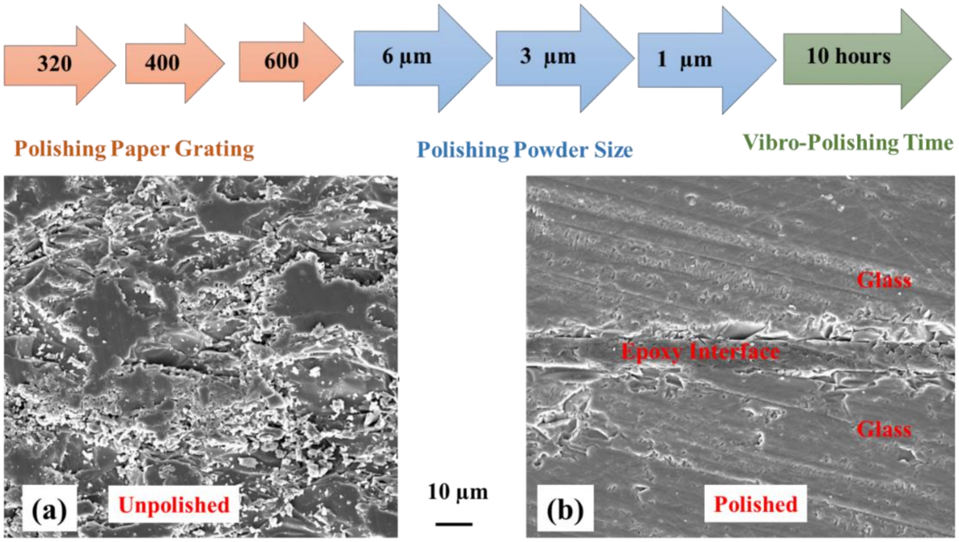

Fig. 4-1. SEM images showing Glass/Epoxy interface (a) before polishing and (b) after polishing with polishing steps listed at the top of the figure.

The EDX analysis was conducted on the samples before and after the experiments. Fig. 4-2. shows SEM image illustrating the impact marks in the middle of the on the epoxy interface. The indent marks width was in the range of 8-10 micron. The depth of the impacts was approximately 2 micron. The EDX spectrum of the surface was obtained to identify the elements. The elemental mapping on the sample surface is given in Fig. *4-3*. The sharp interface of epoxy between two glass phases is shown in Fig. *4-4*. The individual element mapping on the epoxy and glass surface is shown in Fig. *4-4* (a) and Fig. *4-4* (b) respectively.

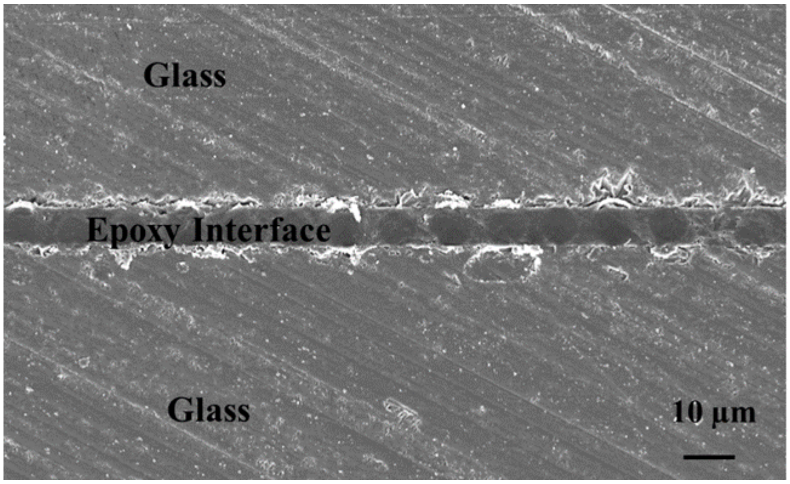

Fig. 4-2. Post impact SEM image of glass/epoxy interface.

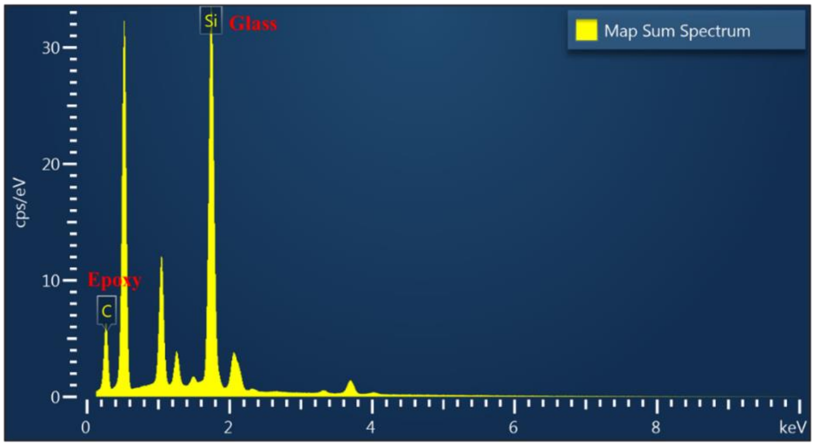

Fig. 4-3. Elemental spectrum on the surface of the sample.

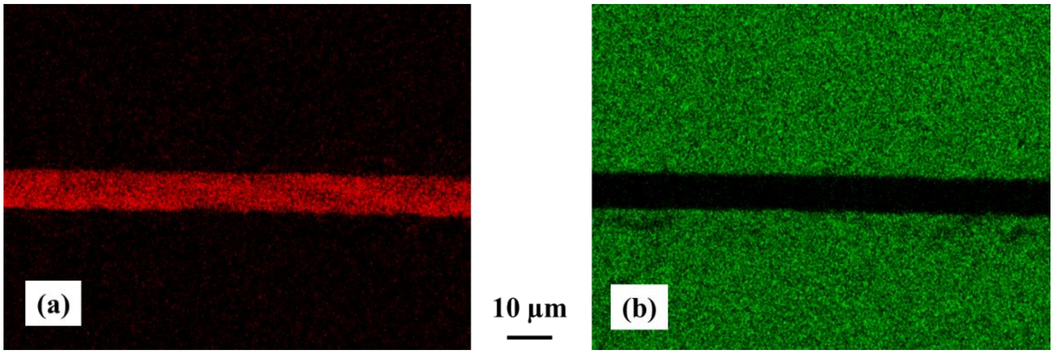

Fig. 4-4. Images showing the EDX elemental map on (a) epoxy (red) and (b) glass (green).

4.2 Statistical Analysis

The quasistatic and dynamic indentation data was post processed to calculate the stresses and strains, dynamic hardness of the interfaces, strain rates of impacts, impact depths, stresses at maximum penetration depth, impact velocity and impact energy. These calculations are subjected to experimental error, and their uncertainty depends on the experimental procedures. The error in a measurement is usually defined as the difference between its true value and the measured value. The term "uncertainty" is used to refer to "a possible value that an error may have." According to the description by Moffat RJ, the terms "uncertainty interval" and "uncertainty" are in general synonymous. They are also used in the current discussion, both referring to the interval around the measured value within which the true value is believed to lie [136]. The "uncertainty analysis" is the determination of the uncertainties in the individual measurements and their effect on the calculated results. The calculated values of dynamic hardness, strains, impact depths, etc. reflect the similar uncertainties. The bounds of uncertainty in the data collected during impact tests is shown in Fig. 4-5. The data points shown in blue color were the measured data from the experiments. The green line indicates the average value and the red lines indicate the one standard deviation variation from the average. The data points that fall under the acceptable deviation from the average were used for further analysis. The data points outside the red lines were ignored due to too much error in the measurement, probably because of errors during the experiments.

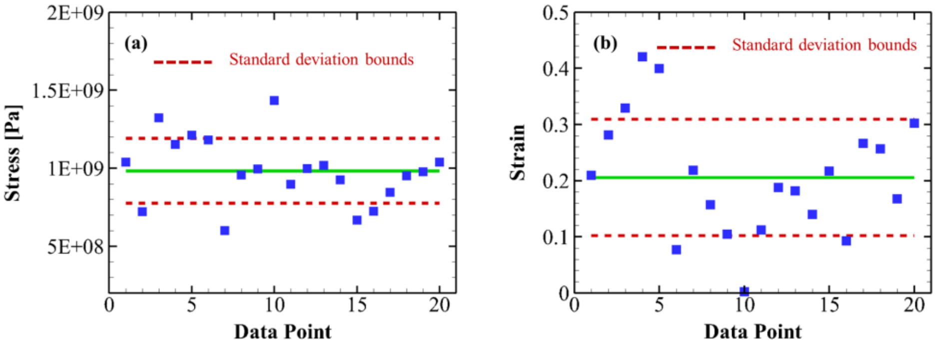

Fig. 4-5. Uncertainty analysis on the data measured from the experiments for (a) stress and (b) strain.

Statistical analysis is another way to check for the validity of the experimental data collected over a range of experiments. It helps the used to interpret the data and deduce the correlations among different variables. A statistical check was done on the data collected from the current experiments before the analysis using a statistical analysis software SAS. A regression analysis was performed by writing a SAS program to check for the correlations between dynamic hardness and other parameters of the experiment. Table 4-1 lists the correlation coefficients among dynamic hardness, residual depth, strain rate, plastic depth, stress rate and energy absorbed. The stresses were calculated at the highest plastic depth and were multiplied by the strain rates to give stress rates. The dynamic hardness has a strong negative correlation (>0.80) with residual depth. A high positive correlation was found between the strain rate and impact energy. In the case of glass/epoxy interfaces, the dynamic hardness shows an increase with the increase in the strain rate as expected as shown in Fig. 4-6. These correlations were useful to eliminate the duplicated parameters during the further analyses stages and development of viscoplastic models. The viscoplastic models will be described in further sections.

Table 4-1 A list of the correlation coefficients among dynamic hardness, strain rate, plastic depth, residual depth, stress rate, and energy absorbed at impact sites on glass/epoxy interface

	H_{dyn}	Strain rate	$h_{plastic}$	h_{res}	Stress rate	$E_{absorbed}$
H_{dyn}	1.00000	0.65238	-0.45380	-0.82190	0.65607	0.33781
Strain rate	0.65238	1.00000	-0.37223	-0.49652	0.82665	0.74555
$h_{plastic}$	-0.45380	-0.37223	1.00000	0.69329	-0.80397	0.33109
h_{res}	-0.82190	-0.49652	0.69329	1.00000	-0.66994	-0.00656
Stress rate	0.65607	0.82665	-0.80397	-0.66994	1.00000	0.25838
$E_{absorbed}$	0.33781	0.74555	0.33109	-0.00656	0.25838	1.00000

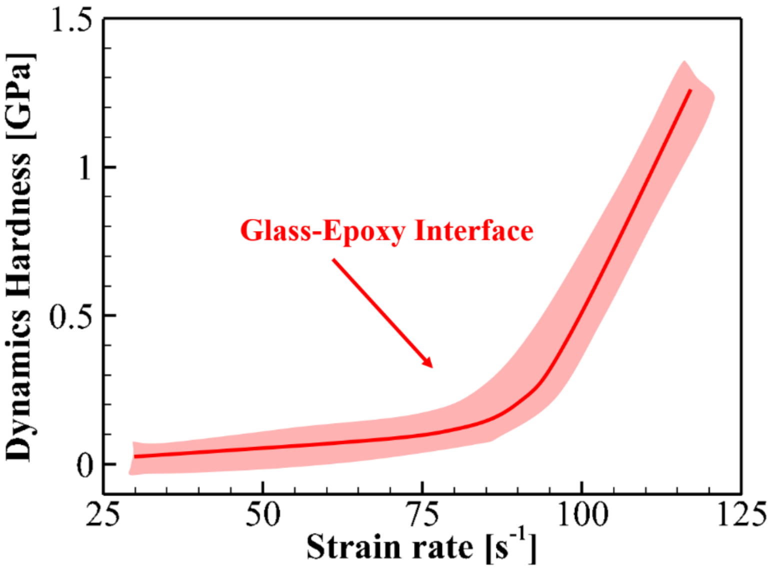

Fig. 4-6. Dynamic hardness on glass/epoxy interfaces as a function of strain rate.

4.3 Stress Strain

The dynamic strength of a material needs to be modeled appropriately depending on the strain rates of loading. The Johnson-Cook model is utilized in the present scenario to model this behavior. The JC constitutive model [120] is an empirical model, that relates the equivalent stress as a function of the strain, strain rate and temperature given by equation (4.1)as

$$\sigma = [\mathrm{A} + \mathrm{B}\varepsilon^{n}][1 + \mathrm{C}\ln\dot{\varepsilon}][1 - \mathrm{T}^{*m}]. \tag{4.1}$$

Here, σ is the equivalent stress, $\dot{\varepsilon}$ is the normalized effective plastic strain rate (normalized to strain rate of 1.0 s^{-1} in the present case), and ε is the effective plastic strain. T^{*} is defined as $T^{*} = (\mathrm{T} - \mathrm{T}_{r}) / (\mathrm{T}_{m} - T_{r})$ with T_{r} as room temperature, T is the absolute temperature, and T_{m} is the melting temperature A, B, n, C and m are material constants. The experiments were conducted at room temperature so the equation is simplified to

$$\sigma = [\mathrm{A} + \mathrm{B}\varepsilon^{n}][1 + \mathrm{C}\ln\dot{\varepsilon}]. \tag{4.2}$$

Similarly, the JC damage model is given by the equation as

$$\varepsilon_{f} = [D_{1} + D_{2}\exp(\mathrm{D}_{3}\,\sigma^{*})][1 + D_{4}\ln\dot{\varepsilon}]. \tag{4.3}$$

Here, σ^{*} is the stress triaxiality, ε_{f} is the fracture strain, D_{1} ,…, D_{5} are material constants.

The stress strain data corresponding to each red point comes from a single impact point. Each impact instant during the experiment gives the depth and velocity of the impact which was used to calculate the stress and strain of that point. This method of extracting the stress strain data from impact experiments is well document in the literature and have been used for years [137, 138]. The stresses for the strains from 0.2 to 0.4 was measured during dynamic indentation experiments. The contact radius divided by the indenter radius is defined at the indentation strain [139, 140]. The JC model equation is fitted to this range of strains with an normalized strain rate of 300 s^{-1}. Table 4-2. lists the JC parameters obtained from the current fit. The yield stress value shown in the table is high compared to the value for normal epoxy. The reason for this is that the confinement effect also plays a major role during that deformation and it is not considered in the given equation. It is later discussed in the next chapter and the confinement effect is quantified. The deformation mechanisms of in high strain regimes depends on strain rates, microstructure, grain boundaries orientations, and dislocation movements [141]. The present analyses concludes that the JC model alone is not sufficient to model the dynamic behavior of interface. Therefore, there is a need to extend the current JC model to be able to predict the mechanisms of interfaces deformation correctly. The JC parameters were calculated from the experimental data.

Table 4-2 Johnson-Cook material parameters for the epoxy interfaces.

Strain hardening		Damage parameters	
A (MPa)	251	D_1	-0.219
B (MPa)	1130	D_2	0.366
C	0.018	D_3	0.212
n	0.33	D_4	0.556

Although the Johnson-Cook model is useful to describe the dynamic effects in materials, it is only applicable in higher strain rate regimes. The other limitation of JC model is the large no. of material parameters that needs a lot of experimental data. A new viscoplastic model that could capture the strain rate dependency over large strain rate ranges and is relatively easy to implement was sought in the current study. It is well stablished as given in the article by L.M. Taylor et. al., that the strength of the material changes with strain rates and thus strain rate should be included in the material modeling [142]. Materials exhibit considerable increase in the yield strain with increasing rate of strain which leads to the increase of material ductility. A brief search through literature revealed several models that could describe the behavior of polymeric material such as epoxy. E Kontou et. al., examined the tensile behavior of epoxy-glass fiber composites and developed a 3D viscoplastic model [143]. They developed a model to describe the nonlinear, strain rate-dependent behavior in anisotropic materials. Q. Bing et. al.. developed a technique to conduct compression experiments on carbon fiber composites to characterize their strain rate dependent behavior [144]. The rate-dependent constitutive model and the microbuckling model for the composites predicted the compressive strengths very accurately. In yet another study by A.D. Mulliken et. al., two polymers were compared at strain rate from 10^{-4} s^{-1} to 10^{4} s^{-1} in uniaxial tension and compression experiments by a dynamic mechanical analyzer (DMA) [145]. In more recent studies, the compressive deformation of low-density polymeric foams at different strain rates was characterized by A. Yonezu et. al.[146]. They proposed a constitutive equation for plastic deformation of polymer materials with strain rate dependence which could predict time-dependent properties of porous materials subjected to uniaxial compression and indentation loadings. R. Dou et. al., used Cowper-Symonds model as the constitutive model to study the properties of aluminum alloy with an account of compression behavior and strain rate effects[147]. All previously mentioned models employ many material parameters to model the strain rate effect. In the present case, we have chosen the viscoplastic model developed by J.Tsai and C.T. Sun defined by a simple power law [148]. They observed that the elastic deformation of the material was not affected significantly by strain rates but the plastic deformation was significantly affected by strain rates. They developed a viscoplastic model from low strain rate data that also fits the high strain rate. The stress-strain curve was fitted by equation (4.4) given as

$$\bar{\varepsilon}^{p} = A\left(\bar{\sigma}\right)^{n}. \tag{4.4}$$

Here, the amplitude A is function of strain rate, which can be expressed by equation (4.5) given as

$$A = \chi\left(\dot{\bar{\varepsilon}}^{p}\right)^{m}. \tag{4.5}$$

The material parameter χ and m were determined from the data corresponding to the plastic deformation part by plotting the amplitude A as a function of plastic strain rate on the log-log scale as shown in Fig. 4-7. The viscoplastic parameters obtained from the experimental data for glass/epoxy interfaces are given in Table 4-3. The stress-strain curves for quasistatic and dynamic loading are shown in Fig. 4-8. As expected the dynamic strength of material is higher in comparison to the quasistatic strength.

Table 4-3 Viscoplasticity parameters for epoxy interface.

χ (MPa)$^{-n}$	1.58E-13
m	-0.28
n	1.4

The viscoplastic model fit is also plotted on the Fig. 4-8 using the equation(4.4). The stress-strain curves from this model is later compared to the model developed in this article in further

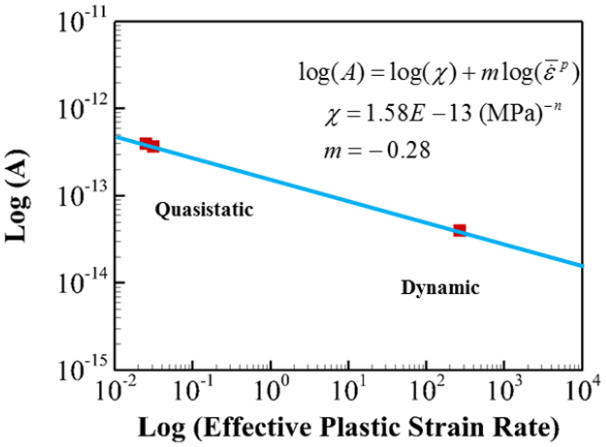

Fig. 4-7. Plot to determine the amplitude A for glass epoxy interface.

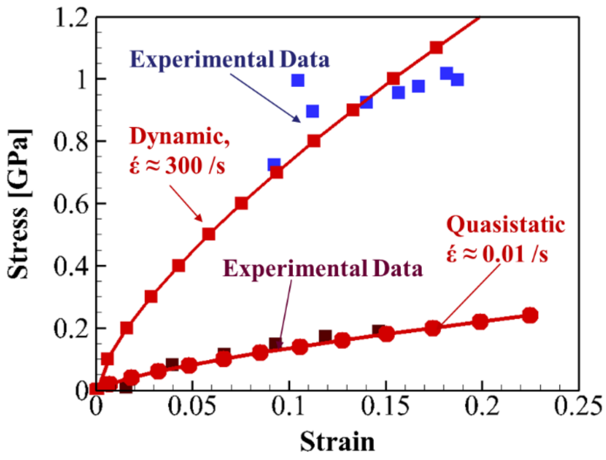

Fig. 4-8. Stress–strain curves for glass/epoxy interface for quasistatic and dynamic loading.

CHAPTER 5. CONFINEMENT EFFECT IN INTERFACES

5.1 Confinement Law

The material deformation under the effect of compressive stresses changes from its normal behavior. This phenomenon has been long established since first introduced by Richard et. al. in 1928, with his proposed linear relation given in equation (5.1), for the compressive strength of confined and unconfined material under lateral confinement stress σ with k as material constant[149]

$$f_{cc} = f_c + k.\sigma. \tag{5.1}$$

Here, f_{cc} is the confined compressive strength and f_c is the unconfined strength.

Since then there had been huge attempts to modify the equation (5.1) to make predictions more accurate and to propose the value of the constant k [150].

Interfaces in composite materials can be considered as a material phase confined between two separate grains or phases. Mechanical strength of materials in confined spaces has been shown to be strongly affected by lateral stresses [149]. Such confinement effects has been utilized in applications such as brittle materials for armor applications where brittle materials are kept under high confinement stresses. Most of the research on the effect of confinement is in the area of concrete with a goal to increase the strength of structures made of concrete. D. R. Mc Creath et. al. [151] studied response of concrete under increasing lateral compressive stress and found that increasing compressive strength of the concrete as a function of applied lateral stress. Experimental studies found that the load carrying capacity and ductility of concrete columns increased by the application of composite wraps in axial compression. It can also renew deteriorated structure and improve seismic resistance [152]. Effect of hoop reinforcement on the strength of concrete column studied by Y.P. Sun et. al., revealed that the hoops with intermediate hoops or crossties exhibited higher increase in the concrete strength and more ductile behavior compared to perimeter hoops [153]. Stress strain behavior of the concrete columns under various confinements was also studied with recently improved models for confined compressive strength proposed by Y. Sun. It was applied in the case of rectangular or circular confinement by accounting for the volumetric ration, the yield strength, the thickness and the outside dimension of confinement [154]. These models predicts the stress strain response of the confined material up to very large strains. Veysel et. al. [155], proposed a simple model predicting the effect of fiber reinforced polymer (FRP) confinement to the increase of compressive strength and axial deformation capacity of concrete which could also be extended to hollow cylinders confinement. Various analysis techniques have been adopted to be able to model these problems such as nonlinear fiber element analysis [156], crack formation process with pre and post peak behavior in confinement [157], stress strain model for compressive fracture [158], the fracture mode changes in armor materials [159], and the lateral expansion associated with the compression [160].

The confinement effect in the current case is investigated by comparing the stress strain behavior of epoxy in the interface confined between two glass slides with the stress strain behavior of unconfined epoxy. The data for the unconfined epoxy for different strain rates was obtained from the article by L. Bardella [161]. The viscoplastic model was fitted to this data to find the viscoplastic parameters. The viscoplastic parameters obtained from the experimental data for glass/epoxy interfaces are given in Table 5-1. The stress strain curves for unconfined epoxy for quasistatic and dynamic loading are given in Fig. 5-1.

Table 5-1 Viscoplasticity parameters for unconfined epoxy.

χ (MPa)$^{-n}$	6.37E-14
m	-0.0456
n	1.5

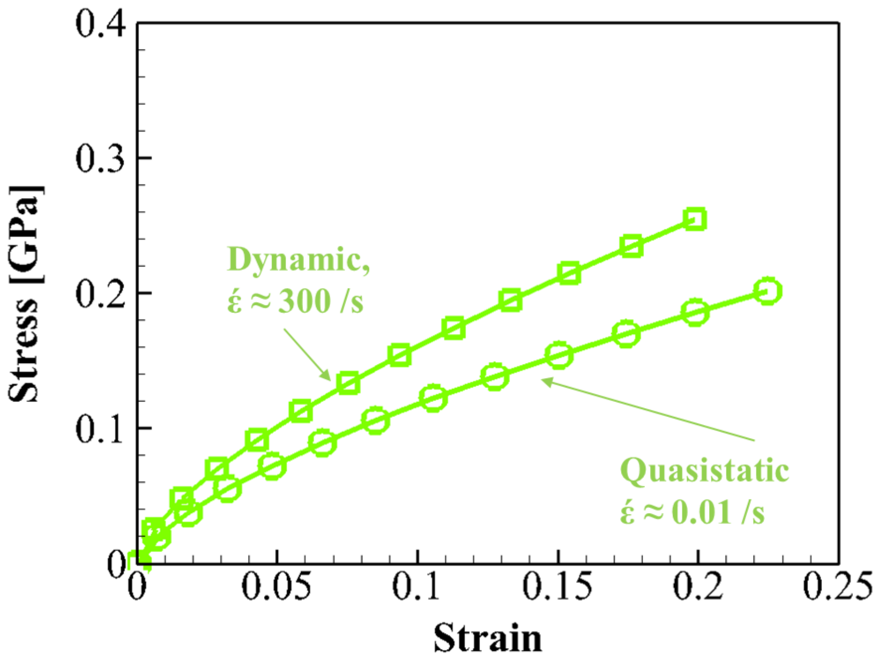

Fig. 5-1. Stress–strain curves for unconfined epoxy for quasistatic and dynamic loading

The confined epoxy state in the glass/epoxy interface and the unconfined epoxy is compared for both the quasistatic and dynamic cases. The interfaces exhibited higher compressive strength as compared to the unconfined epoxy. Moreover, the effect of confinement is much higher in the case of dynamic loading as shown in Fig. 5-2. This difference is attributed to the factors such as the increase in the material strength via strain hardening and also because of the increased compressive strength due to the presence of residual stresses.

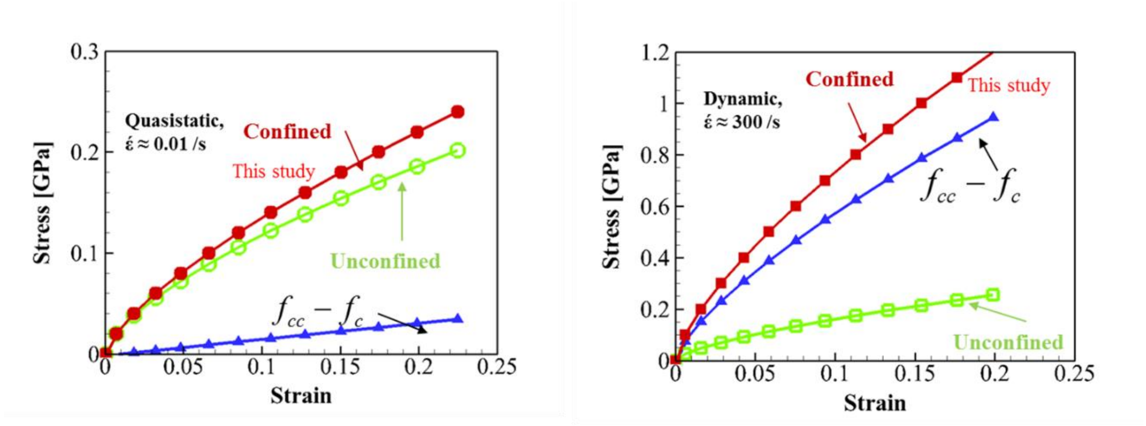

(a) **(b)**

Fig. 5-2. Difference in compressive strength between confined and unconfined state in (a) quasistatic and (b) dynamic loading.

5.2 Analytical Solution for Confinement Stresses

As mentioned earlier, it is difficult to measure the lateral stresses during the indentation experiments with the current techniques but the lateral stress information is needed to be able to quantify the effect of confinement. An analytical solution is therefore developed to calculate the lateral stresses during indentation of interfaces. A schematic of the contact problem of interface is illustrated in *Fig. 5-3*. The present boundary value problem shows non-linearity in the displacements of the bodies and contains mixed boundary conditions in the loaded area. It also changes its size in a non-linear manner while applying the load therefore several assumptions and simplifications are needed to describe the problem in a mathematically comprehensible way. The underlying simplifications of the model are discussed in the following text.

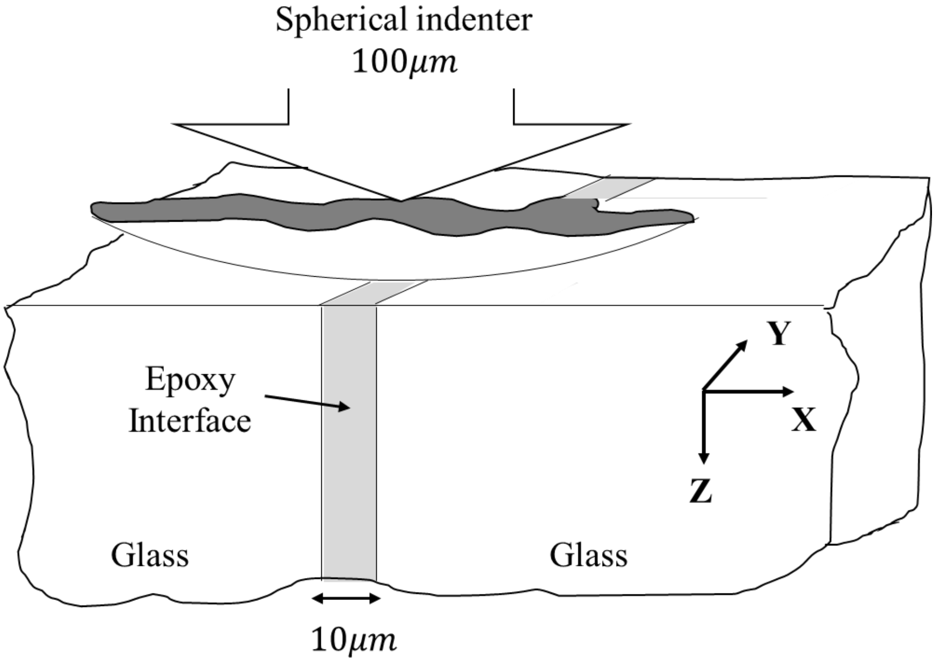

Fig. 5-3. Schematic of epoxy interface between glasses.

As shown in Fig. *5-3*, the spherical indenter has a radius of 100 μm and the epoxy interface has a thickness of 10 μm. In the present analysis, the indentations are quasistatic and fully elastic which gives small indentation depths, δ_2, compared to the indenter radius. This condition allows for the simplifications of the loaded region. The term “quasistatic” means that the indentations are performed with a low velocity and the dynamic forces such as inertia are not considered. This case of loading allows us to restrict the theoretical model to a static one which means that stresses are calculated for specified indentation depths and loads.

Whenever a spherical body is in contact with a half space, the surface tractions, because of geometrical reasons, are not one dimensional in the indentation direction. This causes normal and tangential displacements in the elastic half space. The contact between the indenter and the half space is assumed to be a frictionless contact, where the tangential forces in the loaded area are zero, a no slip contact, or a mix of both with partial slip. In the latter case, no slip occurs in the center of the contact area and slip starts to appear first at the margins but with increasing indentation depth, the slip zone increases. The curvature of the indenter within the contact area is small because of the small indentation depths and comparatively big indenter radius. This allows us to assume contact as a no slip contact.

Interfaces are often described as transversely isotropic with the interface normal axis as the symmetry axis [162, 163]. The conditions of compatibility and equilibrium are expressed as:

$$\delta\epsilon_{ij}^{||epoxy} = \delta\epsilon_{ij}^{||glass} , \tag{5.2}$$

$$\sigma_{ij}^{\perp epoxy} = \sigma_{ij}^{\perp glass} . \tag{5.3}$$

The compatibility condition means that the local strains, $\delta\epsilon_{ij}^{||epoxy}$, in the interface plane must correspond to the local strains occurring in the glass, $\delta\epsilon_{ij}^{||glass}$ close to the interface. The stresses perpendicular to the interface plane, $\sigma_{ij}^{\perp epoxy}$ in interface and $\sigma_{ij}^{\perp glass}$ in glass, must also be in equilibrium.

The geometry of the contact problem is such that the indenter is in contact with the thin interface and the bulk phase glass. Since the stiffness of the indenter is usually significantly higher than the stiffness of the sample, the normal surface displacement of the interface is prescribed by the geometry of the indenter. Considering different stiffness for the interface and the bulk phases, this boundary condition leads to a jump in the stresses. It has continuous strain distribution for the component in indentation direction while the stresses perpendicular to the interface must fulfill the condition of equilibrium.

To solve this problem, a fictitious homogeneous isotropic elastic half space is assumed which for a given applied load through the indenter exhibits the same normal surface displacement as the material with interface. The elastic modulus of this half space can be obtained by using Hertzian equations [164] given as

$$E^* = \frac{3P}{2\delta^{\frac{3}{2}}\sqrt{R_1}}. \tag{5.4}$$

Here, E^* is the effective Young's modulus for the contact and *P* is the applied load. δ is the maximum total deformation of the surface which is a sum of the indentation depth δ_2, the depth of the indenter deformation δ_1 and R_1 is the radius of the indenter. The effective modulus can be expressed in terms of the modulus and Poisson's ratios of the two bodies in contact which gives the Young's modulus of the half space as

$$E_2 = \frac{E^*\left(1-\nu_2^2\right)E_1}{2E_1 - E^*\left(1-\nu_1^2\right)}. \tag{5.5}$$

The Poisson's ratio of the interface is unknown and is assumed to be equal to one of the bulk phases. Here subscript '1' corresponds to the indenter properties and subscript '2' corresponds to bulk material properties. Generally, a ratio of $\nu = 0.25$ is valid for most of the engineering materials [165].

The stress distribution of this fictitious elastic half space can be obtained by using the constitutive equations for a distributed load acting on the surface of a half space given in equation(5.6)-(5.11) as,

$$\sigma_{xx,fict} = \int_{-a}^{a} \int_{-\sqrt{a^2-\zeta^2}}^{\sqrt{a^2-\zeta^2}} -\frac{3p(\zeta,\eta)(x-\zeta)^2 z}{2\pi R'^5} + \frac{(1-2\nu)\,p(\zeta,\eta)\,z}{2\pi R'^3}$$

$$-\frac{(1-2\nu)\,p(\zeta,\eta)}{2\pi}\left\{\frac{1}{R'(R'+z)} - \frac{(x-\zeta)^2}{R'^3(R'+z)} - \frac{(x-\zeta)^2}{R'^2(R'+z)^2}\right\} d\eta\, d\zeta,$$

(5.6)

$$\sigma_{yy,fict} = \int_{-a}^{a} \int_{-\sqrt{a^2-\zeta^2}}^{\sqrt{a^2-\zeta^2}} -\frac{3p(\zeta,\eta)(y-\eta)^2 z}{2\pi R'^5} + \frac{(1-2\nu)\,p(\zeta,\eta)\,z}{2\pi R'^3}$$

$$-\frac{(1-2\nu)\,p(\zeta,\eta)}{2\pi}\left\{\frac{1}{R'(R'+z)} - \frac{(y-\eta)^2}{R'^3(R'+z)} - \frac{(y-\eta)^2}{R'^2(R'+z)^2}\right\} d\eta\, d\zeta,$$

(5.7)

$$\sigma_{zz,fict} = -\int_{-a}^{a} \int_{-\sqrt{a^2-\zeta^2}}^{\sqrt{a^2-\zeta^2}} \frac{3p(\zeta,\eta)\,z^3}{2\pi R'^5}\, d\eta\, d\zeta, \tag{5.8}$$

$$\sigma_{xy,fict} = \int_{-a}^{a} \int_{-\sqrt{a^2-\zeta^2}}^{\sqrt{a^2-\zeta^2}} -\frac{3p(\zeta,\eta)(x-\zeta)(y-\eta)z}{2\pi R'^5} + \frac{(1-2\nu)p(\zeta,\eta)}{2\pi}\left\{\frac{(x-\zeta)(y-\eta)}{R'^3(R'+z)} + \frac{(x-\zeta)(y-\eta)}{R'^2(R'+z)^2}\right\} d\eta d\zeta, \tag{5.9}$$

$$\sigma_{xz,fict} = -\int_{-a}^{a} \int_{-\sqrt{a^2-\zeta^2}}^{\sqrt{a^2-\zeta^2}} \frac{3p(\zeta,\eta)(x-\zeta)z^2}{2\pi R'^5} d\eta d\zeta, \tag{5.10}$$

$$\sigma_{yz,fict} = -\int_{-a}^{a} \int_{-\sqrt{a^2-\zeta^2}}^{\sqrt{a^2-\zeta^2}} \frac{3p(\zeta,\eta)(y-\eta)z^2}{2\pi R'^5} d\eta d\zeta, \tag{5.11}$$

$$R' = \sqrt{(x-\zeta)^2 + (y-\eta)^2 + (z-0)^2}. \tag{5.12}$$

These equations are obtained from the Boussinesq solution for load acting on a half space using the principal of superposition. More details on the derivations can be found in the given reference[166]. Here, the load applied is represented as a function $p(\zeta,\eta)$ which is distributed over local x and y directions represented as ζ and η respectively. z is the indentation direction coordinate and a is the radius of contact. The load distribution, with applied load P, within the area of contact is given by Hertz [167] and can be expressed in Cartesian coordinates as,

$$p(\zeta,\eta)=\frac{3P}{2\pi a^2}\sqrt{1-\left(\frac{\zeta}{a}\right)^2-\left(\frac{\eta}{a}\right)^2}. \tag{5.13}$$

The correlation to the applied load is given by equation (5.14) as,

$$P=\int_{-a}^{a}\int_{-\sqrt{a^2-\zeta^2}}^{\sqrt{a^2-\zeta^2}} p(\zeta,\eta)\,d\eta\,d\zeta. \tag{5.14}$$

The classical stress solutions given in equation (5.6)-(5.11) are the basis of the following calculations. The key assumption of the approach presented here is that the classical solution and the solution for the layered half space are similar for the applied loads.

Due to its dependence on the geometry of the indenter, the strain in indentation direction, ϵ_{zz}, for a given indentation depth is assumed to be independent of the interface stiffness and thickness as long as the indenter is in contact with both the interface and the bulk phases. Therefore, it is assumed that the strain, $\epsilon_{zz,fict}$, is equal to the strain in the layered half space, $\epsilon_{zz,lay}$.

The strains perpendicular to the indentation directions and the interface are not prescribed by the indenter geometry and are therefore not necessarily a continuous function. The related stresses, in contrast, must fulfil equilibrium conditions and therefore be continuous. The assumptions for these components are therefore:

$$\begin{aligned}\sigma_{xx,fict} &\approx \sigma_{xx,lay}\,,\\ \sigma_{xz,fict} &\approx \sigma_{xz,lay}\,,\\ \sigma_{xy,fict} &\approx \sigma_{xy,lay}\,.\end{aligned} \tag{5.15}$$

The remaining strain components in interface plane direction ϵ_{yy}, and ϵ_{yz} must fulfill the conditions of compatibility and strain jumps cannot occur. Therefore, the assumptions are:

$$\begin{aligned} \epsilon_{yy,fict} &\approx \epsilon_{yy,lay}, \\ \epsilon_{yz,fict} &\approx \epsilon_{yz,lay}. \end{aligned} \tag{5.16}$$

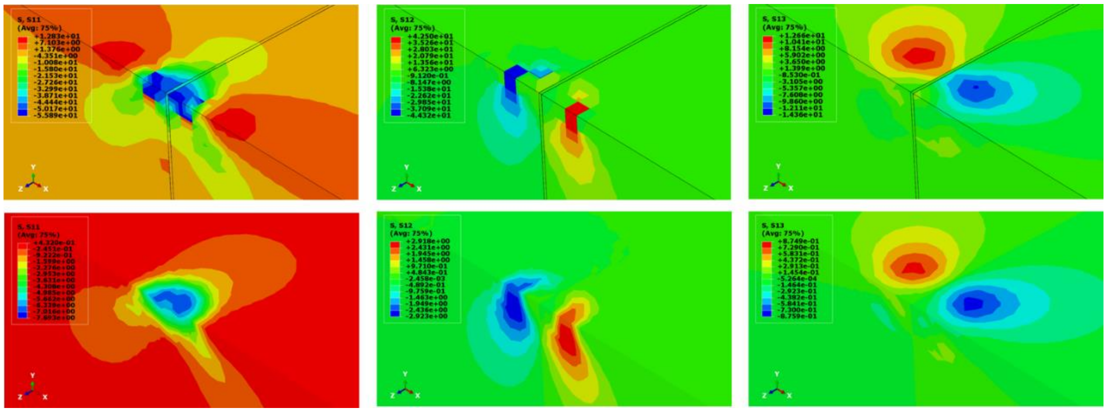

Fig. 5-4. ABAQUS figures showing the stress assumption validation for model with interface (top figures) with the model without interface (bottom figures)

To validate the assumptions of the model, an interface FE model and a homogeneous isotropic half space model was simulated with 10 µm thick interface in the middle. Plane strain loading boundary conditions were applied and the loading was given in the displacement boundary condition. The strains were measured at the maximum displacement of 500 nm that was equivalent to the indentation depth in the actual experiments. The strains and stresses were compared for both models. The stresses, Fig. 5-4, showed the similar profile validating the stress assumptions given in equation (5.15). The strain assumptions given in equation (5.16) were also verified by the ABAQUS solution as shown in Fig. 5-5.

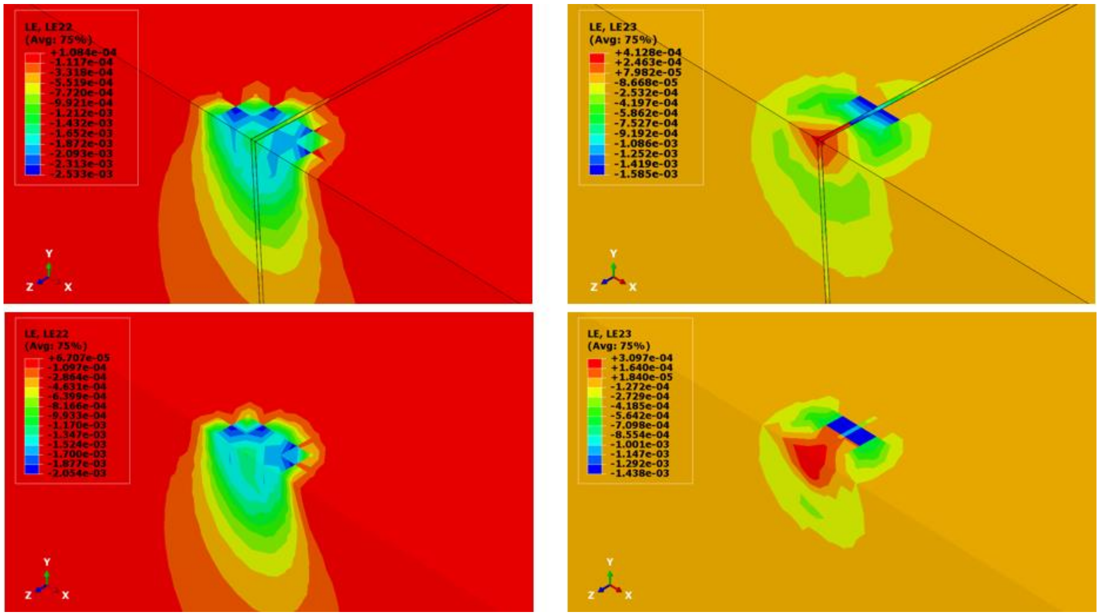

Fig. 5-5. ABAQUS figures showing the strain assumption validation for model with interface (top figures) with the model without interface (bottom figures)

While the perpendicular stresses can be obtained directly from equations (5.6),(5.9) and (5.10), the other stress components must be first transferred into strains using Hooke’s law and the elastic constants of the fictitious elastic half space. A brief description of the stresses in the plain-strain case is given below.

In contrast to the plane stress state, which is mostly used to describe the behavior of thin walled components such as the skins of aircraft, where the structure is not able to be loaded in the third direction, plane strain is used to describe very thick components, where (almost) no strains occur in the third direction. The state of plane strain leads to the following simplifications:

$$\epsilon_{yy} = 0, \tag{5.17}$$

$$\sigma_{yy} = \nu\left(\sigma_{xx} + \sigma_{zz}\right). \tag{5.18}$$

The relation between stresses and strains is generally known as Hooke’s Law, and can be expressed as it follows for the case of plane strain,

$$\epsilon_{xx} = \frac{1}{E}\left\{\left(1-\nu^2\right)\sigma_{xx} - \nu\left(1+\nu\right)\sigma_{zz}\right\}, \tag{5.19}$$

$$\epsilon_{zz} = \frac{1}{E}\left\{\left(1-\nu^2\right)\sigma_{zz} - \nu\left(1+\nu\right)\sigma_{xx}\right\}, \tag{5.20}$$

$$\epsilon_{xz} = \frac{2\left(1+\nu\right)}{E}\sigma_{xz}. \tag{5.21}$$

In a second step, they are transferred back into the stresses using the elastic constants of the interface and the bulk phases as shown in Fig. 5-6.

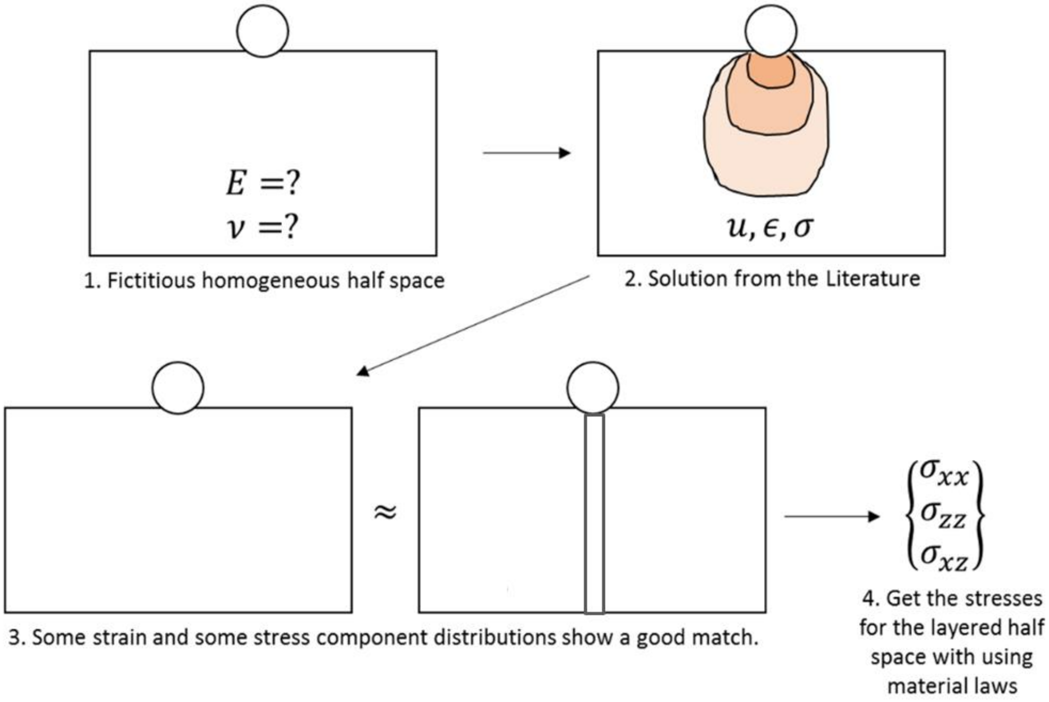

Fig. 5-6. Schematic sketch of the solution procedure.

The stress then can be obtained from the following equation:

$$\sigma_{zz} = \left[H\left(-\left(x + \frac{h}{2} \right) \right) + H\left(x - \frac{h}{2} \right) \right] \frac{E_{glass}}{\left(1+\nu_{glass}\right)\left(1-2\nu_{glass}\right)} \left\{ \nu_{glass}\epsilon_{xx} + \nu_{glass}\epsilon_{yy} + \left(1-\nu_{glass}\right)\epsilon_{zz} \right\}$$

$$+H\left(-\left(\sqrt{x^2} - \frac{h}{2} \right) \right) \frac{E_{epoxy}}{\left(1+\nu_{epoxy}\right)\left(1-2\nu_{epoxy}\right)} \left\{ \nu_{epoxy}\epsilon_{xx} + \nu_{epoxy}\epsilon_{yy} + \left(1-\nu_{epoxy}\right)\epsilon_{zz} \right\},$$

(5.22)

$$\sigma_{yy} = \left[H\left(-\left(x + \frac{h}{2} \right) \right) + H\left(x - \frac{h}{2} \right) \right] \frac{E_{A}}{\left(1+\nu_{glass}\right)\left(1-2\nu_{glass}\right)} \left\{ \nu_{glass}\epsilon_{xx} + \nu_{glass}\epsilon_{zz} + \left(1-\nu_{glass}\right)\epsilon_{yy} \right\}$$

$$+H\left(-\left(\sqrt{x^2} - \frac{h}{2} \right) \right) \frac{E_{epoxy}}{\left(1+\nu_{epoxy}\right)\left(1-2\nu_{epoxy}\right)} \left\{ \nu_{epoxy}\epsilon_{xx} + \nu_{epoxy}\epsilon_{zz} + \left(1-\nu_{epoxy}\right)\epsilon_{yy} \right\},$$

(5.23)

$$\sigma_{yz} = \left[H\left(-\left(x + \frac{h}{2} \right) \right) + H\left(x - \frac{h}{2} \right) \right] \frac{E_{glass}}{1+\nu_{glass}} \epsilon_{yz} + H\left(-\left(\sqrt{x^2} - \frac{h}{2} \right) \right) \frac{E_{epoxy}}{1+\nu_{epoxy}} \epsilon_{yz}.$$

(5.24)

Here, H is a Heaviside function on the interface. The value of H is zero outside the interface so that the equations from (5.22) to (5.24) only gives the stress on the interface. x is along the thickness of the interface with the middle point of interface as zero location. E and ν are the modulus and poisons ration with the subscript denoting the material. The strains ($\varepsilon_{xx}, \varepsilon_{yy}, \varepsilon_{zz}, \varepsilon_{xy}, \varepsilon_{xz}, \varepsilon_{yz}$) are the strains for the fictitious half space calculated by Hooke's law from equation (5.6) to (5.11). Due to limitations of the stress measuring technique, it is not possible to obtain a full stress tensor for the interface in the current indentation setup. Nevertheless, an equivalent stress can be obtained, therefore the calculated stress tensors are transferred to an equivalent stress by:

$$\sigma_v = \sqrt{\sigma_{xx}^2 + \sigma_{yy}^2 + \sigma_{zz}^2 - \left(\sigma_{xx}\sigma_{yy} + \sigma_{yy}\sigma_{zz} + \sigma_{xx}\sigma_{zz}\right) + 3\left(\sigma_{xy}^2 + \sigma_{yz}^2 + \sigma_{xz}^2\right)}. \tag{5.25}$$

Here, σ_v is the von Mises equivalent stress.

The flat punch corrections were then applied in the model. A flat ended and a spherical indenter produce different load distributions on the surface of the sample. While the normal stress $p(\zeta,\eta)$ which is transferred from a sphere to the sample is a quadratic function with its maximum at the center of the contact, the normal stress transferred from a flat indenter to the sample has its minimum at the center and the maximum at the edge. Therefore the stresses occurring close to the edge of the sample reach theoretically infinity. Expressed as equations, the two distributions are:

In the case of spherical indenter,

$$p(\zeta,\eta) = \frac{3P}{2\pi a^2}\left(1 - \left(\frac{\zeta}{a}\right)^2 - \left(\frac{\eta}{a}\right)^2\right)^{\left(\frac{1}{2}\right)}, \tag{5.26}$$

And in the case of flat-punch indenter

$$p(\zeta,\eta) = \frac{P}{2\pi a^2}\left(1 - \left(\frac{\zeta}{a}\right)^2 - \left(\frac{\eta}{a}\right)^2\right)^{-\left(\frac{1}{2}\right)}. \tag{5.27}$$

The relations between the load-displacement curve, the Young's modulus and the contact area radius as introduced earlier are not valid any more. Therefore the following relations are used:

$$p_0 = P/(2\pi a^2) \text{ , and} \tag{5.28}$$

$$E_2 = \frac{\pi\left(1-v^2\right)p_0 a}{\delta} \tag{5.29}$$

The resulting surface displacements can be expressed as: Inside the contact area:

$$u_z = \frac{\pi\left(1-v^2\right)p_0 a}{E_2} = \delta \text{ , and} \tag{5.30}$$

outside the contact area

$$u_z\left(r\right) = \frac{2\left(1-v^2\right)}{E_2} p_0 a \sin^{-1}\left(\frac{a}{r}\right) . \tag{5.31}$$

These formulations were further used for the flat punch indenter to find the stress distributions.

The abovementioned model was programmed in a MATLAB code to calculate the confined stresses for different scenarios. The confinement stresses were then calculated for the quasistatic case for the same applied load as in the experiments. Fig. 5-7 shows the representative stress distribution for material with interface and without interface. The model was run for the case with an interface and without an interface. The confinement stresses were then separated by comparing the stress values from the model with the experimental values according to equation (5.1) and used to find the value of constant ' k

’ given in equation (5.32). Since there was a passive confinement in the present case and we are comparing the stresses acting in the system instead of the compressive strengths, the k was calculated as a function of applied stress. The linear fit equation describing this relation between k and axial stress is given as

$$k = 1.592 * 10^{-9} * \sigma + 0.1112. \tag{5.32}$$

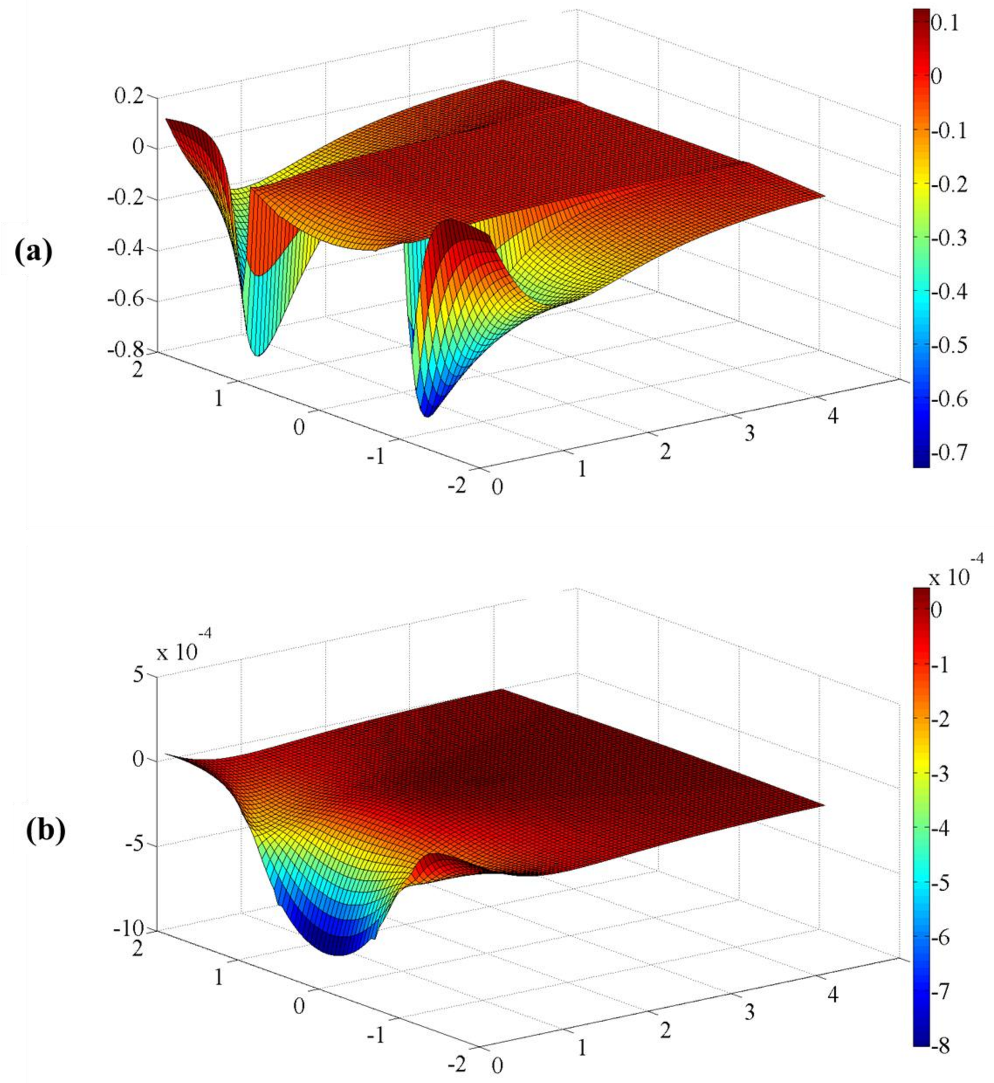

Fig. 5-7. Representative Stress distribution (a) with interface and (b) without interface.

The k for the dynamic case was then determined from the axial stress data available from the experiments. *Table 5-2* shows the values of k with stress for the quasistatic which was used to fit equation(5.32).

Table 5-2 k with respect to the applied stress for the quasistatic case.

Stress	0.06	0.08	0.1	0.14	0.16	0.18	0.2
k	3.52	-1.48	-4.61	2.80	1.27	0.74	0.51

5.3 Multiaxial Stresses in Interfaces

Raman spectroscopy is an excellent tool to measure properties such as the crystalline structure, chemical signature without a necessity of sample preparation. It is a not-contact and non-destructive mode of measurement which measures data from the surface of the sample. The molecular signal obtained from Raman is also associated with the stress state of the sample and thus provides a tool for non-contact evaluation of stress in the sample under considerations which also allows for rapid data acquisition within a matter of seconds. The Raman spectroscopy is based on ‘Raman Effect’, which provides a unique ‘fingerprint’ of every individual substance as a characteristic of for its identification. It is an inelastic process in which energy is exchanged between the incident photon and molecule. During the process, the molecule either emits a photon of lower frequency (stokes) or higher frequency (anti-stokes) than the incident photon. Stokes transitions are more likely to happen as the molecules are predominantly in the ground state at room temperature. There are some other experimental methods available to measure the stress distribution such as X-ray diffraction (XRD) and cross-sectional transmission electron microscopy (XTEM) but this methods are cumbersome due to extensive sample preparation and destructive in nature[129]. X-Ray diffraction (XRD) measures the chemical bond lengths of atoms and angle with high precision from which values for the strain tensor components can be obtained[168]. The focus of the x-ray beam can reach a precision of few µms. The resolution is still large compared to thickness the examined interface,10 µm, and it requires special instrumentation. The Raman spectroscopy has been used for other material systems such as epoxy during recent years to measure the curing state as well as the residual stresses in the sample [130]. The sample used to measure the Raman stresses on the interface is shown in Fig. 5-8

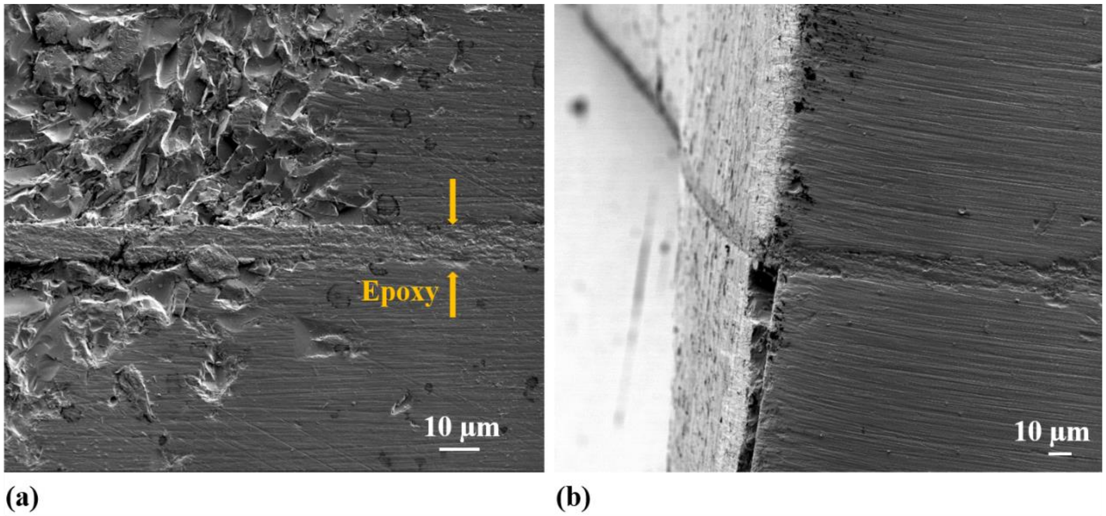

Fig. 5-8. SEM images showing epoxy interface (a) unpolished and polished and (b) edge of the sample with finite thickness interface.

We have used the nanomechanical Raman spectroscopy experiments to measure the stresses in the interface at different applied loads during indentation to compare the stress distribution. The epoxy samples shows Raman peaks in a wide range from 560 nm to 645 nm. The Raman signal at each wavelength depends on the masses of the atoms involved and the strength of the bonds between them. In the current system we measured the strongest signal around 641.1 nm as shown in *Fig. 5-9*. This signal corresponds to the C-H vibrations which corresponds to the polymer chains in the cured epoxy shown in red boxes in *Fig. 5-10*.

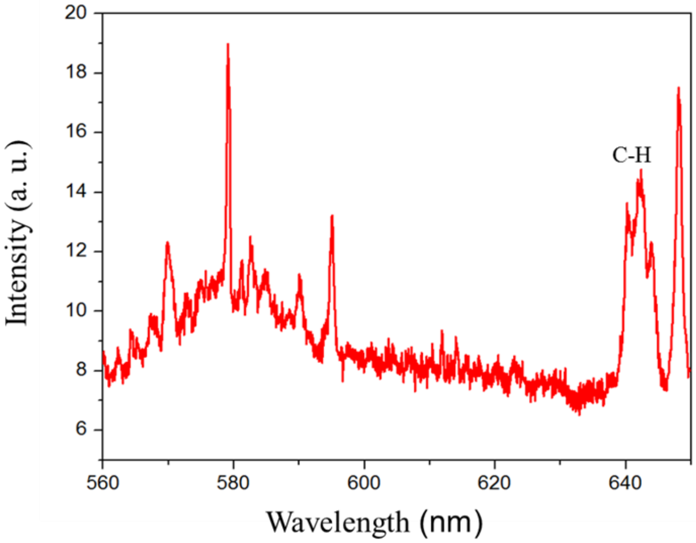

Fig. 5-9. Raman spectrum collected from epoxy showing the peak corresponding to C-H bond.

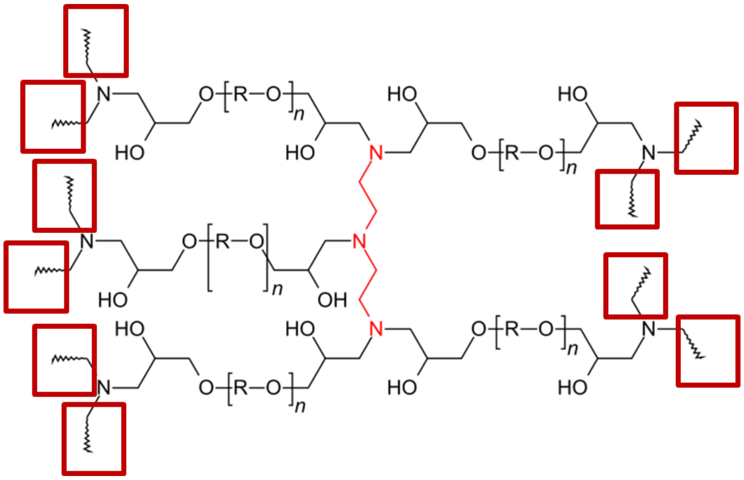

Fig. 5-10. Cured epoxy showing the polymer chains in red boxes with C-H bonds giving the Raman signal.

The first step to measure the stress across the interface is to establish a calibration curve of Raman shift with the applied stress. A uniaxial load was applied on a block of epoxy and the Raman shift was measured at applied loads of 100, 200, 300, 400 and 500 mN. The stresses were obtained by dividing the load by the area of the calibration sample. The measured Raman peak data was converted into shift by the equation

$$\Delta\omega = \left(\frac{1}{\lambda_{laser}} - \frac{1}{\lambda_{measured}} \right) * 10 \wedge 7 \ cm^{-1}. \tag{5.33}$$

The change in shift was obtained by subtracting the shift at the applied load for the shift at zero load. The calibration curve for shift versus load for epoxy is given in *Fig. 5-11*.

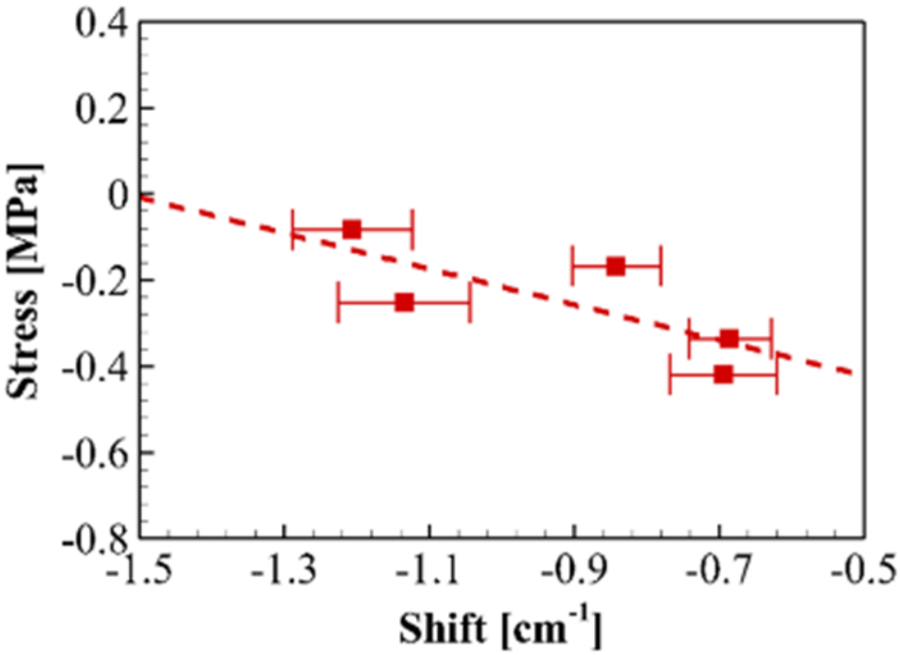

Fig. 5-11. Raman shift versus stress calibration curve for epoxy

The Raman shift versus stress calibration curve was used to calculate the stress maps on the interfaces. The load was applied on the interface and the Raman signal was measured on the transverse side of the sample. The Raman stress maps were measured at 3 loads, 20 mN, 200 mN, and 500 mN. The measurements were performed while holding the load constant.

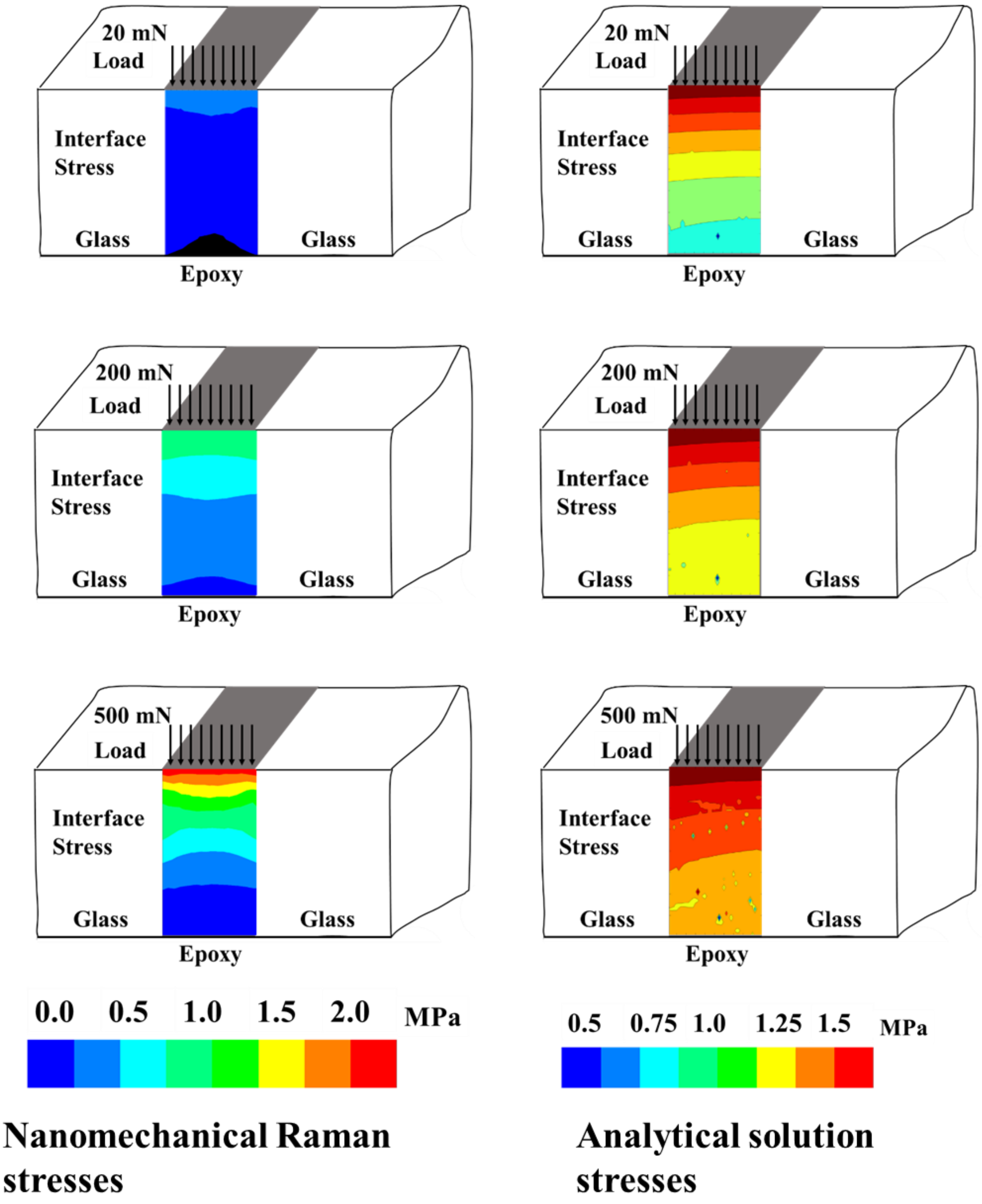

Fig. 5-12. Raman stress maps on interfaces with applied load by Nanomechanical Raman spectroscopy experiments and analytical solution

The stress distribution across interfaces are shown in *Fig. 5-12*. The stresses were measured across an area of 10X100 µm^2. The load direction is as shown in the picture. As shown in the picture, the stress is increasing with an increase in the applied compressive load. The confinement stresses are due to the presence of much stronger material adjacent to the epoxy interface.

CHAPTER 6. INTERFACE CONSTITUTIVE LAW

6.1 Analytical Model

There are several models that explains the effect of strain rate and confinement independently as already described in earlier sections but for material models described in the current paper, the effect of strain rate and confinement is coupled and needs to be treated simultaneously. Therefore, a new model has been developed that derives motivation from the Johnson-Cook model to couple the effect of confinement and strain rate. The proposed model takes the form given in equation as

$$\sigma = (A + B\varepsilon^n)(1 + C\ln\dot{\varepsilon}^*)(1 + k\sigma_1^*). \tag{6.1}$$

Here, σ is the equivalent stress, ε is the equivalent plastic strain, A is the yield stress, B is the strain hardening constant, n is the strain hardening coefficient, C is the strain rate strengthening coefficient and k is the confinement factor. $\dot{\varepsilon}^* = \frac{\dot{\varepsilon}}{\dot{\varepsilon}_{ref}}$ is the dimensionless strain rate normalized with reference strain rate, $\sigma_1^* = \frac{\sigma_1}{\sigma_{compressive\,strength}}$ is the dimensionless lateral stress normalized with the compressive strength of the material. The reference strain rate, $\dot{\varepsilon}_{ref}$, is taken as 1 s^{-1} and the compressive strength , $\sigma_{compressive\,strength}$, is taken as 100 MPa. In the current experiments, the temperature was constant so the temperature effects were neglected.

The coefficient A is the yield stress of the material and is a known material property. Considering the experiments in which the strain rate was equal to the reference strain rate and there were no confinement effects, the equation(6.1) reduces to

$$\sigma = (A + B\varepsilon^{n}). \tag{6.2}$$

The influence of the strain rate and confinement was ignored and the equation was rearranged by taking logarithm on both sides given as

$$\ln(\sigma - A) = \ln B + n \ln \varepsilon. \tag{6.3}$$

The linear fit of stress and strain values after the transformation given in equation (6.3) gives $\ln B$ and n from the intercept and slope data as shown in Fig. *6-1*

The values in the given case are $A = 11MPa$, $B = 208MPa$ and $n = 0.46$.

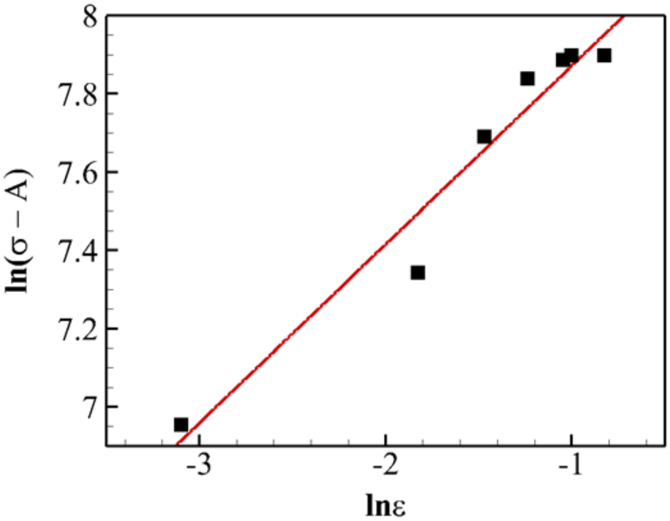

Fig. 6-1. Linear fit to determine A, B and n for equation.

The value of constant k was taken as 1.6 and the value of C was then determined by fitting the data for the confined case in dynamic and quasistatic loading. The values of coefficients for the given case are provided in Table *6-1*

Table 6-1 Parameters for the given model coupling strain rate and confinement effects

A (MPa)	B (MPa)	C	n	k
11	208	0.05	0.46	1.6

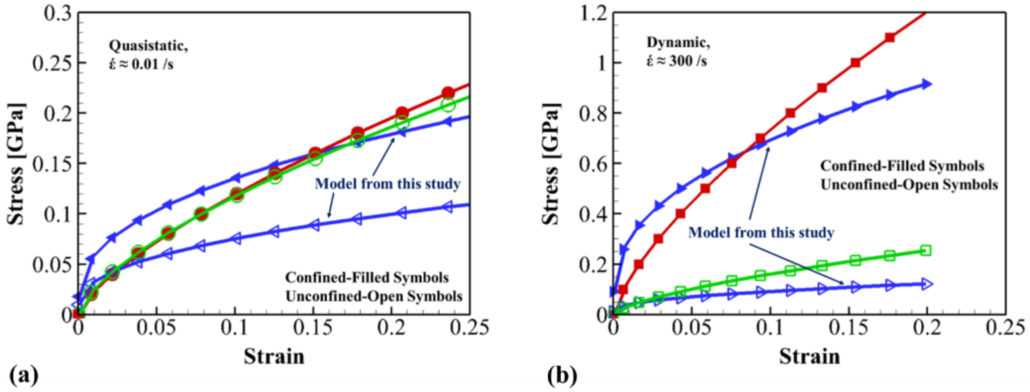

Fig. 6-2. Comparison of current model with the Tsai-Sun model for (a) quasistatic loading and (b) dynamic loading.

The model developed in the current study was compared with the earlier models. As shown in the Fig. *6-2*(a) and (b), the current model captures the confinement effect at both quasistatic and dynamic case while the former Tsai-Sun model is only for the strain rate effect and thus does not account for the confinement effect. At lower strain rates, the difference in stresses was mostly because of the confinement effect while in the dynamic case, the strain rate effect also plays a major role. The difference in the stresses was higher in the dynamic case as evident in the Fig. *6-2* (b) compared to Fig. *6-2* (a). Thus the current models is better suited to model the behavior of materials under confined spaces such as interfaces in the composite materials, metals, ceramics etc. A conventional way is to consider interface as a zero thickness and to not consider interface effect on the material deformation. The model in equation(6.1) takes the effect of interfaces into the deformation and should be considered for cases with interface dominant geometries such as biomimetic and other layered materials.

The constitutive model for the confinement and strain rate effect was also verified for size effect by conducting experiment on the interface with indenters of 1, 10 and 100 µm radius on the same interface. The stress strain curves and the fit to the experimental data from the new constitutive model is shown in *Fig. 6-3*. The fitting parameters are listed in Table *6-2*. The equation (6.1) fits very well to the data obtained from the experiments with indenters with different radiuses. The thickness of the interfaces was 10 µm in these experiments. As seen in the *Fig. 6-3* (a), the interface responds more like epoxy material with lower yield stress and lower stress values. *Fig. 6-3* (b) shows the impact with a 10 µm indenter where the indenter impacts the whole interface thickness and this shows higher values in the stress-strain curve. The stress strain data for impacts with 100 µm indenter is shown in *Fig. 6-3* (c) with very high stress values that reached the elastic limit of glass. This is also the reason for higher values of fitting parameters for 100 µm radius indenter in Table *6-2*. Reader might think of these values as unreasonable at first look but in this case, the indenter was much bigger than the interface with the effective impacts on the glass phase with a very low contribution from the epoxy interface. This is further highlighted in *Fig. 6-3* (d) where the stress strain curve is plotted for the lower strain-rate regimes which exhibits the behavior resembling to the brittle failure in materials such as glass. Thus the current model developed in this paper applies very well to the impact regimes where the interface thickness is comparable to the impactor. The model is not applicable to the cases where interface does not dominate the deformation mechanisms exhibited in Fig. *6-3*(c). This essentially means that the confinement effect is not a dominant factor in the deformations in that particular case of larger indenter radius.

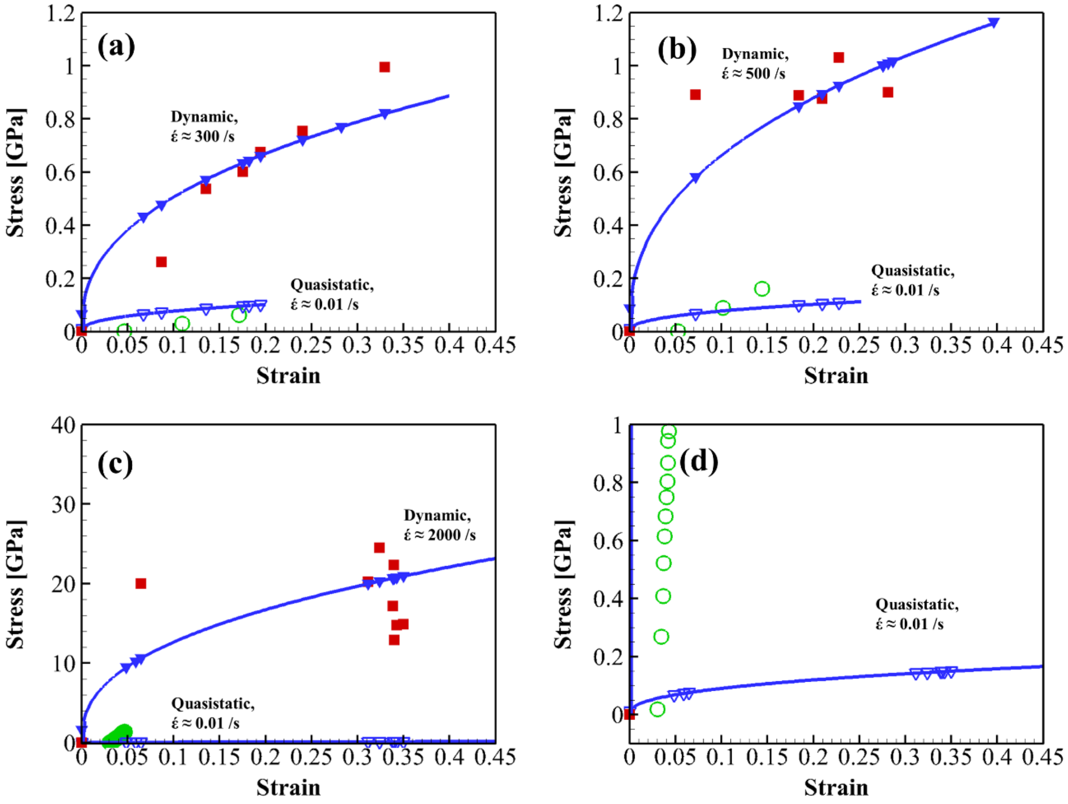

Fig. 6-3. Fit of the constitutive model developed in current article to the stress strain curves from impact experiments with spherical indenter of radius (a) 1 µm, (b) 10 µm, (c) 100 µm, and (d) showing the magnified quasistatic data in the case of 100 µm radius indenter.

Further experiments were performed on interfaces of different sizes of 10, 20 and 30 micron thickness to analyze the size effects. It was found that the yield stress of the interfaces increases with the decrease in the thickness. The stress-strain data is as shown in Fig. 6-4. The corresponding fit parameters are given in Table 6-3.

Table 6-2 Parameters for the given model coupling strain rate and confinement effects with size effect

Indenter Size (μm)	A (MPa)	B (MPa)	C	n	k	Strain Rate (s^{-1})	Confinement Stress (MPa)
1	11	208	0.05	0.46	1.59	300	250
10	11	208	0.05	0.46	1.59	500	350
100	11	208	0.05	0.46	1.59	2000	400
1	11	208	0.05	0.46	1.59	0.01	10
10	11	208	0.05	0.46	1.59	0.01	10
100	110	208	0.05	0.46	1.59	0.01	10

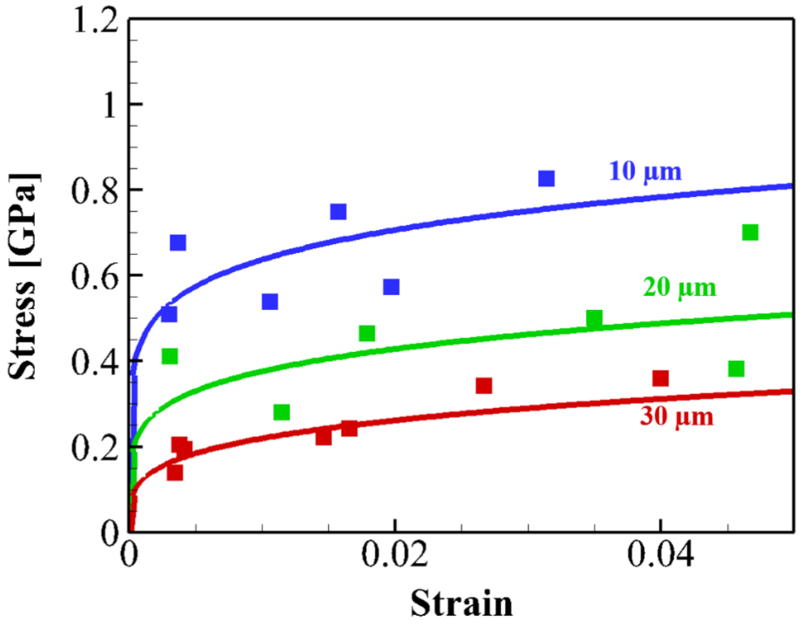

Fig. 6-4. Fit of the constitutive to the stress-strain for interface thickness of 10 μm, 20 μm, and 30 μm.

Table 6-3 Parameters for the given model coupling strain rate and confinement effects with size effect for different thickness interfaces.

Interface thickness (μm)	A (MPa)	B (MPa)	C	n	k	Strain rate (s^{-1})	Confinement stress (MPa)
10	51	208	0.05	0.46	1.59	175	400
20	41	208	0.05	0.46	1.59	145	250
30	21	208	0.05	0.46	1.59	125	200

CHAPTER 7. MULTILAYER MATERIALS APPLICATION

The interface constitutive law developed in the previous section was further implemented in the finite element software ABAQUS-explicit to check for the validity of the model. The model verification was done in three steps. In the first step, the behavior of the glass phase was verified by comparing the experiment and simulations for a single glass plate. The second step was to verify the 5 layer structure made of glass/epoxy/glass/epoxy/glass. The load-displacement of the multilayered assembly from the ABAQUS simulation was compared with the experimental results of a flat punch loading in the experiments. In the final step, a multilayered model with the thickness of the layers similar to that of the shrimp exoskeleton was modeled. The interfaces were made of chitin and their contribution during the deformation of the multilayered system was quantified. The interface constitutive model was used for the interfaces to predict the effect of interface in shrimp exoskeleton.

7.1 Glass Plate

The glass plate was modeled in the ABAQUS software and the load-displacement profile from the simulations was compared to the load-displacement profile from the experiments. The glass plate with dimensions of 22 mm length and 22 mm with a thickness of 100 micron was modeled for the finite element simulations. The dimensions were based on the experimental glass plate procured from Ted Pella Inc. (Redding, CA). The properties of the glass such as elastic modulus, poisons ratio and density were provided by the manufacturer for the simulations purposes. The failure properties were obtained from the literature[169]. The properties of glass used in the simulation as provided by the manufacturer are given in Table 7-1.

Table 7-1 Properties of glass plate.

E	70 GPa
ν	0.20
Density	2.51 g/cm3
Brittle Fracture Energy	100 J/m2
Failure Stress	80 MPa

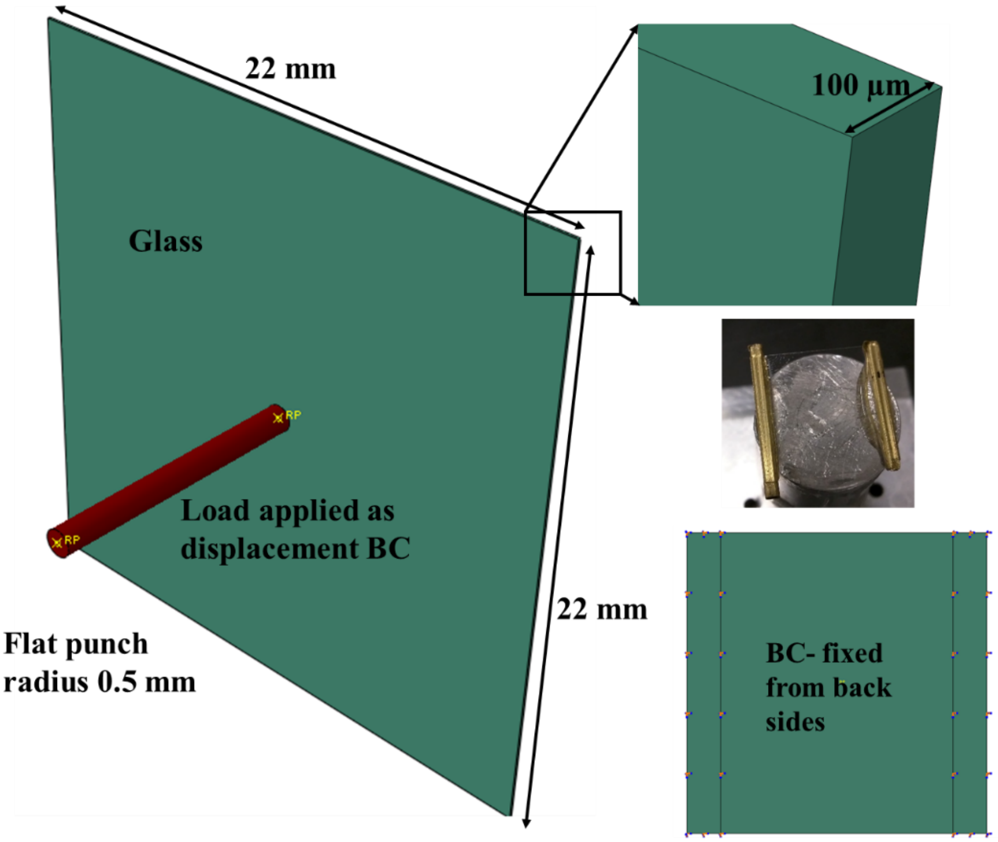

Fig. 7-1. ABAQUS model of the glass plate

The model was fixed at the bottom as per the experimental conditions. The sample mounting for the experiments is shown in Fig. 7-1. The loading head was allowed to move only perpendicular to the glass plate simulating the experimental conditions of the movement of the flat punch during loading. The load was applied as a displacement boundary condition equivalent to the displacement applied during experiments. The model dimensions are also described in Fig. 7-1. It shows the dimensions of the model, the thickness of the plates, the actual sample used in the experiments and the boundary condition applied to the backside of the plate and the loading direction.

The model was run for different number of elements to find the convergence. The model converged around 50,000 elements as shown in Fig. 7-2. The value of von-Mises stress was used as a parameter to find the convergence. The mesh for different cases is shown in Fig. 7-3. These values are also provided in Table 7-2. The minimum size of the element used for the simulation was 10 microns in the thickness direction of the plate. The final simulation used in the presented results was run for 48,400 elements.

Table 7-2 von-Mises stresses with number of elements

Total Elements	S Mises
1936	1.74
15987	17.03
48400	20.48
121000	20.03

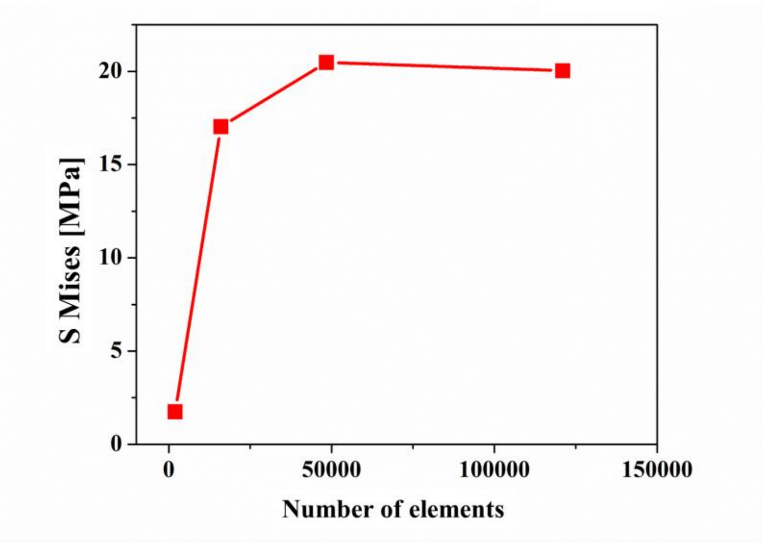

Fig. 7-2. Model convergence with number of elements.

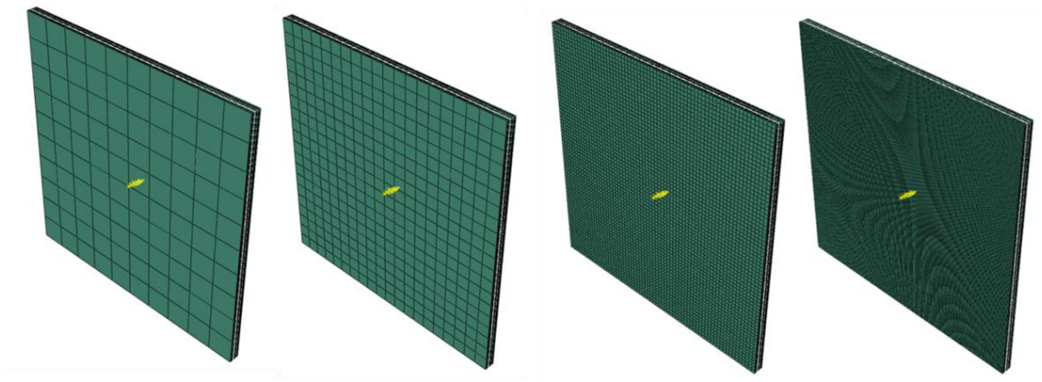

Fig. 7-3. Mesh size for the convergence study

The experiments were performed using a flat punch on the micro head of the indentation set up from Micro materials (UK). A detailed description of the setup is given earlier in the method section. The load is applied via an electromagnetic actuation and the displacements are measured using capacitor plates. The experimental setup was calibrated before the experiments by performing load, depth and machine compliance calibrations. The sample was loaded on the stage with movements in x,y and z directions. The load was applied and the displacement was monitored throughout the experiments. The load-displacement curve from the ABAQUS simulation was obtained by observing a reference point attached to the flat punch in the simulation. The load displacement curve from the experiments was compared to the load-displacement curves from the simulation as shown in Fig. 7-4. The data matched pretty well showing the validity of the ABAQUS model of glass plate. The displacement and stress distribution at the end of the simulation are also plotted in Fig. 7-5 and Fig. 7-6 respectively to give the reader an illustration of the stress distributions.

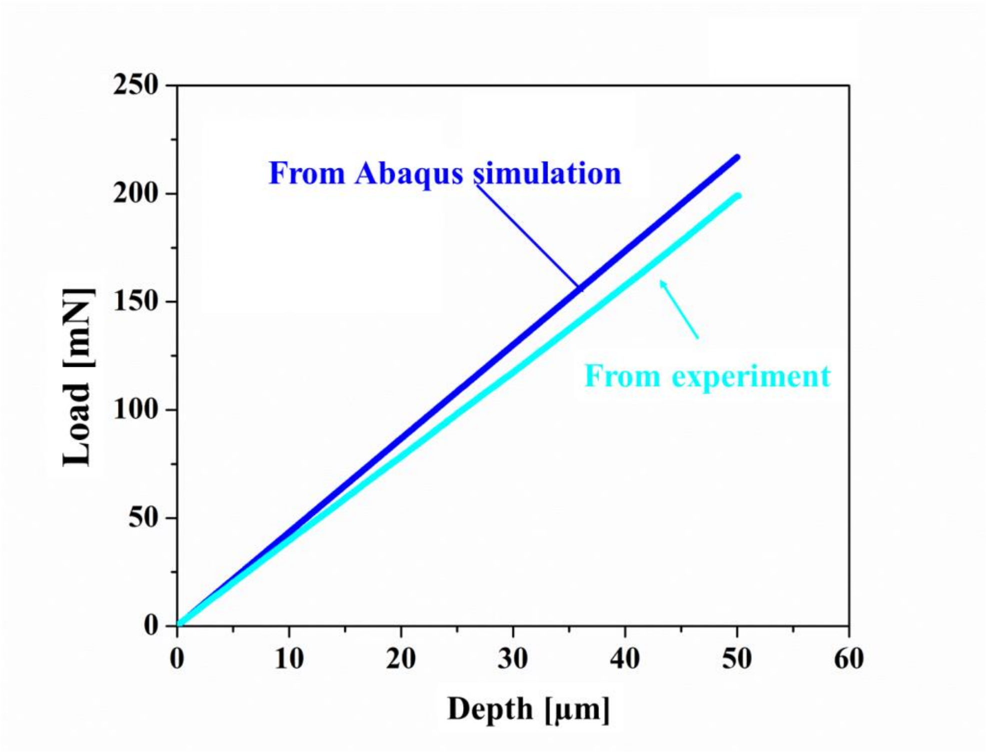

Fig. 7-4. Load-displacement curve for the glass plate from ABAQUS simulation and experiments.

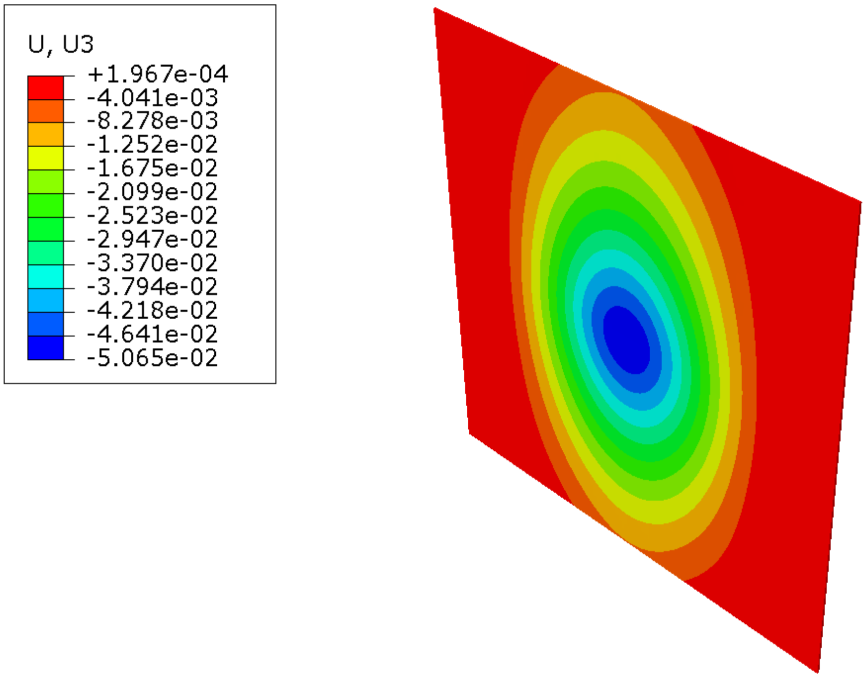

Fig. 7-5. Displacement at the end of the simulation

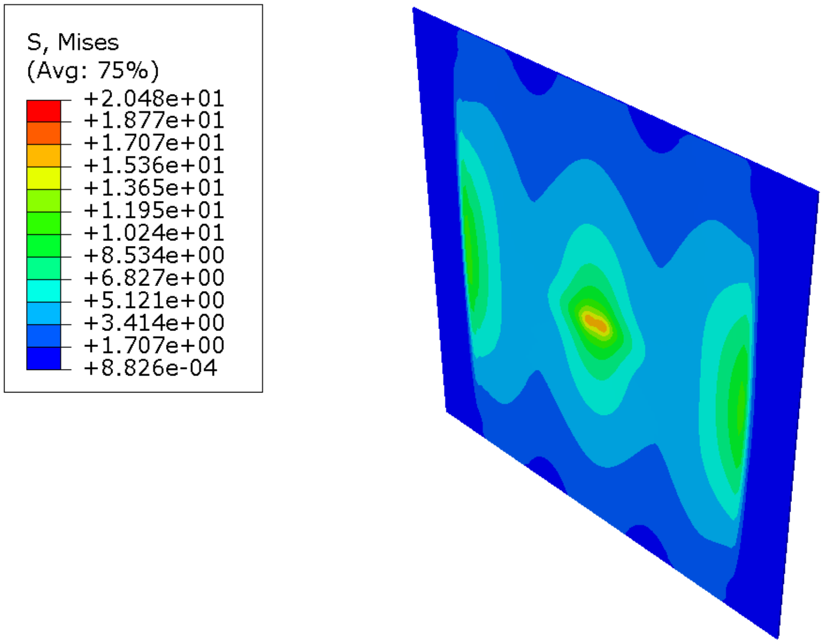

Fig. 7-6. Stress distribution at the end of the simulation

7.2 Multilayered Glass and Epoxy Interface System

The single glass plate model was verified in the earlier section. The second step was to verify the model of multilayered materials with epoxy interfaces between the glass plates. The samples were prepared using uncured epoxy layers of 50 microns and placing them between the glass plates. The multilayered glass and epoxy material was then cured at 150 degree Celsius for 30 minutes as per the guidelines from the manufacturer of the epoxy layers. The epoxy layers were obtained from the company Bonding Source (Manchester, NH). The final sample was checked for defects and proper adhesion of the epoxy in between the glass plates. The sample was mounted on the micro head of the micro materials indentation setup. The loading was applied using a flat punch. The experimental steps included moving the flat punch in the sample direction to bring it in contact with the sample. The micro head was calibrated for load, depth and machine compliance measurements.

Once all calibrations were done, the load was applied on the surface of the multilayered sample. This sample was then also modeled in the ABAQUS software with the same dimensions and loading conditions as in the experiments. The properties of the interfacial epoxy was based on the confinement effect developed in this research and also without the confinement effect. The 5 layer model was modeled as glass/epoxy/glass/epoxy/glass layers stacked one above the other. The dimensions of the model are given in Fig. 7-7. The properties of epoxy were as given in Table 7-3.

Table 7-3 Properties of Epoxy interface.

E	3.5 GPa
ν	0.20
Density	1.3 g/cm3
Confined Yield Stress	8 MPa

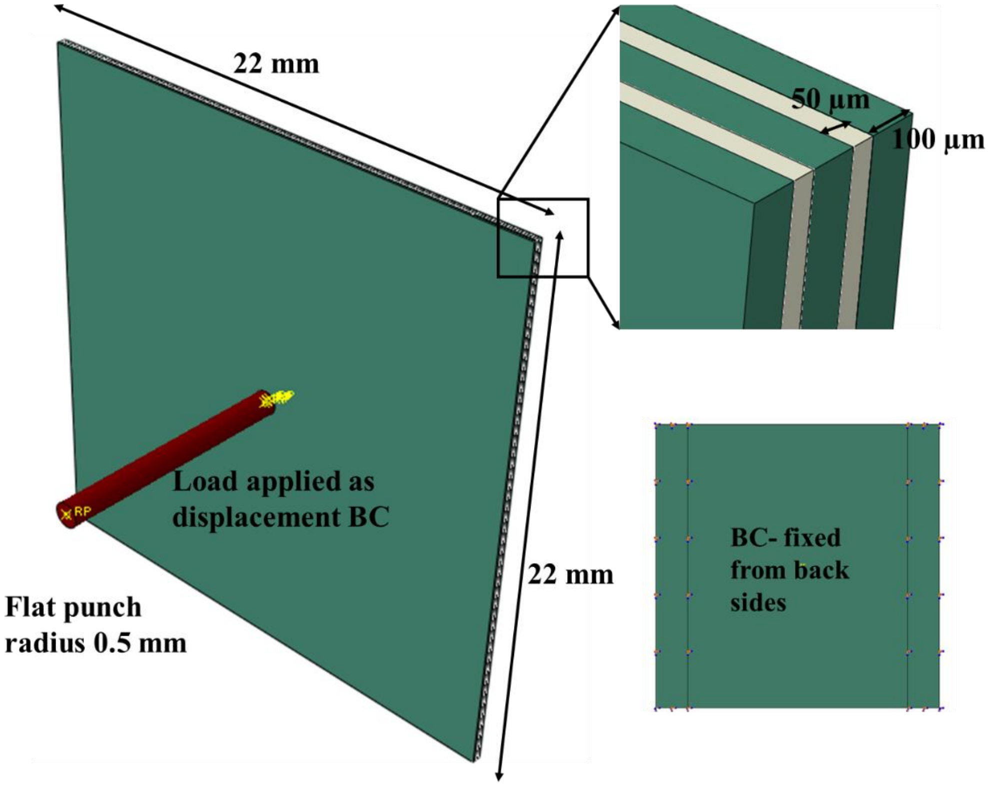

Fig. 7-7. ABAQUS model of the multilayered glass and epoxy plate

The model was run for different number of elements to find the convergence. The model converged around 60,000 elements as shown in Fig. 7-8. The value of von-Mises stress was used as a parameter to find the convergence. The mesh for different cases is shown in Fig. 7-9. The last figure also shows the elements in the thickness direction of the glass and epoxy interfaces. These values are also provided in Table 7-4. The minimum size of the element used for the simulation was 10 microns in the glass plate and 5 micron in the epoxy interface in the thickness direction. The final simulation used in the presented results was run for 60,500 elements.

Table 7-4 von-Mises stresses with number of elements

Total Elements	S Mises
54	34.01
180	43.95
2420	51.39
9680	62.07
60500	63.66
242000	63.8

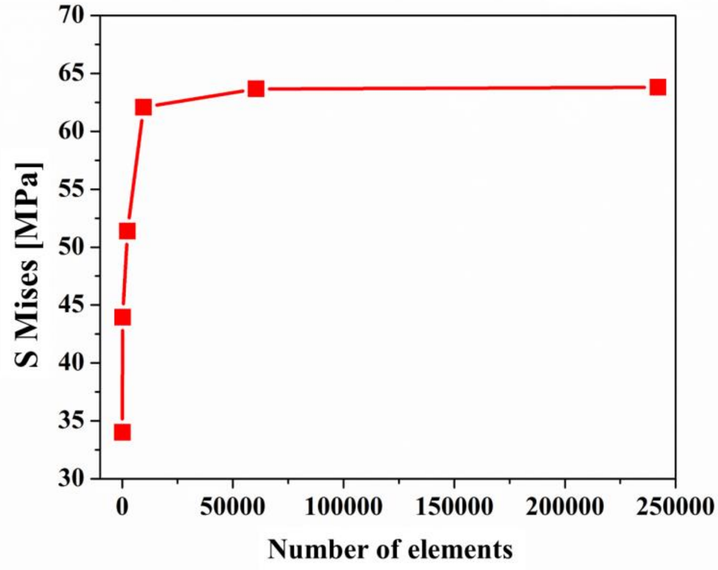

Fig. 7-8. Model convergence with number of elements.

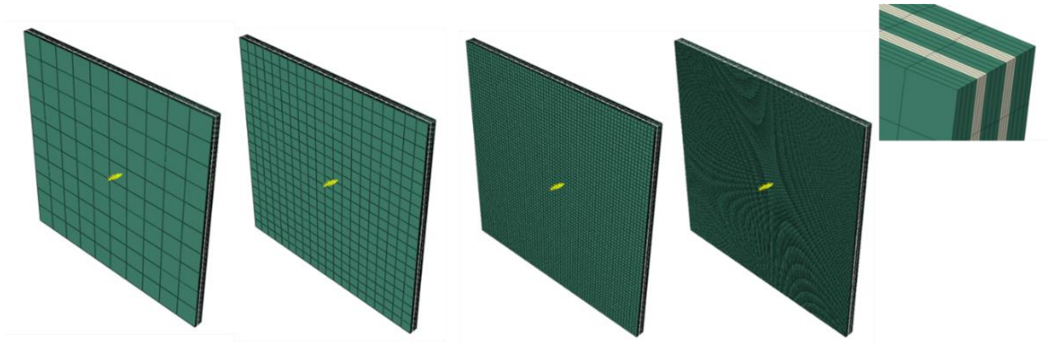

Fig. 7-9. Mesh size for the convergence study

The load was applied and the displacement was monitored throughout the experiments and stored through a data acquisition system. The load-displacement curve from the ABAQUS simulation was obtained by observing a reference point attached to the flat punch in the simulation. The load displacement curve from the experiments was then compared to the load-displacement curves from the simulation as shown in Fig. 7-10 for both the confined and unconfined case. The data matched pretty well showing the validity of the ABAQUS model of glass plate for confined case. The stress distribution at the end of the simulation are plotted in Fig. 7-11.

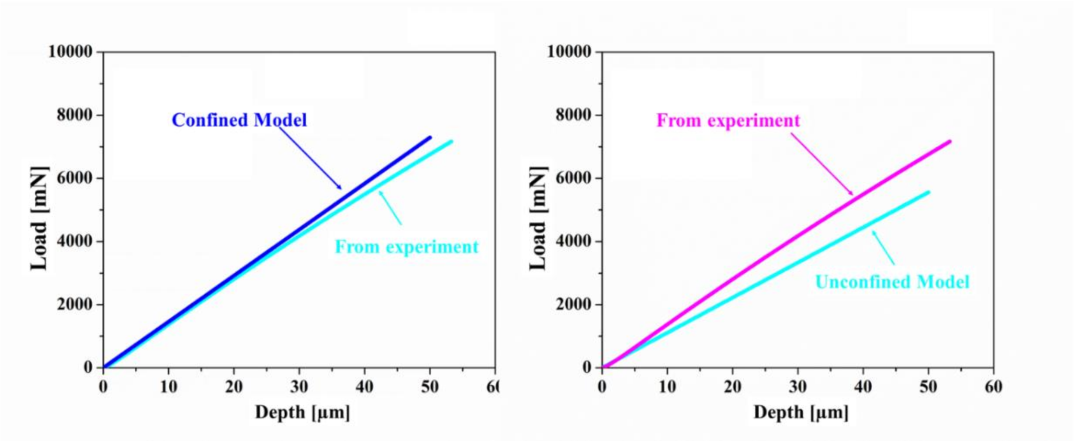

Fig. 7-10. Load-displacement curve for the glass plate from ABAQUS simulation and experiments for (a) confined model and (b) unconfined model

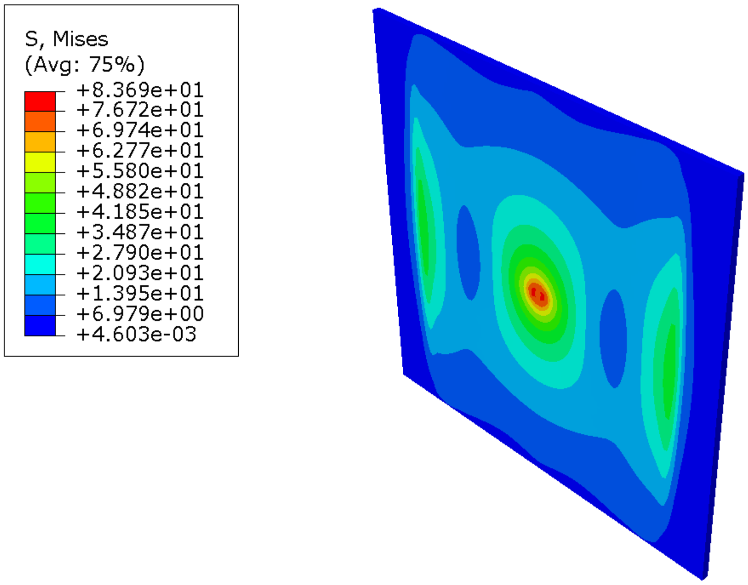

Fig. 7-11. Stress distribution at the end of the simulation

7.3 Multilayered Shrimp Exoskeleton Structure

The last step of the verification was to quantify the effect of interfaces in the shrimp exoskeleton. The shrimp exoskeleton was modeled with main phase layers having the properties obtained from the indentation experiments as provided in author's earlier papers[1-3, 10, 11]. The interfaces in shrimp exoskeleton are made up of chitin fibrils so the interface properties were given based on the chitin properties. The stress-strain relations for the chitin interfaces were obtained in our earlier work with the effect of orientation as well as the effect of environment [84, 85]. The model parameters for the interface constitutive law were obtained from this stress-strain data. The exoskeleton was then modeled with the main layer thickness of two microns and the interface thickness of one micron. These dimensions were based on the dimensions of shrimp like structures with the thickness of the layers equivalent to the shrimp exoskeleton. The properties of the layers and the dimensions of the model are given in Fig. 7-12. The material properties were derived by fitting the stress-strain curves from the earlier molecular dynamic studies performed in reference by Tao et al. [84, 85]. The properties of the main phase are given in Table 7-5 and the properties of interface are given in Table 7-6.

Table 7-5 Properties of shrimp exoskeleton main phase.

E	29 GPa
ν	0.20
Density	1.5 g/cm3
Layer thickness	2 microns
Interface thickness	1 micron

Table 7-6 Properties of chitin interface.

E	110 GPa
ν	.23
Density	1.5 g/cm3
A	150 Mpa
B	600 Mpa
n	0.4

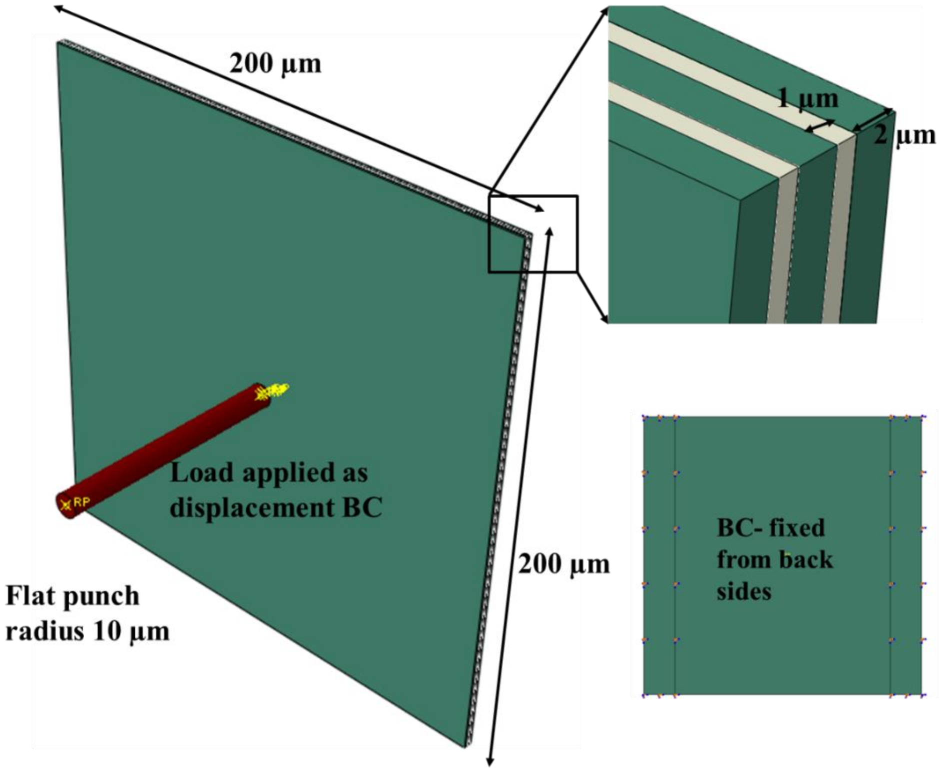

Fig. 7-12. ABAQUS model of the multilayered shrimp exoskeleton structure

Since the model was based on the similar structure as in the earlier section, the mesh was based on it and each layer was divided in 4 elements in the direction of thickness. The minimum element size was in the thickness direction of the layers with 500 nanometers in the main phase and 250 nanometers in the chitin interface. The model was run for two cases with the confined properties and without the confinement effect. The applied displacement boundary condition in each case is given in Fig. 7-13. The stress distribution in the each layer was then compared for both case layer by layer. The stresses in each layer was plotted for comparison as given in Fig. 7-14 to Fig. 7-16. The stress distribution in the interface layers was as given in Fig. 7-17and Fig. 7-18. The difference in these interface was quantified based on the strain energy of these interfaces as plotted in Fig. 7-19. This shows that the interfaces in the confined case have the ability to absorb more energy thus making the overall structure more stiff and resistant to deformations.

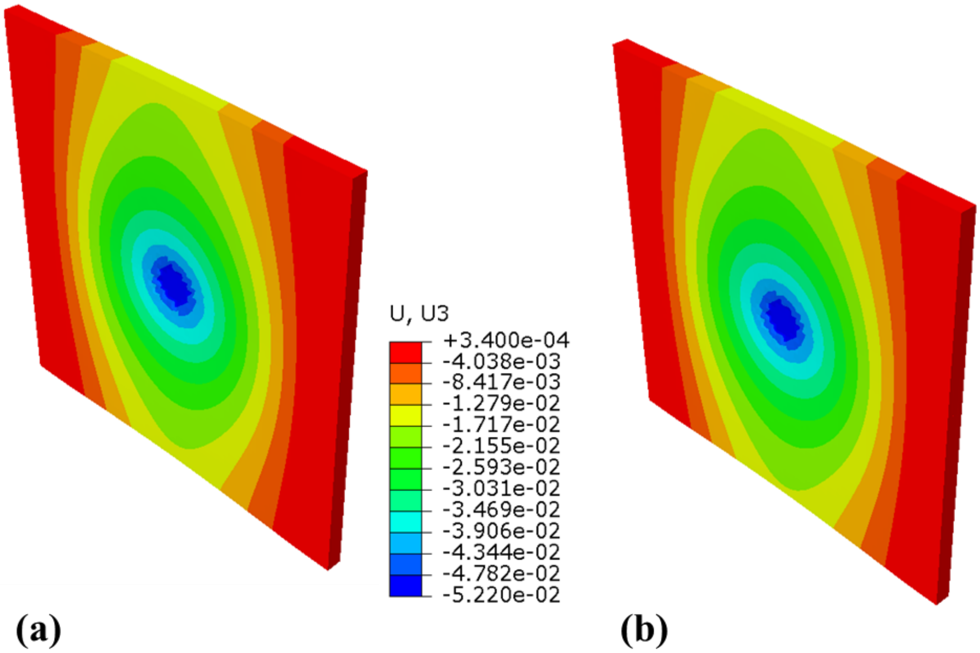

Fig. 7-13. Applied displacements to the system in (a) confined state and, (b) unconfined state

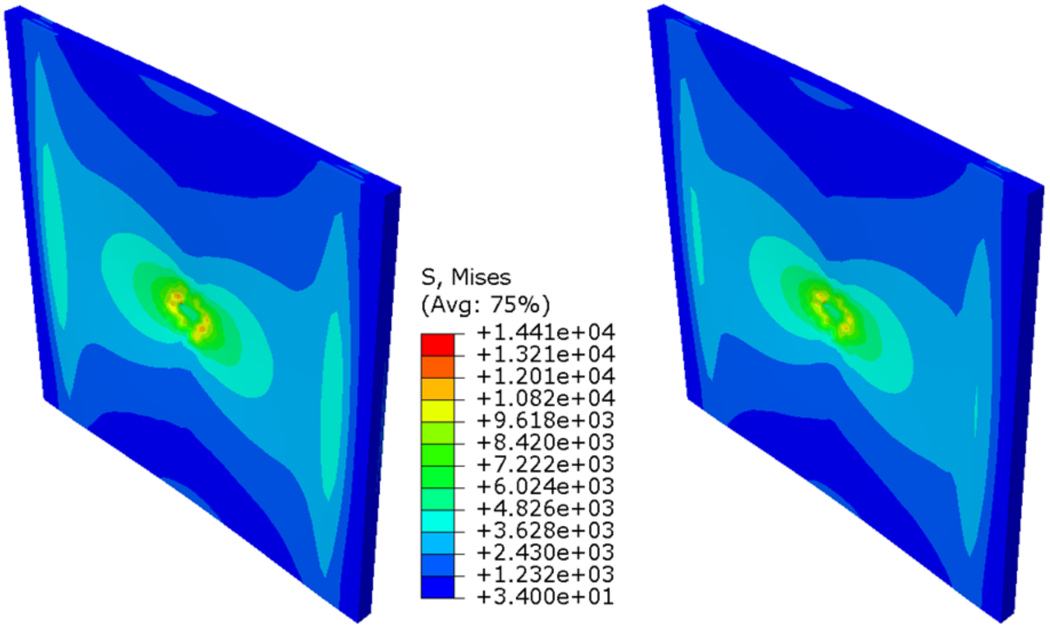

(a) **(b)**

Fig. 7-14. Stresses in the layer-1 with (a) confined state and, (b) unconfined state

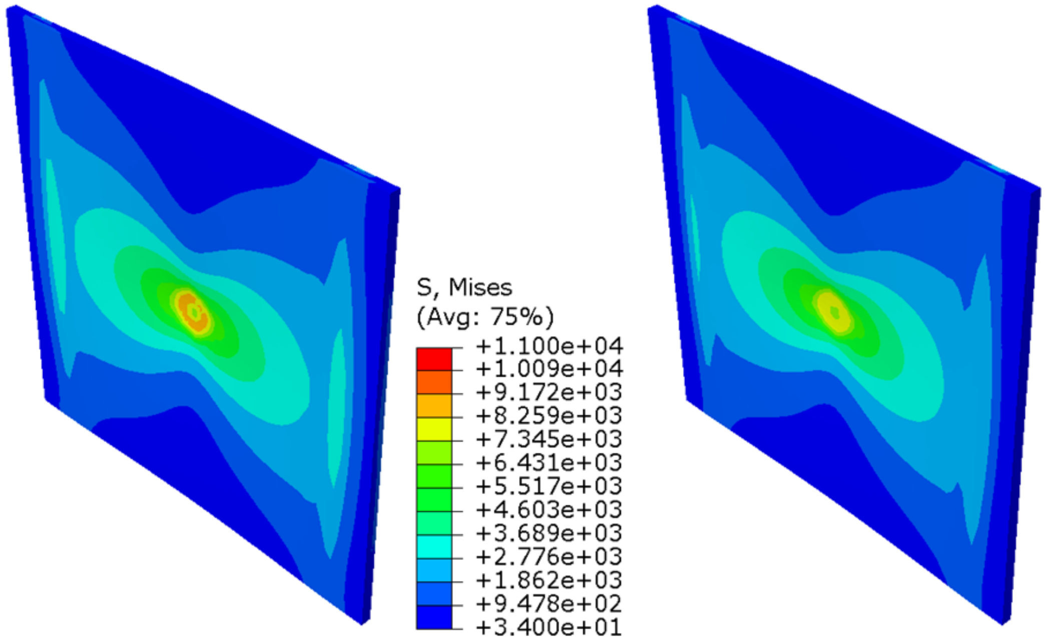

(a) **(b)**

Fig. 7-15. Stresses in the layer-2 with (a) confined state and, (b) unconfined state

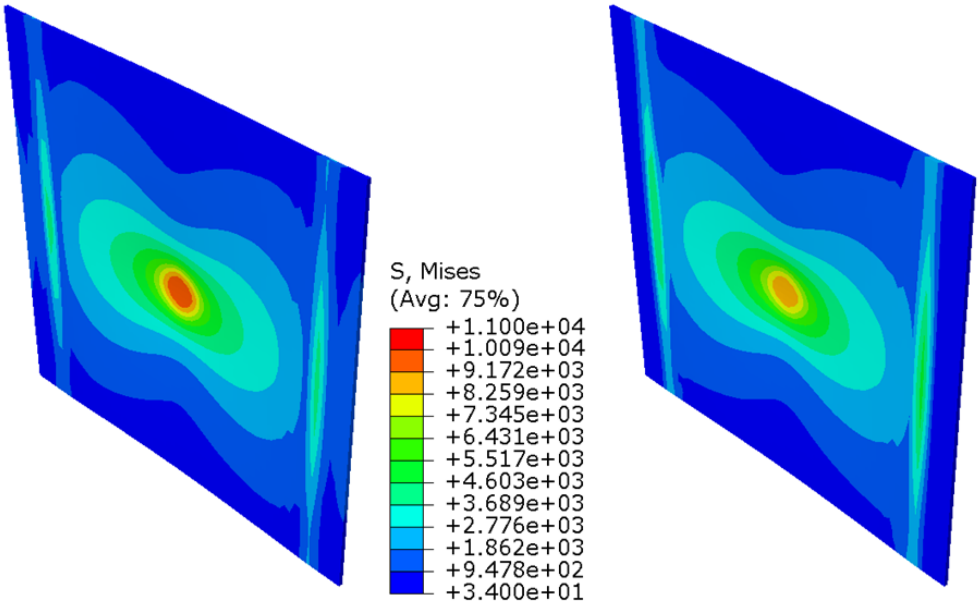

(a) **(b)**

Fig. 7-16. Stresses in the layer-3 with (a) confined state and, (b) unconfined state

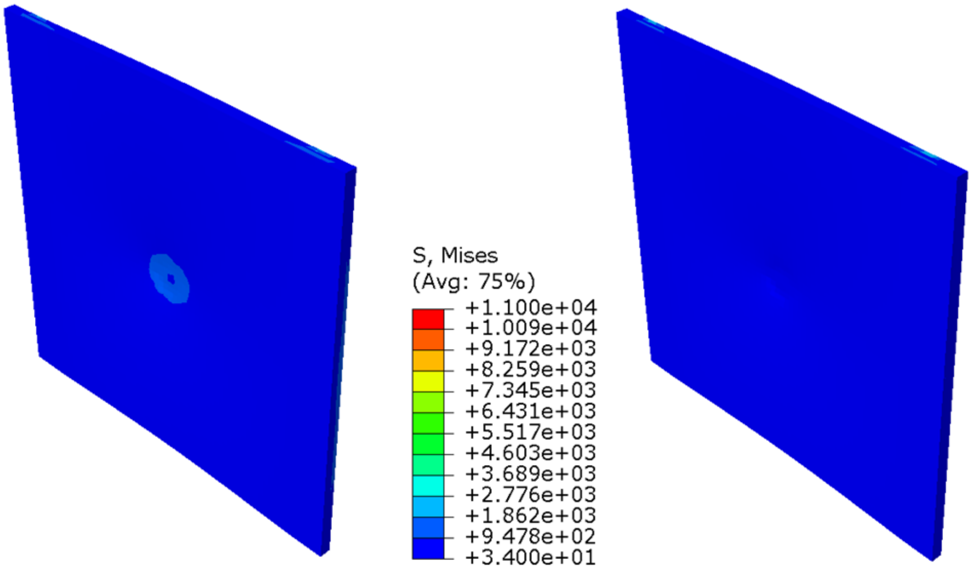

(a) **(b)**

Fig. 7-17. Stresses in the interface-1 with (a) confined state and, (b) unconfined state

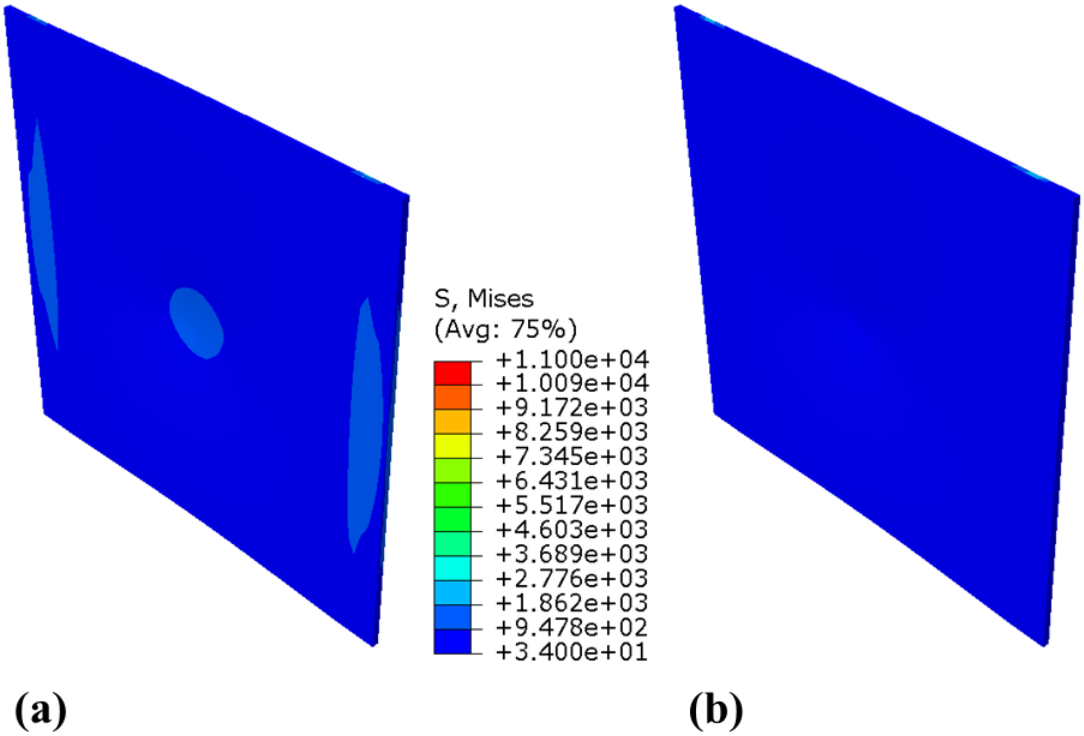

Fig. 7-18. Stresses in the interface-2 with (a) confined state and, (b) unconfined state

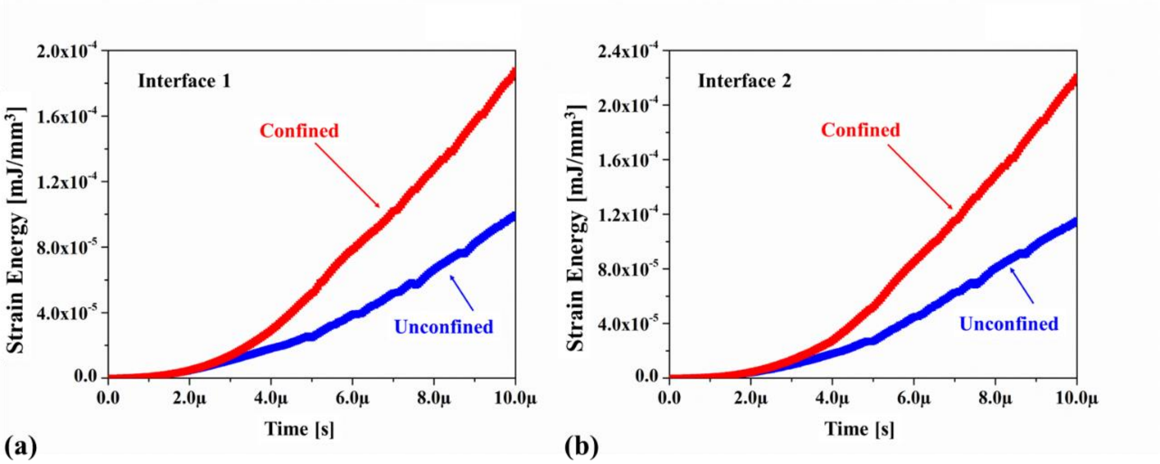

Fig. 7-19. Strain energy in the interface (a) 1 and, (b) 2 in the confined and unconfined state

In summary, the shrimp exoskeleton was modeled with the properties of the system derived from the nanoindentation experiments as well as the interface properties derived from the molecular dynamic simulations on the chitin interfaces. The interface properties were then applied to the model based on the confinement law and the stress distributions were compared. The effect of each layer can be seen in the stress plots of each layer. The top layer where the loading is directly applied takes most of the stresses as shown in Fig. 7-14. As we go down the multilayered system, the middle layers also contribute to the stiffness of the system as shown in Fig. 7-15 and Fig. 7-16. It can be seen from the stress distribution that even when the properties of the each layers are same, the stresses are different in the confined case as compared to the unconfined case because of the presence of the interfaces. It can be further illustrated in the stress plots of the interfaces given in Fig. 7-17and Fig. 7-18. The confined interfaces contribute more in absorbing the stresses as compared to unconfined interfaces. It can be quantified further by comparing the strain energies of these interfaces given in Fig. 7-19. The confined interface absorbs higher energy as compared to unconfined case with the second interface with higher energy because it experiences higher deformations during the loading.

In conclusion, the interface constitutive law gives us a way to quantify the interface contribution in a multilayered materials and provides a way to develop customized multilayered materials based on the applications.

CHAPTER 8. SUMMARY AND CONCLUSIONS

The main goal of the study was to develop a constitutive law describing the behavior of interfaces in multilayered materials along with the consideration of strain rates of deformation and possible other factors affecting the interfaces. The problem was approached by considering an epoxy interface between two glass plates. The behavior of the epoxy interface was analyzed using nanoindentation, nanoscale impact and nanomechanical Raman spectroscopy technique. The nanoindentation was preferred because of its applicability to perform experiments at the length scale of the interfaces in this study since the epoxy interface was 10 micron thick. The nanoscale impact tests were used to perform high strain rate tests to be able to understand the effect of rate of loading. The stress-strains in the epoxy interface and bulk epoxy were compared for higher and lower strain rates and it was concluded that the confinement effect on the interfaces had a considerable effect on the stress-strain response. The confinement effect was then quantified by developing an analytical solution to obtain the multiaxial stresses in the interfaces. The analytical solution was verified using the nanomechanical Raman spectroscopy stress measurements.

Based on the rate dependent stress-strain analyses and the confinement analyses, a new law was developed that couples both the strain rate and confinement effect in interfaces. The new law was fit to the stress-strain data of 10 micron thick interfaces to obtain the material parameters. The effect of thickness of the interface and the size of impactor was also analyzed by impacting the interface by 1, 10 and 100 micron radius indenters. The interface constitutive model was then also implemented in the finite element software to solve the case of multilayered material and to quantify the role of the interface.

In conclusion, the interface behavior was analyzed in the case of epoxy interfaces between glass plates at nanometer to micrometer scales. A new model capturing both strain rate and confinement effects was developed for strain rates up to $10^3 s^{-1}$. An analytical model was developed to measure the lateral stress tensors during indentation experiments. The stress-strain analysis was performed along with the EDX analysis for quasistatic and dynamic experiments. The following points are drawn from the analyses given in earlier sections.

1. The confinement and the strain-rate effect are coupled with each other and to predict the material deformation under indentation loading a new model developed in this paper is more applicable. The new model fits the data from the confined interfaces showing the need to consider the interface as a separate entity in the analyses.
2. The interface has a complex multiaxial stress state during the deformations which needs to be accounted for by developing suitable analytical solutions. These stresses can be used to find the confinement effect of the interfaces as shown in the current study.
3. The development of the interface constitutive law gives a way to quantify the role of interfaces during the deformation of multilayered materials. The stress strain behavior of the interfaces in the case of finite thickness epoxy interfaces shows the dependence on impactor size which can be captured with the model parameters based on the interface thickness.
4. The interface stresses needs to be measured experimentally using advance measurement tools such as nanomechanical Raman spectroscopy experiments. It

provides a non-contact way to measure the residual stresses are present in the interfaces as well.

REFERENCES

1. Verma, D., T. Qu, and V. Tomar, *Scale Dependence of the Mechanical Properties and Microstructure of Crustaceans Thin Films as Biomimetic Materials.* Jom, 2015. **67**(4): p. 858-866.
2. Verma, D. and V. Tomar, *Structural-Nanomechanical Property Correlation of Shallow Water Shrimp (Pandalus platyceros) Exoskeleton at Elevated Temperature.* Journal of Bionic Engineering, 2014. **11**(3): p. 360-370.
3. Verma, D. and V. Tomar, *An investigation into environment dependent nanomechanical properties of shallow water shrimp (Pandalus platyceros) exoskeleton.* Mater Sci Eng C Mater Biol Appl, 2014. **44**(0): p. 371-9.
4. Boßelmann, F., et al., *The composition of the exoskeleton of two crustacea: The American lobster Homarus americanus and the edible crab Cancer pagurus.* Thermochimica Acta, 2007. **463**(1–2): p. 65-68.
5. Raabe, D., et al., *Microstructure and crystallographic texture of the chitin–protein network in the biological composite material of the exoskeleton of the lobster< i> Homarus americanus</i>.* Materials Science and Engineering: A, 2006. **421**(1): p. 143-153.
6. Mayer, G., *New toughening concepts for ceramic composites from rigid natural materials.* Journal of the Mechanical Behavior of Biomedical Materials, 2011. **4**(5): p. 670-681.
7. Chen, P.-Y., et al., *Structure and mechanical properties of crab exoskeletons.* Acta Biomaterialia, 2008. **4**(3): p. 587-596.
8. Flores-Johnson, E., et al., *Numerical investigation of the impact behaviour of bioinspired nacre-like aluminium composite plates.* Composites Science and Technology, 2014. **96**: p. 13-22.
9. Feng, Q.L., et al., *Crystal orientation, toughening mechanisms and a mimic of nacre.* Materials Science and Engineering: C, 2000. **11**(1): p. 19-25.
10. Verma, D. and V. Tomar, *A comparison of nanoindentation creep deformation characteristics of hydrothermal vent shrimp (Rimicaris exoculata) and shallow water shrimp (Pandalus platyceros) exoskeletons.* Journal of Materials Research, 2015. **30**(8): p. 1110-1120.
11. Verma, D. and V. Tomar, *An investigation into mechanical strength of exoskeleton of hydrothermal vent shrimp (Rimicaris exoculata) and shallow water shrimp (Pandalus platyceros) at elevated temperatures.* Mater Sci Eng C Mater Biol Appl, 2015. **49**(0): p. 243-50.
12. Raabe, D., C. Sachs, and P. Romano, *The crustacean exoskeleton as an example of a structurally and mechanically graded biological nanocomposite material.* Acta Materialia, 2005. **53**(15): p. 4281-4292.
13. Bouville, F., et al., *Strong, tough and stiff bioinspired ceramics from brittle constituents.* Nature materials, 2014. **13**(5): p. 508-514.
14. Chen, B., et al., *Laminated microstructure of Bivalva shell and research of biomimetic ceramic/polymer composite.* Ceramics International, 2004. **30**(7): p. 2011-2014.

15. Bechtle, S., S.F. Ang, and G.A. Schneider, *On the mechanical properties of hierarchically structured biological materials.* Biomaterials, 2010. **31**(25): p. 6378-6385.
16. Sorrentino, L., et al., *Mechanical performance optimization through interface strength gradation in PP/glass fibre reinforced composites.* Composites Part B: Engineering, 2015. **76**(0): p. 201-208.
17. Verma, D., et al., *Evaluation of Incoherent Interface Strength of Solid-State-Bonded Ti64/Stainless Steel Under Dynamic Impact Loading.* Jom, 2015. **67**(8): p. 1694-1703.
18. Simeoli, G., et al., *The role of interface strength on the low velocity impact behaviour of PP/glass fibre laminates.* Composites Part B: Engineering, 2014. **62**(0): p. 88-96.
19. Lopez, M.I., P.E. Meza Martinez, and M.A. Meyers, *Organic interlamellar layers, mesolayers and mineral nanobridges: Contribution to strength in abalone (Haliotis rufescence) nacre.* Acta Biomaterialia, 2014. **10**(5): p. 2056-2064.
20. Wang, X., et al., *An investigation of Ti-43Al-9V/Ti-6Al-4V interface by diffusion bonding.* Intermetallics, 2013. **36**: p. 127-132.
21. Savage, A.J., et al., *The Effect of Sliding Knots on the Suture-Tendon Interface Strength A Biomechanical Analysis Comparing Sliding and Static Arthroscopic Knots.* The American journal of sports medicine, 2013. **41**(2): p. 296-301.
22. Roeder, R.K., *Chapter 3 - Mechanical Characterization of Biomaterials*, in *Characterization of Biomaterials*, A. Bandyopadhyay and S. Bose, Editors. 2013, Academic Press: Oxford. p. 49-104.
23. Kundu, S., S. Sam, and S. Chatterjee, *Interfacial reactions and strength properties in dissimilar titanium alloy/Ni alloy/microduplex stainless steel diffusion bonded joints.* Materials Science and Engineering: A, 2013. **560**: p. 288-295.
24. Kundu, S., et al., *Interfacial reactions and strength properties of diffusion bonded joints of Ti64 alloy and 17-4PH stainless steel using nickel alloy interlayer.* Materials & Design, 2013. **51**: p. 714-722.
25. Grandfield, K., A. Palmquist, and H. Engqvist, *Three-dimensional structure of laser-modified Ti6Al4V and bone interface revealed with STEM tomography.* Ultramicroscopy, 2013. **127**: p. 48-52.
26. Damodaram, R., S.G.S. Raman, and K.P. Rao, *Microstructure and mechanical properties of friction welded alloy 718.* Materials Science and Engineering: A, 2013. **560**: p. 781-786.
27. Azouaoui, K., et al. *Impact fatigue damage of glass/epoxy plates predicted from three parameters model*. in *ICF12, Ottawa 2009*. 2013.
28. Azouaoui, K., Z. Azari, and G. Pluvinage, *Evaluation of impact fatigue damage in glass/epoxy composite laminate.* International journal of Fatigue, 2010. **32**(2): p. 443-452.
29. Xu, X., et al., *Multiscale bio-inspired honeycomb structure material with high mechanical strength and low density.* Journal of Materials Chemistry, 2012. **22**(21): p. 10883-10888.
30. Weaver, J.C., et al., *The stomatopod dactyl club: a formidable damage-tolerant biological hammer.* Science, 2012. **336**(6086): p. 1275-1280.

31. Sadighi, M., R.C. Alderliesten, and R. Benedictus, *Impact resistance of fiber-metal laminates: A review.* International Journal of Impact Engineering, 2012. **49**(0): p. 77-90.
32. Sam, S., S. Kundu, and S. Chatterjee, *Diffusion bonding of titanium alloy to micro-duplex stainless steel using a nickel alloy interlayer: Interface microstructure and strength properties.* Materials & Design, 2012. **40**: p. 237-244.
33. Li, P., et al., *Diffusion bonding titanium to stainless steel using Nb/Cu/Ni multi-interlayer.* Materials Characterization, 2012. **68**: p. 82-87.
34. Li, N., M. Nastasi, and A. Misra, *Defect structures and hardening mechanisms in high dose helium ion implanted Cu and Cu/Nb multilayer thin films.* International Journal of Plasticity, 2012. **32–33**(0): p. 1-16.
35. Kundu, S., et al., *Influence of interface microstructure on the mechanical properties of titanium/17-4 PH stainless steel solid state diffusion bonded joints.* Materials & Design, 2012. **37**: p. 560-568.
36. Koyanagi, J., H. Nakatani, and S. Ogihara, *Comparison of glass–epoxy interface strengths examined by cruciform specimen and single-fiber pull-out tests under combined stress state.* Composites Part A: Applied Science and Manufacturing, 2012. **43**(11): p. 1819-1827.
37. Koyanagi, J. and S. Ogihara, *Temperature dependence of glass fiber/epoxy interface normal strength examined by a cruciform specimen method.* Composites Part B: Engineering, 2011. **42**(6): p. 1492-1496.
38. Chen, J., et al., *Integrated honeycomb technology motivated by the structure of beetle forewings.* Materials Science and Engineering: C, 2012. **32**(7): p. 1813-1817.
39. Cerreta, E., et al., *The role of interfaces on dynamic damage in two phase metals.* AIP Conference Proceedings, 2012. **1426**(1): p. 1317-1320.
40. Wu, M.S., *Strategies and challenges for the mechanical modeling of biological and bio-inspired materials.* Materials Science and Engineering: C, 2011. **31**(6): p. 1209-1220.
41. Raman, S. and R. Kumar, *Construction and nanomechanical properties of the exoskeleton of the barnacle,< i> Amphibalanus reticulatus</i>.* Journal of structural biology, 2011. **176**(3): p. 360-369.
42. Mohan, B., G. Freihofer, and S. Raghavan. *Measuring Tensile Stresses in CNF/Polymer composites using Raman Spectroscopy*. in *52nd AIAA/ASME/ASCE/AHS/ASC Structures, Structural Dynamics and Materials Conference 19th AIAA/ASME/AHS Adaptive Structures Conference 13t*. 2011.
43. Menna, C., et al., *Numerical simulation of impact tests on GFRP composite laminates.* International Journal of Impact Engineering, 2011. **38**(8–9): p. 677-685.
44. McNamara, L., *2.210 - Bone as a Material*, in *Comprehensive Biomaterials*, D. Editor-in-Chief: Paul, Editor. 2011, Elsevier: Oxford. p. 169-186.
45. Korhonen, R.K. and S. Saarakkala, *Biomechanics and modeling of skeletal soft tissues.* 2011.

46. Klocke, F., et al., *Adhesive interlayers' effect on the entire structure strength of glass molding tools' Pt–Ir coatings by nano-tests determined.* Surface and Coatings Technology, 2011. **206**(7): p. 1867-1872.
47. Chen, J., et al., *Effects of mechanical properties and layer structure on the cyclic dynamic loading of TiN-based coatings.* Surface and Coatings Technology, 2011. **206**(2): p. 522-529.
48. Castellani, C., et al., *Bone–implant interface strength and osseointegration: Biodegradable magnesium alloy versus standard titanium control.* Acta Biomaterialia, 2011. **7**(1): p. 432-440.
49. Wheeler, J., et al., *Evaluation of micromechanical behaviour of plasma electrolytic oxidation (PEO) coatings on Ti–6Al–4V.* Surface and Coatings Technology, 2010. **204**(21): p. 3399-3409.
50. Nikolov, S., et al., *Revealing the Design Principles of High-Performance Biological Composites Using Ab initio and Multiscale Simulations: The Example of Lobster Cuticle.* Advanced Materials, 2010. **22**(4): p. 519-526.
51. Lau, D. and O. Büyüköztürk, *Fracture characterization of concrete/epoxy interface affected by moisture.* Mechanics of Materials, 2010. **42**(12): p. 1031-1042.
52. Koyanagi, J., et al., *Time and temperature dependence of carbon/epoxy interface strength.* Composites Science and Technology, 2010. **70**(9): p. 1395-1400.
53. Bezares, J., R.J. Asaro, and M. Hawley, *Macromolecular structure of the organic framework of nacre in Haliotis rufescens: Implications for mechanical response.* Journal of Structural Biology, 2010. **170**(3): p. 484-500.
54. Wang, L., et al., *Anisotropic design of a multilayered biological exoskeleton.* Journal of Materials Research, 2009. **24**(12): p. 3477-3494.
55. Luz, G.M. and J.F. Mano, *Biomimetic design of materials and biomaterials inspired by the structure of nacre.* Philosophical Transactions of the Royal Society A: Mathematical, Physical and Engineering Sciences, 2009. **367**(1893): p. 1587-1605.
56. Fox-Rabinovich, G., et al., *Design and performance of AlTiN and TiAlCrN PVD coatings for machining of hard to cut materials.* Surface and Coatings Technology, 2009. **204**(4): p. 489-496.
57. Das, B., et al., *Nano-indentation studies on polymer matrix composites reinforced by few-layer graphene.* Nanotechnology, 2009. **20**(12): p. 125705.
58. Barthelat, F., J.E. Rim, and H.D. Espinosa, *A Review on the Structure and Mechanical Properties of Mollusk Shells–Perspectives on Synthetic Biomimetic Materials*, in *Applied Scanning Probe Methods XIII*. 2009, Springer. p. 17-44.
59. Hernandez, A.I., et al., *Residual interface tensile strength of ceramic bonded to dentin after cyclic loading and aging.* The Journal of prosthetic dentistry, 2008. **99**(3): p. 209-217.
60. Fu, S.-Y., et al., *Effects of particle size, particle/matrix interface adhesion and particle loading on mechanical properties of particulate–polymer composites.* Composites Part B: Engineering, 2008. **39**(6): p. 933-961.
61. Birringer, R. and P. Zimmer, *Novel approach to measuring interface stress of phase boundaries: The case of Ag/Ni.* Scripta Materialia, 2008. **58**(8): p. 639-642.

62. Kang, B.C., et al., *Bilayer thickness effects on nanoindentation behavior of Ag/Ni multilayers.* Scripta Materialia, 2007. **57**(8): p. 703-706.
63. Ray, B., *Temperature effect during humid ageing on interfaces of glass and carbon fibers reinforced epoxy composites.* Journal of Colloid and Interface Science, 2006. **298**(1): p. 111-117.
64. Mayer, G., *New classes of tough composite materials—Lessons from natural rigid biological systems.* Materials Science and Engineering: C, 2006. **26**(8): p. 1261-1268.
65. Sain, M., et al., *Interface modification and mechanical properties of natural fiber-polyolefin composite products.* Journal of Reinforced Plastics and Composites, 2005. **24**(2): p. 121-130.
66. Park, S.H., et al., *Cement–cement interface strength: Influence of time to apposition.* Journal of Biomedical Materials Research, 2001. **58**(6): p. 741-746.
67. Swadener, J., K. Liechti, and A.d. Lozanne, *The intrinsic toughness and adhesion mechanisms of a glass/epoxy interface.* Journal of the Mechanics and Physics of Solids, 1999. **47**(2): p. 223-258.
68. Josell, D., et al., *Measuring the interface stress: Silver/nickel interfaces.* Journal of materials research, 1999. **14**(11): p. 4358-4365.
69. Bonfield, W., M. Wang, and K.E. Tanner, *Interfaces in analogue biomaterials.* Acta Materialia, 1998. **46**(7): p. 2509-2518.
70. Melnick, C.A., Z. Chen, and J.J. Mecholsky, *Hardness and toughness of exoskeleton material in the stone crab, Menippe mercenaria.* Journal of Materials Research, 1996. **11**(11): p. 2903-2907.
71. Berger, S. and F. Spaepen, *The Ag/Cu interface stress.* Nanostructured Materials, 1995. **6**(1–4): p. 201-204.
72. Chateauminois, A., et al., *Study of the interfacial degradation of a glass-epoxy composite during hygrothermal ageing using water diffusion measurements and dynamic mechanical thermal analysis.* Polymer, 1994. **35**(22): p. 4766-4774.
73. Gupta, V. and J. Yuan, *Measurement of interface strength by the modified laser spallation technique. II. Applications to metal/ceramic interfaces.* Journal of applied physics, 1993. **74**(4): p. 2397-2404.
74. Gupta, V., et al., *Measurement of interface strength by a laser spallation technique.* Journal of the Mechanics and Physics of Solids, 1992. **40**(1): p. 141-180.
75. Dubey, D.K. and V. Tomar, *Understanding the influence of structural hierarchy and its coupling with chemical environment on the strength of idealized tropocollagen–hydroxyapatite biomaterials.* Journal of the Mechanics and Physics of Solids, 2009. **57**(10): p. 1702-1717
76. Dubey, D.K. and V. Tomar, *Role of the nanoscale interfacial arrangement in mechanical strength of tropocollagen-hydroxyapatite based hard biomaterials.* Acta Biomaterialia, 2009. **5**(7): p. 2704-2716.
77. Dubey, D.K. and V. Tomar, *The effect of tensile and compressive loading on the hierarchical strength of idealized tropocollagen-hydroxyapatite biomaterials as a function of the chemical environment.* Journal of Physics-Condensed Matter, 2009. **21**(20).

78. Dubey, D.K. and V. Tomar, *Role of hydroxyapatite crystal shape in nanoscale mechanical behavior of model tropocollagen-hydroxyapatite hard biomaterials.* Materials Science & Engineering C-Materials for Biological Applications, 2009. **29**(7): p. 2133-2140.
79. Landis, W.J., et al., *Mineralization of collagen may occur on fibril surfaces: evidence from conventional and high-voltage electron microscopy and three-dimensional imaging.* Journal of Structural Biology, 1996. **117**: p. 24-35.
80. Landis, W.J., et al., *Structural relations between collagen and mineral in bone as determined by high voltage electron microscopic tomography.* Microscopy Research and Technique, 1996. **33**(2): p. 192-202.
81. Fratzl, P., et al., *Nucleation and growth of mineral crystals in bone studied by small-angle X-ray scattering.* Calcified Tissue International, 1991. **48**(6): p. 407-413.
82. Weiner, S., Y. Talmon, and W. Traub, *Electron diffraction of mollusc shell organic matrices and their relationship to the mineral phase.* International Journal of Biological Macromolecules, 1983. **5**(6): p. 325-328.
83. Al-Sawalmih, A., et al., *Microtexture and chitin/calcite orientation relationship in the mineralized exoskeleton of the American lobster.* Advanced functional materials, 2008. **18**(20): p. 3307-3314.
84. Qu, T., et al., *Mechanics of organic-inorganic biointerfaces-Implications for strength and creep properties.* Mrs Bulletin, 2015. **40**(4): p. 349-358.
85. Qu, T., et al., *Influence of interfacial interactions on deformation mechanism and interface viscosity in alpha-chitin-calcite interfaces.* Acta Biomater, 2015. **25**(0): p. 325-38.
86. Qu, T. and V. Tomar, *Nanomechanics based investigation into interface-thermomechanics of collagen and chitin based biomaterials.* 2014.
87. McMurtrey, M.D., et al., *Strain localization at dislocation channel–grain boundary intersections in irradiated stainless steel.* International Journal of Plasticity, 2014. **56**(0): p. 219-231.
88. Gautieri, A., et al., *Viscoelastic properties of model segments of collagen molecules.* Matrix Biology, 2012. **31**(2): p. 141-149.
89. Shi, Y., T. Swait, and C. Soutis, *Modelling damage evolution in composite laminates subjected to low velocity impact.* Composite Structures, 2012. **94**(9): p. 2902-2913.
90. FANG, T., W. CHANG, and J.-C. Yang, *Temperature effect on mechanical properties of graphene sheets under tensile loading.* Digest journal of nanomaterials and biostructures, 2012. **7**(4): p. 1811-1816.
91. Zhang, R., et al., *Dislocation nucleation mechanisms from fcc/bcc incoherent interfaces.* Scripta Materialia, 2011. **65**(11): p. 1022-1025.
92. Wang, J. and A. Misra, *An overview of interface-dominated deformation mechanisms in metallic multilayers.* Current Opinion in Solid State and Materials Science, 2011. **15**(1): p. 20-28.
93. Wang, J., et al., *The influence of interface shear strength on the glide dislocation–interface interactions.* Acta Materialia, 2011. **59**(8): p. 3164-3173.
94. You, M., et al., *3-D Finite Element Analysis of Bonded Joints under Impact Loading.* Advanced Materials Research, 2010. **97**: p. 763-766.

95. Wisnom, M.R., *Modelling discrete failures in composites with interface elements.* Composites Part A: Applied Science and Manufacturing, 2010. **41**(7): p. 795-805.
96. Wang, J., R.G. Hoagland, and A. Misra, *Mechanics of nanoscale metallic multilayers: From atomic-scale to micro-scale.* Scripta Materialia, 2009. **60**(12): p. 1067-1072.
97. Ichikawa, Y., et al., *Molecular dynamics and multiscale homogenization analysis of seepage/diffusion problem in bentonite clay.* International journal for numerical methods in engineering, 2002. **54**(12): p. 1717-1749.
98. Paipetis, A. and C. Galiotis. *Modelling the stress–transfer efficiency of carbon–epoxy interfaces*. in *Proceedings of the Royal Society of London A: Mathematical, Physical and Engineering Sciences*. 2001. The Royal Society.
99. Subero, J., et al., *Effect of interface energy on the impact strength of agglomerates.* Powder Technology, 1999. **105**(1–3): p. 66-73.
100. Gibbs, J.W., *The Collected Works of J. Willard Gibbs, Volume I: Thermodynamics*. 1928: Yale University Press.
101. Shuttleworth, R., *The surface tension of solids.* Proceedings of the Physical Society. Section A, 1950. **63**(5): p. 444.
102. Gurtin, M.E. and A.I. Murdoch, *A continuum theory of elastic material surfaces.* Archive for Rational Mechanics and Analysis, 1975. **57**(4): p. 291-323.
103. Sharma, P. and S. Ganti, *Size-dependent Eshelby's tensor for embedded nano-inclusions incorporating surface/interface energies.* Journal of Applied Mechanics, 2004. **71**(5): p. 663-671.
104. Yang, F., *Size-dependent effective modulus of elastic composite materials: spherical nanocavities at dilute concentrations.* Journal of Applied Physics, 2004. **95**(7): p. 3516-3520.
105. Cammarata, R., *Surface and interface stress effects on interfacial and nanostructured materials.* Materials Science and Engineering: A, 1997. **237**(2): p. 180-184.
106. Dingreville, R., A. Hallil, and S. Berbenni, *From coherent to incoherent mismatched interfaces: A generalized continuum formulation of surface stresses.* Journal of the Mechanics and Physics of Solids, 2014. **72**(0): p. 40-60.
107. Dingreville, R. and J. Qu, *Interfacial excess energy, excess stress and excess strain in elastic solids: Planar interfaces.* Journal of the Mechanics and Physics of Solids, 2008. **56**(5): p. 1944-1954.
108. Dingreville, R., J. Qu, and C. Mohammed, *Surface free energy and its effect on the elastic behavior of nano-sized particles, wires and films.* Journal of the Mechanics and Physics of Solids, 2005. **53**(8): p. 1827-1854.
109. Ustinov, K.B., R.V. Goldstein, and V.A. Gorodtsov, *On the Modeling of Surface and Interface Elastic Effects in Case of Eigenstrains*, in *Surface Effects in Solid Mechanics: Models, Simulations and Applications*, H. Altenbach and F.N. Morozov, Editors. 2013, Springer Berlin Heidelberg: Berlin, Heidelberg. p. 167-180.
110. Zhang, W.X., T.J. Wang, and X. Chen, *Effect of surface/interface stress on the plastic deformation of nanoporous materials and nanocomposites.* International Journal of Plasticity, 2010. **26**(7): p. 957-975.

111. Dingreville, R. and J. Qu, *A semi-analytical method to estimate interface elastic properties.* Computational Materials Science, 2009. **46**(1): p. 83-91.
112. Duan, H.L., et al., *Size-dependent effective elastic constants of solids containing nano-inhomogeneities with interface stress.* Journal of the Mechanics and Physics of Solids, 2005. **53**(7): p. 1574-1596.
113. Nix, W.D. and H. Gao, *An atomistic interpretation of interface stress.* Scripta Materialia, 1998. **39**(12): p. 1653-1661.
114. Cahn, J., J. Pan, and R. Balluffi, *Diffusion induced grain boundary migration.* Scripta Metallurgica, 1979. **13**(6): p. 503-509.
115. Herring, C. *The use of classical macroscopic concepts in surface energy problems*. in *Structure and properties of solid surfaces*. 1953.
116. Qiao, P., M. Yang, and F. Bobaru, *Impact mechanics and high-energy absorbing materials: review.* Journal of Aerospace Engineering, 2008. **21**(4): p. 235-248.
117. Marsh, J., et al., *Nanomechanical Characterization of Temperature-Dependent Mechanical Properties of Ion-Irradiated Zirconium with Consideration of Microstructure and Surface Damage.* Jom, 2015. **67**(12): p. 2945-2958.
118. Beake, B.D., et al., *Nanoscale repetitive impact testing of polymer films.* Journal of materials research, 2004. **19**(01): p. 237-247.
119. Steinberg, D., S. Cochran, and M. Guinan, *A constitutive model for metals applicable at high‐strain rate.* Journal of Applied Physics, 1980. **51**(3): p. 1498-1504.
120. Johnson, G.R. and W.H. Cook. *A constitutive model and data for metals subjected to large strains, high strain rates and high temperatures*. in *Proceedings of the 7th International Symposium on Ballistics*. 1983. The Netherlands.
121. Zerilli, F.J. and R.W. Armstrong, *Dislocation‐mechanics‐based constitutive relations for material dynamics calculations.* Journal of Applied Physics, 1987. **61**(5): p. 1816-1825.
122. Steinberg, D. and C. Lund, *A constitutive model for strain rates from 10− 4 to 106 s− 1.* Journal of Applied Physics, 1989. **65**(4): p. 1528-1533.
123. Lee, W.-S. and C.-F. Lin, *Plastic deformation and fracture behaviour of Ti–6Al–4V alloy loaded with high strain rate under various temperatures.* Materials Science and Engineering: A, 1998. **241**(1): p. 48-59.
124. Constantinides, G., et al., *Quantitative Impact Testing of Energy Dissipation at Surfaces.* Experimental Mechanics, 2009. **49**(4): p. 511-522.
125. Follansbee, P. and U. Kocks, *A constitutive description of the deformation of copper based on the use of the mechanical threshold stress as an internal state variable.* Acta Metallurgica, 1988. **36**(1): p. 81-93.
126. Vanhellemont, J., et al., *On the assessment of local stress distributions in integrated circuits.* Applied Surface Science, 1993. **63**: p. 119-125.
127. De Wolf, I., *Micro-Raman spectroscopy to study local mechanical stress in silicon integrated circuits.* Semiconductor Science and Technology, 1996. **11**(2): p. 139.
128. Anastassakis, E., et al., *Effect of static uniaxial stress on the raman spectrum of silicon.* Solid State Communications, 1970. **8**: p. 133-138.

129. Gan, M. and V. Tomar, *An in situ platform for the investigation of Raman shift in micro-scale silicon structures as a function of mechanical stress and temperature increase.* Review of Scientific Instruments, 2014. **85**(1): p. 013902.
130. Colomban, P., et al., *Raman stress measurement in opaque industrial Cf/epoxy composites submitted to tensile strain.* Composites Part A: Applied Science and Manufacturing, 2006. **37**(4): p. 646-651.
131. Oliver, W.C. and G.M. Pharr, *Improved technique for determining hardness and elastic modulus using load and displacement sensing indentation experiments.* Journal of Materials Research, 1992. **7**(6): p. 1564-1583.
132. Pharr, G., *Measurement of mechanical properties by ultra-low load indentation.* Materials Science and Engineering: A, 1998. **253**(1): p. 151-159.
133. Kalidindi, S.R. and S. Pathak, *Determination of the effective zero-point and the extraction of spherical nanoindentation stress–strain curves.* Acta Materialia, 2008. **56**(14): p. 3523-3532.
134. Johnson, K.L. and K.L. Johnson, *Contact mechanics*. 1987: Cambridge university press.
135. Somekawa, H. and C.A. Schuh, *High-strain-rate nanoindentation behavior of fine-grained magnesium alloys.* Journal of Materials Research, 2012. **27**(09): p. 1295-1302.
136. Moffat, R.J., *Describing the uncertainties in experimental results.* Experimental Thermal and Fluid Science, 1988. **1**(1): p. 3-17.
137. Al Baida, H., et al., *Identifying the stress–strain curve of materials by microimpact testing. Application on pure copper, pure iron, and aluminum alloy 6061-T651.* Journal of Materials Research, 2015. **30**(14): p. 2222-2230.
138. Mok, C.-H. and J. Duffy, *The dynamic stress-strain relation of metals as determined from impact tests with a hard ball.* International Journal of Mechanical Sciences, 1965. **7**(5): p. 355-371.
139. Xu, B. and X. Chen, *Determining engineering stress–strain curve directly from the load–depth curve of spherical indentation test.* Journal of Materials Research, 2010. **25**(12): p. 2297-2307.
140. He, L.H. and M.V. Swain, *Nanoindentation derived stress–strain properties of dental materials.* Dental materials, 2007. **23**(7): p. 814-821.
141. Gray, G.T., *High-Strain-Rate Deformation: Mechanical Behavior and Deformation Substructures Induced.* Annual Review of Materials Research, 2012. **42**(1): p. 285-303.
142. Taylor, L.M., E.-P. Chen, and J.S. Kuszmaul, *Microcrack-induced damage accumulation in brittle rock under dynamic loading.* Computer methods in applied mechanics and engineering, 1986. **55**(3): p. 301-320.
143. Kontou, E. and A. Kallimanis, *Formulation of the viscoplastic behavior of epoxy-glass fiber composites.* Journal of Composite materials, 2005. **39**(8): p. 711-721.
144. Bing, Q. and C. Sun, *Modeling and testing strain rate-dependent compressive strength of carbon/epoxy composites.* Composites science and technology, 2005. **65**(15): p. 2481-2491.
145. Mulliken, A. and M. Boyce, *Mechanics of the rate-dependent elastic–plastic deformation of glassy polymers from low to high strain rates.* International journal of solids and structures, 2006. **43**(5): p. 1331-1356.

146. Yonezu, A., et al., *Characterization of the compressive deformation behavior with strain rate effect of low-density polymeric foams.* Polymer Testing, 2016. **50**: p. 1-8.
147. Dou, R., et al., *Simulation of compression behavior and strain-rate effect for aluminum foam sandwich panels.* Computational Materials Science, 2016. **112**: p. 205-209.
148. Tsai, J. and C. Sun, *Constitutive model for high strain rate response of polymeric composites.* Composites Science and Technology, 2002. **62**(10): p. 1289-1297.
149. Richart, F.E., A. Brandtzaeg, and R.L. Brown, *A study of the failure of concrete under combined compressive stresses.* University of Illinois Bulletin; v. 26, no. 12, 1928.
150. Saatcioglu, M. and S.R. Razvi, *Strength and Ductility of Confined Concrete.* Journal of Structural Engineering-Asce, 1992. **118**(6): p. 1590-1607.
151. Mc Creath, D., J. Newman, and K. Newman, *The influence of aggregate particles on the local strain distribution and fracture mechanism of cement paste during drying shrinkage and loading to failure.* Matériaux et Construction, 1969. **2**(1): p. 73-85.
152. Hoppel, C.P., T.A. Bogetti, and J.W. Gillespie, *Design and analysis of composite wraps for concrete columns.* Journal of reinforced plastics and composites, 1997. **16**(7): p. 588-602.
153. Sun, Y., et al. *Confinement effects of transverse hoops in high strength concrete*. in *CD ROM Proceedings of the 11th World conference on Earthquake Engineering, Acapulco*. 1996.
154. Sun, Y., *PROPOSAL AND APPLICATION OF STRESS-STRAIN MODEL FOR CONCRETE CONFINED BY STEEL TUBES.*
155. Yazici, V. and M.N. Hadi, *Normalized confinement stiffness approach for modeling FRP-confined concrete.* Journal of Composites for Construction, 2012. **16**(5): p. 520-528.
156. Perea, T. and R. Leon, *Behavior of composite CFT beam-columns based on nonlinear fiber element analysis.* ASCE. doi: 10.1061/41142 (396), 2011. **20**.
157. Tung, N.D. and N.V. Tue, *A fracture mechanics-based approach to modeling the confinement effect in reinforced concrete columns.* Construction and Building Materials, 2016. **102**: p. 893-903.
158. Turgay, T., et al. *Stress–strain model for compressive fracture of RC columns confined with CFRP jackets*. in *International association of fracture mechanics for concrete and concrete structures, FraMCoS-6, sixth international conference on fracture mechanics of concrete and concrete structures. Catania, Italy: Taylor and Francis*. 2007.
159. Subhash, G., et al., *Recent advances in dynamic indentation fracture, impact damage and fragmentation of ceramics.* Journal of the American Ceramic Society, 2008. **91**(9): p. 2777-2791.
160. Forquin, P., G. Gary, and F. Gatuingt, *A testing technique for concrete under confinement at high rates of strain.* International Journal of Impact Engineering, 2008. **35**(6): p. 425-446.

161. Bardella, L. and A. Belleri, *Two features of the uniaxial compression of a glassy epoxy resin: the yield stress rate-dependence and the volumetric instability.* Mechanics of Time-Dependent Materials, 2011. **15**(3): p. 255-275.
162. Ustinov, K.B., R.V. Goldstein, and V.A. Gorodtsov, *On the Modeling of Surface and Interface Elastic Effects in Case of Eigenstrains*, in *Surface Effects in Solid Mechanics*. 2013, Springer Berlin Heidelberg. p. 167-180.
163. Makkonen, L., *Misinterpretation of the Shuttleworth equation.* Scripta Materialia, 2012. **66**(9): p. 627-629.
164. Johnson, K.L., *Contact Mechanics*. 1985, Cambridge: Cambridge University Press.
165. Timoschenko, S.P. and J.N. Goodier, *Theory of Elasticity*. 1970, Stanford: McGraw-Hill, Inc.
166. Ling, F.F., W.M. Lai, and D.A. Lucca, *Fundamentals of Surface Mechanics* - *with Applications*. 2002, Austin: Springer-Verlag.
167. Hertz, *Ueber die Beruehrung fester elastischer Koerper*, in *Journal fuer die reine und angewandte Mathematik 92*. 1881. p. 156-171.
168. Flinn, P.A. and G.A. Waychunas, *A new x-ray diffractometer design for thin-film texture, strain, and phase characterization.* Journal of Vacuum Science & Technology B, 1988. **6**(6): p. 1749-1755.
169. Amadio, C. and C. Bedon, *Blast analysis of laminated glass curtain walls equipped by viscoelastic dissipative devices.* Buildings, 2012. **2**(3): p. 359-383.

VITA

Devendra Verma

Devendra Verma hails from Alwar, Rajasthan, India. He finished his high school in Alwar and then moved to Kanpur to complete his bachelors from Indian Institute of Technology Kanpur. He visited Texas A&M University as an undergraduate researcher in summer of 2010 which inspired him to pursue a higher degree. In the following year in Aug 2011, he joined Purdue University as a master's student where he continued on for his PhD from Jan 2013. His major research work is focused on understand the interfaces in different material systems. He has developed a constitutive law to be able to study these interfaces.

During his stay at Purdue, he has been fortunate enough to work on a variety of problems from biomaterials to super alloys, from high temperature material properties to soft materials characterization. His work has resulted in the publication of 12 journal papers, 4 conference papers, a book, around 20 conference presentation with several other papers in submission. He has received several awards from various conferences such as Society of Engineering Science travel award, United States Association for Computational Mechanics travel award, NSF Fellowship, Haythornthwaite Foundation Student travel award from the American Society of Mechanical Engineers, Erasmus Mundus (Europe) Exchange Program Scholarship. In addition, he has received various awards from Purdue including Graduate Student Excellence award and Outstanding Service Scholarship.

PUBLICATIONS

Book

1. V. Tomar, T. Qu, D. K. Dubey, D. Verma, Y. Zhang, “Multiscale Characterization of Biological Systems: Spectroscopy and Modeling”, Springer-Verlag New York, 2015, ISBN 978-1-4939-3451-5

Refereed Journal Publications

1. D. Verma, S. Biswas, C. Prakash and V. Tomar: “Relating Interface Evolution To Interface Mechanics Based On Interface Properties”. (JOMJ-D)
2. D. Verma, M. Exner and V. Tomar: “An Investigation into Strain Rate Dependent Constitutive Properties of a Sandwiched Epoxy Interface”, JMAD, 2016 (Accepted - Journal of Materials and Design)
3. J. Marsh, Y. Zhang, D. Verma, and V. Tomar: “Nanomechanical Characterization of Temperature Dependent Mechanical Properties of Ion Irradiated Zirconium with Consideration of Microstructure and Surface Damage” *JOM, 67(12), 2945* (2015).
4. J. Marsh, Y.s. Han, D. Verma and V. Tomar: “An Investigation into Plastic Deformation of Irradiated Tungsten Microstructure at Elevated Temperatures using the Anand’s Viscoplastic Model” *International Journal of Plasticity, 74, 127* (2015).
5. T. Qu, D. Verma, M. Alucozai and V. Tomar: “Influence of Interfacial Interactions on Deformation Mechanism and Interface Viscosity in α-Chitin–Calcite Interfaces” *Acta Biomaterialia, 25, 325* (2015).
6. D. Verma, J. Singh, A.H. Varma and V. Tomar: “Evaluation of Incoherent Interface Strength of Solid-State-Bonded Ti64/Stainless Steel Under Dynamic Impact Loading” *JOM,* 67(8), 1694 (2015).
7. D. Verma and V. Tomar: “A Comparison of Nanoindentation Creep Deformation Characteristics of Hydrothermal Vent Shrimp (*Rimicaris exoculata*) and Shallow Water Shrimp (*Pandalus platyceros*) Exoskeletons” *Journal of Materials Research*, 30(8), 1110 (2015).
8. D. Verma and V. Tomar: “An Investigation into Mechanical Strength of Exoskeleton of Hydrothermal Vent Shrimp (*Rimicaris exoculata*) and Shallow Water Shrimp (*Pandalus platyceros*) at Elevated Temperatures” *Materials Science and Engineering: C,* 49, 243 (2015).
9. [Featured on Cover Page] D. Verma, T. Qu and V. Tomar: “Scale Dependence of the Mechanical Properties and Microstructure of Crustaceans Thin Films as Biomimetic Materials” *JOM,* 67(4), 858 (2015).
10. T. Qu, D. Verma, M. Shahidi, B. Pichler, C. Hellmich and V. Tomar: “Mechanics of Organic-Inorganic Biointerfaces—Implications for Strength and Creep Properties” *MRS Bulletin*, 40(4), 349 (2015).
11. D. Verma and V. Tomar: “An Investigation into Environment Dependent Nanomechanical Properties of Shallow Water Shrimp (*Pandalus platyceros*) Exoskeleton” *Materials Science and Engineering: C,* 44, 371 (2014).
12. D. Verma and V. Tomar: “Structural-Nanomechanical Property Correlation of Shallow Water Shrimp (*Pandalus platyceros*) Exoskeleton at Elevated Temperature” *Journal of Bionic Engineering*, 11(3), 360 (2014).

Peer Reviewed Publications in Conference Proceedings

1. D. Verma, T. Qu and V. Tomar: Scale Dependence of the Mechanical Properties of Interfaces in Crustaceans Thin Films, in Mechanics of Biological Systems and Materials, Volume 6: Proceedings of the 2016 Annual Conference on Experimental and Applied Mechanics, (Springer International Publishing, City, 2017), pp. 17.
2. C. Prakash, D. Verma, M. Exner, E. Gunduz and V. Tomar: Strain Rate Dependent Failure of Interfaces Examined via Nanoimpact Experiments, in Challenges in Mechanics of Time Dependent Materials, Volume 2: Proceedings of the 2016 Annual Conference on Experimental and Applied Mechanics (Springer International Publishing, City, 2017), pp. 93.
3. T. Qu, D. Verma and V. Tomar: A Nanomechanics Based Investigation into Interface Thermomechanics of Collagen and Chitin Based Biomaterials, in Mechanics of Biological Systems and Materials, Volume 6: Proceedings of the 2015 Annual Conference on Experimental and Applied Mechanics, (Springer International Publishing, City, 2016), pp. 119.
4. D. Verma, C. Prakash, and V. Tomar., 2015, "Interface Impact Experiments and Derivation of Rate Dependent Cohesive Separation Laws" in Proceedings of ICCM20, July 19-24, Copenhagen, Denmark, Paper No. 150701-2814 (5 pages).

Conference Presentations (no proceeding paper)

1. T. N. Nguyen, J. Pribe, T. Siegmund, D. Verma, V. Tomar, and J. Kruzic, "Rate- and Size-Dependent Plasticity of a Nickel-base Superalloy in Instrumented Nanoindentation Processes" SEM 2017, Indianapolis, IN, USA Jun 12 - 15, 2017
2. D. Verma and V. Tomar, "Interface Mechanical Strength and Elastic Constants Calculations via Nano-impact and Nanomechanical Raman Spectroscopy" SEM 2017, Indianapolis, IN, USA Jun 12 - 15, 2017
3. D. Verma and V. Tomar, "Interface Mechanical Strength and Interface Elastic Constants Calculations in Thin Films of Polymer Composites, and Natural Materials" TMS 2017, San Diego, CA, USA Feb. 26 - Mar 2, 2017
4. D. Verma and V. Tomar, "Strain Rate Dependent Failure of Interfaces in Glass/Epoxy and Energetic Materials at Nano-microscale" ASME IMECE 2016, Phoenix, AZ, USA Nov. 11-17, 2016
5. D. Verma and V. Tomar, "Interface Mechanical Strength and Interface Elastic Constants Calculations in Polymer Composites, and Natural Materials" SES 2016, College Park, MD, USA Oct. 2-5, 2016
6. D. Verma, C. Prakash, and V. Tomar, 2015, "Strain Rate Dependent Failure of Ammonium Perchlorate-HTPB Interfaces at Nano to Microscale Examined via Nanoimpact Experiments" in Proceedings of SEM 2016, June 6-9, 2016, Orlando, FL
7. D. Verma, and V. Tomar, 2015, "Strain Rate Dependent Failure of Epoxy Interfaces between Glass Plates" THERMEC 2016, May 29 - June 3, 2016,Graz, Austria
8. D. Verma and V. Tomar, "Strain-rate Dependent Deformation Characteristic Mechanisms of Confined Epoxy Interfaces" EMIPMC2016**,** Nashville, TN, May 22-25, 2015
9. D. Verma and V. Tomar, "Strain-rate Dependent Failure of Glass/Epoxy Interfaces" TMS 2016, Nashville, TN, USA Feb. 14-18, 2016

10. D. Verma and V. Tomar, “Strass-strain Analysis of Glass/Epoxy Interfaces via Quasistatic and Dynamic Indentation” IMECE2015, Houston, TX, Nov. 13-19, 2015
11. D. Verma and V. Tomar, “An Analysis and Characterization of Interface Thickness Dependent Deformation Mechanisms via Dynamic Indentation” SES 2015, College Station, TX, USA Oct. 26-28, 2015
12. D. Verma and V. Tomar, “Strain Rate Dependent Failure of Metallic Interfa ces at Nano-micro Scale via Nano-Impact Experiments” ICCM20, Copenhagen, Denmark July 19-24, 2015
13. [Keynote] D. Verma and V. Tomar, “An Investigation into Strain-rate Dependent Failure of Metallic Material Interfaces” McMat2015, Seattle, WA, USA June 29-July 1, 2015
14. D. Verma and V. Tomar, “A Nanomechanics Based Investigation into Interface Thermomechanics of Collagen and Chitin Based Biomaterials” SEM2015, Costa Mesa, CA, Jun 8-11, 2015
15. D. Verma and V. Tomar, “An Investigation into Strain-rate Dependent Failure of Material Interfaces” MACH Conference, Annapolis, MD, USA April 8-10, 2015
16. [Invited] D. Verma and V. Tomar, “An Investigation into Environment and Temperature Dependent Nanomechanical Properties of the Shallow Water Shrimp (Pandalus Platyceros) and Deep Sear Shrimp (Rimicaris Exoculata) Exoskeleton” TMS 2015, Orlando, FL, USA Mar. 15- 19, 2015
17. D. Verma and V. Tomar, “An Investigation into Environment and Temperature Dependent Nanomechanical Properties of Crustacean Exoskeleton of Shallow Water and Deep Sea Shrimps” SES 2014, West Lafayette, IN, USA Oct. 1- 3, 2014
18. D. Verma and V. Tomar, “An Investigation into Temperature Dependent Nanomechanical Properties of Crustacean Exoskeleton of Shallow Water Shrimps” EMI 2014, Hamilton Ontario, Canada Aug. 5-8, 2014
19. J. Pavón, D. Verma, M. Alucozai, R. Kempahia, J. P. Allain, V. Tomar, “Nanomechanical Behavior of Bacterial Nano-Cellulose (BNC) for Regenerative Vascular Treatments” EUROMAT, Sevilla, Spain Sep. 8-13, 2013